

PSU-IRL-SCI-395

Classification Numbers 3.3 and 3.4



THE PENNSYLVANIA  
STATE UNIVERSITY

# IONOSPHERIC RESEARCH

Scientific Report 395

## HIGH ENTHALPY HYPERSONIC BOUNDARY LAYER FLOW

N73-32187  
G3/12 17322  
Unclass  
HIGH ENTHALPY HYPERSONIC  
BOUNDARY LAYER FLOW (Pennsylvania State  
Univ.) 462-p HC \$10.25  
CSCL 20D  
163

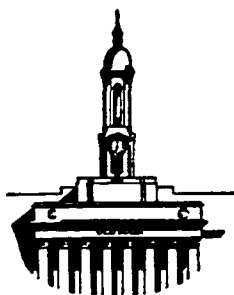
by

Gilbert Yanow

November 6, 1972

*This work was supported by the National Aeronautics and Space Administration under Grant NGR 39-009-129.*

IONOSPHERE RESEARCH LABORATORY



University Park, Pennsylvania

PSU-IRL-SCI-395  
Classification Numbers 3.3 and 3.4

Scientific Report 395

"High Enthalpy Hypersonic Boundary Layer Flow"

by

Gilbert Yanow

November 6, 1972

This work was supported by the National Aeronautics and Space Administration under Grant NGR 39-009-129.

Submitted by:

Bruce R Kendall  
Professor of Physics  
Contract Supervisor

Approved by:

John S. Nisbet  
John S. Nisbet, Director  
Ionosphere Research Laboratory

Ionosphere Research Laboratory

The Pennsylvania State University

University Park, Pennsylvania 16802

## ABSTRACT

This three-part paper describes a theoretical and experimental study of an ionizing laminar boundary layer formed by a very high enthalpy flow (in excess of 12 eV per atom or 7000 cal/gm) with allowance for the presence of Helium driver gas. The theoretical investigation has shown that the use of variable transport properties and their respective derivatives is very important in the solution of equilibrium boundary layer equations of high enthalpy flow. The effect of low level Helium contamination on the surface heat transfer rate is minimal. The variation of ionization is much smaller in a chemically frozen boundary layer solution than in an equilibrium boundary layer calculation and consequently, the variation of the transport properties in the case of the former was not essential in the integration. The experiments have been conducted in a Free Piston Shock Tunnel, and a detailed study of its nozzle operation, including the effects of low levels of Helium driver gas contamination has been made. Neither the extreme solutions of an equilibrium nor of a frozen boundary layer will adequately predict surface heat transfer rate in very high enthalpy flows. This has been attributed to non-equilibrium gas relaxation processes in the boundary layer. A satisfactory approximation can be obtained with what has been called a composite boundary layer calculation. A level in the boundary layer is defined where the gas is assumed to change from primarily chemically frozen in nature to primarily equilibrium in nature. The position of this changeover is determined by a simple criterion based on the recombination rate in the gas stream tubes that are taken to form the boundary layer. The solution are joined by matching the velocities and shear stresses.

## TABLE OF CONTENTS

	Page
Abstract . . . . .	i
List of Figures . . . . .	v
I. Part 1 Introduction and Boundary Layer Calculations. . . . .	1
1. Introduction . . . . .	2
2. Boundary Layers. . . . .	10
Equilibrium Boundary Layer Equations. . . . .	12
Frozen Boundary Layer Equations . . . . .	13
Boundary Layer Equations with Variable Transport Parameters . . . . .	14
Integration of the Boundary Layer Equations . . . . .	16
Displacement Thickness. . . . .	19
Heat Transfer. . . . .	19
Transport Properties. . . . .	20
Free Stream Conditions . . . . .	21
Equilibrium Boundary Layer Calculations . . . . .	23
Frozen Boundary Layer Calculations . . . . .	41
3. Conclusions. . . . .	51
II. Part 2 Free Stream Conditions and Effects of Helium Contamination . . . . .	52
1. Introduction . . . . .	53
2. Pure Argon . . . . .	53
Development of the Reflected Shock Region. . . . .	53
Nozzle Conditions . . . . .	58
Results and Discussion for Pure Argon . . . . .	60
Enthalpy Loss in the Reflected Shock Heated Gas . . . . .	60

	Page
Exit Condition. . . . .	60
Mach No. . . . .	60
Pitot Pressure. . . . .	64
3. Argon--Helium Mixtures. . . . .	64
Theory . . . . .	64
Argon--Helium Mixtures Calculations. . . . .	70
Reflected Shock Region . . . . .	70
Nozzle Flow . . . . .	74
Temperature . . . . .	74
Velocity, Density, Pitot Pressure, and Static Pressure . . . . .	76
Reynold's Number . . . . .	76
4. Test Section Conditions . . . . .	78
Nozzle Exit Values . . . . .	78
Flow Divergence . . . . .	78
Conditions Across the Oblique Shock Front . . . . .	81
5. Contamination Effects on Boundary Layer Calculations . .	85
Nozzle Calculations. . . . .	85
Flat Plate Calculations . . . . .	86
Equilibrium Boundary Layer. . . . .	86
Frozen Boundary Layer . . . . .	95
6. Summary of Part 2. . . . .	102
III. Part 3 Experiments and Data Correlation With Theory. . .	105
1. Introduction . . . . .	106
2. Properties of the Test Section Flow . . . . .	106
Calculated Conditions . . . . .	106
Pitot Pressure Measurements. . . . .	106

	Page
3. Boundary Layers . . . . .	116
Leading Edge Effects . . . . .	116
Heat Transfer . . . . .	119
Composite Boundary Layer Calculations . . . . .	125
4. Summary of Part 3 . . . . .	142
5. References . . . . .	143
6. Symbols and Nomenclature . . . . .	146
7. Acknowledgements . . . . .	152

## LIST OF FIGURES

Figure	Page	
1.1	Schematic drawing of Free Piston Shock Tunnel, "T2," of the A. N. U. Aerophysics Laboratory . . . . .	7
1.2	Velocity profiles for various values of the Profile constant, equilibrium boundary layer . .	25
1.3	Velocity profiles for constant and variable transport parameters. Arrows are $K_1$ at different levels. . . . .	26
1.4	Density profiles for constant and variable transport parameter calculations, equilibrium boundary layer. . . . .	27
1.5	Temperature profile for constant and variable transport parameter calculations, equilibrium boundary layer. . . . .	29
1.6	Ionization profile for constant and variable transport parameter calculations, equilibrium boundary layer. . . . .	30
1.7	Shear stress for constant and variable transport parameter calculations, equilibrium boundary layer. . . . .	31
1.8	Stagnation enthalpy-velocity relationship for constant and variable transport parameters, equilibrium boundary layer, large exit, $x_p = 1$ cm . . . . .	32
1.9	Equilibrium flat plate velocity profiles. Dotted lines are small exit nozzle, $9.5^\circ$ plate inclination. Solid lines are large exit nozzle, $19.5^\circ$ plate inclination, $x_p = 1$ cm . .	34
1.10	Temperature profile for variable transport parameter calculations, large exit nozzle, equilibrium boundary layer. . . . .	35
1.11	Ionization profile for variable transport parameter calculations, large exit nozzle, equilibrium boundary layer. . . . .	36
1.12	Density profile for variable transport parameter calculation, large exit nozzle, equilibrium boundary layer. . . . .	37

Figure	Page
1.13 Conversion from $\eta$ to y-axis for variable transport parameter calculations, large exit, equilibrium boundary layer . . . . .	38
1.14 Thermal conductivity and viscosity for variable transport parameter calculation, large exit nozzle, equilibrium boundary layer . . . . .	39
1.15 Prandtl number and $C_1$ for variable transport parameter calculation, large exit nozzle, equilibrium boundary layer . . . . .	40
1.16 Heat transfer rates. Dotted lines ( $\diamond$ data) are small exit nozzle, $9.5^\circ$ plate inclination. Solid lines ( $\circ$ data) are large exit nozzle, $19.5^\circ$ plate inclination . . . . .	42
1.17 Velocity profile for frozen boundary layer. Transport properties set constant at free stream values. Solid line 100% catalytic surface; dotted line 100% non-catalytic surface . . . . .	44
1.18 Temperature profile for frozen boundary layer. Transport properties set constant at free stream values. Solid line 100% catalytic surface; dotted line 100% non-catalytic surface . . . . .	46
1.19 Density profile for frozen boundary layer. Transport properties set constant at free stream values. Solid line 100% catalytic surface; dotted 100% non-catalytic surface . . . . .	47
1.20 Ionization profile for frozen boundary layer. Transport properties set constant at free stream values. Solid line 100% non-catalytic surface; dotted line 100% catalytic surface . . . . .	48
1.21 Conversion from $\eta$ to y-axis for frozen boundary layer. Transport properties set constant at free stream values. Solid line 100% catalytic surface; dotted line 100% non-catalytic surface . . . . .	49
1.22 Surface heat transfer rate for frozen boundary layer. Transport properties set constant at free stream values. Solid line 100% catalytic surface; dotted line 100% non-catalytic surface. . . . .	50

Figure	Page
2.1 Nozzle area ratio as a function of on axis distance from throat . . . . .	61
2.2 Reflected shock gas changes due to enthalpy loss. . . . .	62
2.3 Exit Mach No. as function of stagnation enthalpy . . . . .	63
2.4 Exit Pitot pressure as function of stagnation enthalpy . . . . .	65
2.5 Gas temperature down small exit nozzle as function of Helium contamination . . . . .	75
2.6 Reynold's number down small exit nozzle as function of Helium Contamination . . . . .	77
2.7 Two dimensional diverging flow over sharp leading edge inclined flat plate (after wedge problem of Hall (1963)) . . . . .	79
2.8 Temperature profile for variable transport parameter calculation, small exit nozzle with contamination at $x_p = 2.0$ cm . . . . .	87
2.9 Ionization profile for variable transport parameter calculation, small exit nozzle with contamination at $x_p = 2.0$ cm . . . . .	88
2.10 Density profile for variable transport parameter calculation, small exit nozzle with contamination at $x_p = 2.0$ cm . . . . .	89
2.11 Conversion from $\eta$ axis to $y$ -axis for variable transport parameter calculation, small exit nozzle with contamination at $x_p = 2.0$ cm . . . . .	90
2.12 Thermal conductivity for variable transport parameter calculation with contamination at $x_p = 2.0$ cm., equilibrium boundary layer . . . . .	92
2.13 Viscosity for variable transport parameter calculation with contamination at $x_p = 2.0$ cm., equilibrium boundary layer . . . . .	93
2.14 Transport parameters for variable transport parameter calculation with contamination at $x_p = 2.0$ cm., equilibrium boundary layer . . . . .	94

Figure	Page
2.15	Calculated surface heat transfer rates for small exit nozzle with contamination, equilibrium boundary layer. . . . . 96
2.16	Frozen boundary layer velocity profile for small exit nozzle, $9.5^\circ$ plate inclination, $x_p$ = cm., 100% catalytic surface, with Helium contamination. 97
2.17	Frozen boundary layer temperature profile for small exit nozzle, $9.5^\circ$ plate inclination, $x_p$ = 2 cm., 100% catalytic surface, with Helium contamination. 98
2.18	Frozen boundary layer density profile for small exit nozzle, $9.5^\circ$ plate inclination, 100% catalytic surface, $x_p$ = 2.0 cm., with Helium contamination. 99
2.19	Frozen boundary layer ionization profile for small exit nozzle, $9.5^\circ$ plate inclination, 100% catalytic surface, $x_p$ = 2.0 cm., with Helium contamination. Solid line 100% non-catalytic surface; dotted line 100% catalytic surface. . . . . 100
2.20	Conversion from $\eta$ axis to the y-axis for the frozen boundary layer, small exit, $9.5^\circ$ plate inclination, $x_p$ = 2.0 cm., 100% catalytic surface . . . . . 103

Figure	Page
3.1a Typical pitot pressure oscillogram for small exit nozzle with 50 micro-seconds/division time base . . . . .	109
3.1b Typical pitot pressure oscillogram for small exit nozzle with 20 micro-seconds/division time base . . . . .	110
3.1c Typical pitot pressure oscillogram for large exit nozzle with 20 micro-seconds/division time base . . . . .	111
3.2 Bifurcated Shock . . . . .	113
3.3 Change of effective nozzle ratio by Helium feeding into Argon flow . . . . .	115
3.4a Drawing of typical surface temperature history in Argon flow. Time base is 20 micro-seconds/division . . . . .	120
3.4b Drawing of typical surface temperature history in Helium flow. Time base is 20 micro-seconds division . . . . .	121
3.5 Helium heat transfer rate at approximately 85 micro-seconds after shock reflection, large exit nozzle, and 9.5° plate inclination. Constant transport parameters were assumed . . . . .	124
3.6 Recombination rate coefficient for Argon . . . . .	129
3.7 Matching criterion for composite boundary layer calculation. Small and large exit nozzles . . . . .	131
3.8 Heat flux for small exit nozzle, plate inclination of 9.5°, $x_p = 2.0$ cm . . . . .	133
3.9 Shear stress for small exit nozzle, 9.5° plate inclination, $x_p = 2.0$ cm . . . . .	136
3.10 Composite boundary layer calculation of surface heat transfer rates. Small exit nozzle, 9.5° plate inclination . . . . .	138
3.11 Composite boundary layer calculations of surface heat transfer rates, large exit nozzle, 19.5° plate inclination . . . . .	139

PART 1

INTRODUCTION AND BOUNDARY LAYER CALCULATIONS

## 1. Introduction

The Free Piston Shock Tunnel, as described by Stalker (1967) is unique in its ability to produce very high enthalpy gas flows well in excess of 12 eV or 7000 cal/gm. The object of this paper is to report the results of a theoretical and experimental study into the nature of a laminar boundary layer formed on an inclined flat plate in such a flow.

An important subsidiary investigation was made of the nozzle operation of a reflected shock tunnel with special attention being given to the possible effects of Helium gas contamination upon the flow characteristics.

At hypersonic gas flow speeds, as produced by the Free Piston Shock Tunnel, the dissipated kinetic energy will cause ionization of the test gas. The presence of free electrons greatly modifies the viscosity and thermal conductivity of the gas, and the solution of the boundary layer problem becomes difficult.

Taking the y-axis normal to the plate surface, the equations for a reacting gas boundary layer (neglecting thermal diffusion) are<sup>1</sup> on two dimensions:

Conservation of Mass:

$$\frac{\partial \rho u r^j}{\partial x} + \frac{\partial \rho v r^j}{\partial y} = 0, \quad (1-1)$$

Conservation of Momentum:

$$\rho u \frac{\partial u}{\partial x} + \rho v \frac{\partial u}{\partial y} = - \frac{\partial P}{\partial x} + \frac{\partial}{\partial y} \left( \mu \frac{\partial u}{\partial y} \right), \quad (1-2)$$

---

<sup>1</sup>See Dorrance (1962), Chapter 2.

Conservation of Species:

$$\rho u \frac{\partial C_i}{\partial x} + \rho v \frac{\partial C_i}{\partial y} = \frac{\partial}{\partial y} \left( \rho D_i \frac{\partial C_i}{\partial y} \right) + \dot{w}_i, \quad (1-3)$$

Conservation of Energy:

$$\begin{aligned} \rho u \frac{\partial H}{\partial x} + \rho v \frac{\partial H}{\partial y} &= \frac{\partial}{\partial y} \left[ \frac{\mu}{Pr} \frac{\partial H}{\partial y} + \mu \left( 1 - \frac{1}{Pr} \right)^{\frac{1}{2}} \frac{\partial u^2}{\partial y} \right] \\ &- \frac{\partial}{\partial y} \left[ \left( \frac{1}{Le} - 1 \right) \rho D_i \sum_{i=1}^n h_i \frac{\partial C_i}{\partial y} \right], \end{aligned} \quad (1-4)$$

where

$j = 0$  for two dimensional flow,  $j = 1$  for axisymmetric flow,

$\rho$  = density of the total mixture,

$P$  = pressure of the total mixture,

$\mu$  = viscosity of the total mixture,

$C_i$  = the mass fraction of species  $i$ ,

$D_i$  = coefficient of diffusion of species  $i$  through the mixture,

$\dot{w}_i$  = mass rate of change of species  $i$  per unit volume  
(reaction rate),

$H = \frac{1}{2} u^2 + h$

$h = \sum C_i h_i$ ,

$h_i = \int c_{pi} dT + h_i^0$ ,

$h_i^0$  = Heat of formation of species  $i$ ,

$Pr = \text{Prandtl number} = \mu c_p / k$ ,

$k$  = thermal conductivity of the total mixture,

$c_p = \sum C_i c_{pi}$ ,

$Le = \text{Lewis number} = \rho D_i c_p / k$ .

These equations are nonlinear partial differential equations and are difficult to solve. Fay and Riddell (1958), using integral transformations suggested by Lees (1956), were able to separate the variables and reduce the relations to ordinary differential equations. The equations of Fay and Riddell are applicable to diatomic dissociating gas boundary layers formed over axisymmetric bodies of flat plates.

If the gas is in thermochemical equilibrium in the boundary layer, i. e.  $\dot{w}_i = \infty$ , only the transformed versions of equations (1-2) and (1-4) need be solved. Solution of the former will give the velocity profile, while solution of the latter will give the enthalpy profile. The criterion of chemical equilibrium will then permit the calculation of the temperature, density, and species profiles.

If the gas is assumed chemically frozen, i. e.  $\dot{w}_i = 0$ , equation (1-3) must be used in addition to the two mentioned. Equation (1-1) is used in the transformation of the other equations.

In the case of flow over a flat plate, there is no pressure gradient along the x-axis since the stream lines external to the boundary layer remain parallel to the surface.

In the equations of Fay and Riddell, the transport properties of thermal conductivity, viscosity, and diffusion appear in dimensionless groupings as the Prandtl number, Lewis number, and the density viscosity product; the latter is defined by

$$\frac{\rho \cdot \mu}{\rho_\omega \mu_\omega}, \quad (1-5)$$

where the subscripts refer to conditions at the plate surface or wall. It should also be noted that the Prandtl number, Lewis number, and

density-viscosity product appear in the transformed equations of motion as parts of derivatives.

Fay and Riddell (1958) numerically integrated the transformed equations and obtained solutions at the stagnation point. They allowed the density-viscosity product to vary throughout the boundary layer, but set the Prandtl number equal to 0.71. The Lewis number was assigned values of 1.0, 1.4, or 2.0. The viscosity was calculated using Sutherland's formula.

Fay and Kemp (1963) extended the work of Fay and Riddell to an ionizing diatomic gas. The density-viscosity product was replaced by a density-thermal conductivity product. The contribution of the free electrons was taken into account in the case of total thermal conductivity, but not in the determination of the total viscosity. Fay and Kemp integrated the boundary layer equations with a varying Prandtl number, but the Lewis number was set to constant values between 0.3 and 1.0.

Finson and Kemp (1965) analyzed the problem of stagnation point heat transfer in ionized monatomic gases. The effect of free electrons on the viscosity was estimated from the pure ion thermal conductivity, using perfect gas relations. This theory gave good agreement with the low Mach number data of Rutowski and Bershadter (1964), but the measurements of Reilly (1964) at Mach 12 (a stagnation enthalpy of approximately 2000 cal/gm) were about 40% lower than the theory would predict.

Back (1967) studied laminar boundary layer heat transfer from a partially ionized monatomic gas. He held the Prandtl and Lewis numbers constant at values ranging from 0.1 to 0.67 and 0.25 to 2.0, respectively. The density-viscosity product was defined at a value of unity for all calculations.

Knöös (1968) investigated the equilibrium boundary layer structure in a 1 eV shock generated plasma flow. This work demonstrated that the viscosity, thermal conductivity, and density-viscosity product could all vary greatly throughout the boundary layer, and consequently, setting the density-viscosity product equal to a constant was a poor assumption.

High enthalpy gas flows are produced in the laboratory by allowing the reflected shock region of a shock tube to act as a reservoir for a nozzle. A driver gas (usually Hydrogen or Helium) is contained in a high pressure region, separated by a diaphragm from the shock tube which contains the test gas. The pressure of the driver gas is raised until the diaphragm bursts, and the consequent shock front followed by a driver-test gas contact surface travels down the tube and reflects at the end wall.

The Free Piston Shock Tunnel developed by Stalker (1967) differs from others in the method used to raise the pressure of the driver gas. This is illustrated in Figure 1.1. The piston compresses the driver gas until the pressure is raised to the point where the main metal diaphragm is burst. The principal performance difference is in the flow stagnation enthalpies that are produced. In conventional high enthalpy shock tunnels, the driver gas is ignited to produce high pressure and stagnation flow enthalpies approaching 3000 cal/gm. The Free Piston Shock Tunnel operates normally with flow stagnation enthalpies at, or in excess of, 7000 cal/gm.

A major problem arises in shock tunnels when the reflected shock front interacts with the shock tube boundary layer. Kaegi and Muntz (1964) investigated the test flow duration of a hypersonic reflected shock tunnel, using a combustion driver. Their results indicated that

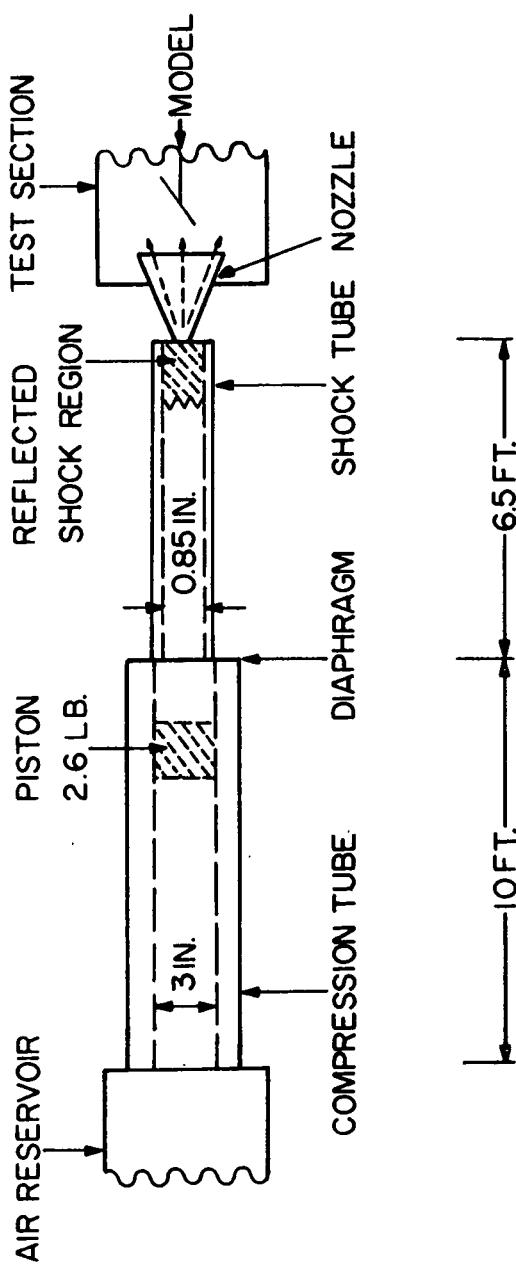


Figure 1.1

Schematic drawing of Free Piston Shock Tunnel, "T2," of the A. N. U. Aerophysics Laboratory

driver-test gas mixing significantly reduced test times at high enthalpy conditions. Davies (1965) and more recently Davies and Wilson (1969) have theoretically investigated this problem using the bifurcation model of Mark (1957). They suggest that the reflected shock boundary layer interaction will permit early contamination of the test gas by the driver gas.

Bull and Edwards (1968) experimentally studied the reflected shock interaction process in a shock tube and found that the driver gas appeared much earlier than predicted on the basis of a simple shock tube theory. Their measurements were in close agreement with the predictions of Davies (1965).

Slade (1970) experimentally studied this problem using a quadrupole mass spectrometer and confirmed that low level contamination may occur quite early in the test run.

In the very high enthalpy flow of this investigation, the transport properties of viscosity and thermal conductivity will vary greatly across the boundary layer. In order to determine the importance of these variations in relation to the overall boundary layer solution, it was decided to integrate the equations of motion, taking into account not only the differing values of viscosity, thermal conductivity, Prandtl number, Lewis number, and specific heat at each level in the boundary layer, but also the gradients or derivatives of these quantities throughout the region.

Since there is the possibility of the presence of Helium in the boundary layer, it was decided that the equations of motion must be integrated in such a way as to allow the estimation of the effects of contamination.

The solution of the boundary layer problem is completely dependent upon the free stream conditions that are assumed to exist above it. The Free Piston Shock Tunnel is a relatively new device and therefore its characteristics are not as completely understood as with the older forms of shock tunnels. Consequently, it was deemed necessary to carefully investigate the nozzle flow. Special attention was given to any changes in the flow characteristics that might occur due to the Helium contamination.

The transport properties are changed primarily by the presence of free electrons. It seemed logical to carry out the work using a monatomic gas that would go directly to the ionized state. The thermodynamic relations for a monatomic gas are also more straightforward and convenient to use than a dissociating gas, since only the translational and ionized modes of energy need be considered.

Part 1 of this paper will examine the boundary layer problem. Theoretical solutions will be developed for very high stagnation enthalpy flow (in excess of 12 eV), first in the condition of thermochemical equilibrium and then in a chemically frozen state. Full consideration will be given to the variation of the transport properties, and the boundary layer equations will be integrated in a fully coupled manner using a "multiple shooting" technique. The results of these solutions will be used in a discussion of the physical processes that occur in the boundary layer.

Part 2 of this paper will investigate the problem of Helium contamination. Firstly, the pure Argon flow is calculated, and secondly, the calculations are repeated with various amounts of Helium assumed to be present. Boundary layer solutions for both equilibrium and

frozen cases are shown with Helium contamination. A relatively straight forward theory will be developed to facilitate clear understanding of the physical processes that will be altered, and to what extent, when Helium is present in the flow.

The experimental results and project summary are described and discussed in Part 3. Laboratory investigations include time resolved pitot pressure of the on axis nozzle flow and surface heat transfer measurements at several stations on the plate. It will be shown that neither the equilibrium nor frozen boundary layer solutions can adequately predict the surface heat transfer rate in a very high enthalpy flow. A crude theoretical model will be developed that will give satisfactory predictions.

## 2. Boundary Layers

The boundary layer equations of motion for a flat plate are partial differential equations and have an exact solution only at the stagnation point. Solutions can be readily found for the flat plate problem, however, at extreme values of the reaction rates, i. e.  $\dot{w}_i = 0$  for a "frozen" boundary layer and  $\dot{w}_i = \infty$  for an "equilibrium" boundary layer.

To invoke the concept of "similarity", it is necessary to find a suitable method of integral transformation to move the problem from the  $x$ ,  $y$  plane to a new plane where the partial differential equations will reduce to ordinary differential equations. The integral transformations used were

$$\eta = \frac{u_e}{(2\xi)^{\frac{1}{2}}} \int_0^y \rho dy, \quad (1-6)$$

and

$$\xi = \int_0^x \rho_w \mu_w u_e dx . \quad (1-7)$$

In modern high enthalpy boundary layer problems, the major interest is in heat transfer. With this in mind, Fay and Kemp (1963) suggested that the use of a density-thermal conductivity product is more appropriately used in the transformed equations of motion than the density-viscosity product.

For the purposes of this study, the use of viscosity in equation (1-7) offered some conceptual disadvantage. In dealing with ionized monatomic gases, the effects of ionization upon viscosity are less obvious than the effects upon thermal conductivity and specific heat. Thus, where possible, it seemed desirable to use the latter quantities in the boundary layer equations.

Parametric studies can be made of boundary layers assuming different values of Prandtl number, e.g. Back's work. In these cases, if the viscosity has been replaced with the other parameters mentioned, the problem is simplified significantly.

Consequently, equation (1-7) has been modified by use of the definition of the Prandtl number to the form

$$\xi = \int_0^x \frac{\rho_w k_w \text{Pr}_w}{c_{pw}} u_e dx . \quad (1-7a)$$

### Equilibrium Boundary Layer Equations

Application of equations (1-6) and (1-7a) to the Equations of Motion, equations (1-1) to (1-5), gave rise to the following results in the case of an equilibrium boundary layer:

momentum:

$$\frac{c_{pw}}{Pr_w} \frac{d}{d\eta} \left[ \frac{Y Pr}{c_p} \frac{d^2 f}{d\eta^2} \right] + f \frac{d^2 f}{d\eta^2} = 0 , \quad (1-8)$$

energy:

$$\frac{c_{pw}}{Pr_w} \frac{d}{d\eta} \left[ \frac{1 + A}{c_p} \frac{dg}{d\eta} \right] + \frac{f}{Y} \frac{dg}{d\eta} - \frac{c_{pw}}{Pr_w} \frac{u_e^2}{H_s} \frac{d}{d\eta} \left[ \frac{1 - Pr}{c_p} \frac{df}{d\eta} \frac{d^2 f}{d\eta^2} \right] = 0 , \quad (1-9)$$

where  $f' = u/u_e$  ,  $f = \int_0^\infty \frac{df}{d\eta}$  ,

$$g = (u_e^2/2 + h_i) / H_s ,$$

$$Y = \rho k / \rho_w k_w ,$$

$$A = (Le - 1) h_i \left[ \frac{d\alpha}{dh} \right] P ,$$

$$f(0) = f'(0) = 0 ,$$

$$g(0) = g_w ,$$

$$f'(\infty) = g(\infty) = 1 .$$

The rate of change of ionization with the specific enthalpy at constant pressure is directly determined using the equation for specific enthalpy and Saha's equation.

Pure Argon:

$$\left[ \frac{d\alpha}{dh} \right]_P = \left\{ \frac{5}{2} R_A (1 + \alpha) \frac{dT}{d\alpha} + \frac{5}{2} R_A T + I \right\}^{-1}, \quad (1-10a)$$

Helium-Argon Mixtures:

$$\begin{aligned} \left[ \frac{d\alpha}{dh} \right]_P = & \left\{ x_A \frac{5}{2} R_A (1 + \alpha) \frac{dT}{d\alpha} + x_A \frac{5}{2} R_A T + x_A I \right. \\ & \left. + x_H \frac{5}{2} R_H \frac{dT}{d\alpha} \right\}^{-1}, \end{aligned} \quad (1-10b)$$

where

$$\frac{dT}{d\alpha} = \frac{1}{2} \frac{\left[ \frac{3.8208}{P_A} \right] T^{3/2} \left[ \frac{5}{2} + \frac{\epsilon}{kT} \right] \exp \left[ -\frac{\epsilon}{kT} \right]}{\left[ \frac{\alpha^2}{1-\alpha^2} \right]^{\frac{1}{2}} \left[ \frac{\alpha^2}{1-\alpha^2} \right]^{3/2}}. \quad (1-11)$$

The number 3.8208 was obtained from the evaluation of the constant terms in Saha's equation, in c.g.s. units. It should also be emphasised that the pressure is assumed to remain constant throughout the boundary layer.

#### Frozen Boundary Layer Equations

If there are no chemical reactions in the boundary layer, the gas is considered chemically "frozen." The value of ionization at

any point in the boundary layer will be determined solely by diffusion.

The momentum equation, equation (1-8) is still valid. The role played by the Saha equation in the equilibrium case is now filled by an equation of species concentration. The energy equation is also rewritten in a different form.

Conservation of species:

$$Le \frac{c_{pw}}{Pr_w} \frac{d}{d\eta} \left[ \frac{Y}{c_p} \frac{dS_i}{d\eta} \right] + f \frac{dS_i}{d\eta} = 0 , \quad (1-12)$$

Energy:

$$\begin{aligned} \frac{d^2\Theta}{d\eta^2} + \left[ \frac{c_p}{c_{pw}} \frac{Pr_w}{Y} f + \frac{c_{pw}}{c_p} Le \alpha_e \frac{dS_i}{d\eta} \right] \frac{d\Theta}{d\eta} \\ + \frac{u_e^2 Pr}{T_e c_p} \left[ \frac{d^2 f}{d\eta^2} \right]^2 = 0 , \quad (1-13) \end{aligned}$$

where

$$\begin{aligned} S_i &= \alpha/\alpha_e , & S_i(0) &= 0 \text{ or } S_{iw} , \\ \Theta &= T/T_e , & \Theta(0) &= \Theta_w , \\ & & S_i(\infty) &= \Theta(\infty) = 1 . \end{aligned}$$

#### Boundary Layer Equations with Variable Transport Parameters

If a solution is desired which will include the effects of the transport property changes through the boundary layer, the quantities within the brackets in the above equations must be differentiated.

In the case of the equilibrium boundary layer, in this investigation, the following new parameters are defined; using the frozen specific heat,

$$C_1 = Y \cdot Pr / c_p ,$$

$$C_2 = (1 + A) / c_p , \quad (1-14)$$

and

$$C_3 = (1 - Pr) / c_p .$$

Equations (1-8) and (1-9) are then rewritten in the form

$$f''' + (k_1 f + c_1' / c_1) f'' = 0 , \quad (1-8a)$$

and

$$g'' + (C_2' / C_2 + K_2 f) g' - K_3 \left[ (f'')^2 + f' f''' \right] - \frac{u_e^2}{C_2 H_s} C_3' f' f'' = 0 , \quad (1-9a)$$

where  $K_1 = (Pr_w / c_{pw}) / C_1 ,$

$$K_2 = (Pr_w / c_{pw}) / (Y C_2) , \quad (1-15)$$

and  $K_3 = (u_e^2 C_3) / (H_s C_2) .$

In the solution of a frozen boundary layer with variable transport parameters, it is found that the momentum equation, in the form of equation (1-8), remains valid. One additional transport parameter is defined,

$$C_4 = Y / c_p \quad (1-14a)$$

and then equation (1-12) and (1-13) are modified to the following:

$$S_i''' + \left[ C_1'/C_1 + K_4 f/\text{Le} \right] S' = 0 , \quad (1-12a)$$

and

$$\Theta''' + \left[ C_4'/C_4 + K_4 f + K_L S_i' \right] \Theta' + K_T (f'')^2 = 0 , \quad (1-13a)$$

where

$$K_4 = (\text{Pr}_w / c_{pw}) / C_4 ,$$

$$K_L = (c_{pw} / c_p) \text{Le} \alpha_e , \quad (1-15a)$$

and

$$K_T = (\text{Pr} u_e^2) / (T_e c_p) .$$

#### Integration of the Boundary Layer Equations

Back (1967) assumed equation (1-8) to be of the form

$$f'''' + f f''' = 0 ,$$

and obtained solutions for the momentum equation by curve fitting the original Blasius solution with the proper scaling. Back then solved his equivalent equation to equation (1-9) via a Runge-Kutta integration. This procedure is valid only if all the transport properties are assumed constant in value - otherwise equations (1-8) and (1-9) are coupled. (It should be noted that in their paper, Fay and Riddell did integrate the equations in a coupled manner.)

In this work, the equations are coupled and integrated using the multiple shooting technique of Osborne (1969). This procedure is a modification of the standard initial value problem. In the latter, one assumes the boundary conditions at the surface, making a guess of the unknown values, and then integrates the problem to an upper limit of  $\eta \rightarrow \infty$ . The final values calculated (usually a  $\eta$  value of 3 to 5 gives a sufficiently good approximation to  $\eta \rightarrow \infty$ ) are compared with the upper boundary values that are known. The initial numbers used may be modified and the problem redone. The method is repeated until the final predictions and the upper boundary values are matched to the desired accuracy.

Two major problems with this type of solution are:

- (1) that there is sometimes instability in the differential equations (i.e. two possible solutions are close to one another) and
- (2) one must usually start with "good" guesses.

Osborne overcame these problems by dividing the boundary layer into a number of intermediate levels and then carrying out an initial value type solution from the  $i^{\text{th}}$  to the  $(i^{\text{th}} + 1)$  interface. He also developed a sophisticated method to ensure quick convergence of the problem. The starting "guesses" at each level need only be the free stream values.

A slightly modified Newton method was used in the overall calculation. Using the free stream values, the equations and their respective derivatives would be evaluated at each interface. Correction factors based on these derivatives would then be algebraically added to the first solution estimates, and the sum of the squares of the difference between the new values and the old was calculated. The procedure would be repeated many times. Final solutions were obtained when the sum of

the squares fell below a certain tolerance, or one of several other criteria were met.

Calculations were done on an IBM 360-50 computer, and the basic integration subroutine was the IBM supplied Runge-Kutta procedure, RKGS, which has a built in step size determination procedure. Appropriate substitutions were made to convert the problem to a system of first order, non-linear equations. Consequently, the equilibrium cases required solution of a set of five equations, and the frozen solutions were obtained by integrating a set of seven equations. As many as 100 intermediate levels were used, but generally the division of the boundary layer into 50 layers proved more than adequate for the multiple shooting.

It was necessary to obtain an accurate estimate of the derivatives of the transport parameters.<sup>1</sup> In this study, all these values were calculated numerically from data of each individual solution.

Initially, the problem was solved with the transport parameters held constant at the free stream values. Based on this solution, the transport parameters were recalculated throughout the boundary layer, and the new table of values stored in the computer. The program then looped, and the second time around the required derivatives were estimated using the first differences from the tabulated data. The looping could be repeated as many times as desired.

The major changes occurred in the solution at the second loop. The convergence time of subsequent loops increased as smaller and smaller corrections were applied. The solution was normally terminated after the second looping was completed.

---

<sup>1</sup> Transport "parameters" will be taken as the newly defined quantities of equation (1-14) and (1-14a). Transport "properties" will refer to viscosity, thermal conductivity, and diffusion.

### Displacement Thickness

The effective physical thickness which the boundary layer exhibits in changing or displacing the flow of the free stream gas, is called the "displacement thickness" and is defined by

$$\delta^* = \int_0^\infty \left[ 1 - \frac{\rho u}{\rho_e u_e} \right] dy . \quad (1-16)$$

In terms of the transformation parameters this equation becomes

$$\delta^* = \frac{(2\xi)^{\frac{1}{2}}}{\rho_e u_e} \int_0^\infty \left[ \frac{\rho_e}{\rho} - f' \right] d\eta . \quad (1-17)$$

Using the results of the boundary layer integrations, equation (1-17) was in turn integrated using a 3/8 Simpson Rule. The value of  $\delta^*$  in terms of  $y$  was obtained using a quadrature formula derived from equation (1-6).

### Heat Transfer

The heat transfer to the surface of the flat plate, or in the boundary layer proper, is taken to be due to conduction and to diffusion of ion-electron pairs,

$$-q = k \frac{\partial T}{\partial y} + D_i \rho h_i \frac{\partial \alpha}{\partial y} , \quad (1-18)$$

where the negative sign is shown to indicate heat transfer to the surface.

Now

$$\frac{\partial T}{\partial y} = \frac{d\eta}{dy} \frac{dT}{d\eta} = \frac{\rho u_e}{(2\xi)^{\frac{1}{2}}} \frac{dT}{d\eta} = \frac{\rho u_e}{(2\xi)^{\frac{1}{2}}} T_e \frac{d\Theta}{d\eta} , \quad (1-19a)$$

and similarly

$$\frac{\partial \alpha}{\partial y} = \frac{\rho u_e}{(2\xi)^{\frac{1}{2}}} \alpha_e \frac{dS_i}{d\eta} . \quad (1-19b)$$

Using in turn equations (1-19a) and (1-19b), two relations for the heat transfer in transformed variables may be obtained,

$$-q = \frac{k \rho u_e T_e}{(2\xi)^{\frac{1}{2}}} \left[ \Theta' + \frac{L_e}{c_p T_e} \alpha_e h_i S_i' \right] , \quad (1-20a)$$

and

$$-q = \frac{k \rho u_e H_s}{(2\xi)^{\frac{1}{2}} c_p} \left[ (1 + A) g' - f' f'' \frac{u_e^2}{H_s} \right] , \quad (1-20b)$$

Equation (1-20a) was used in frozen boundary layer calculations and equation (1-20b) was employed in the equilibrium boundary layer solutions for both constant and variable transport parameters.

#### Transport Properties

The equations estimating the basic transport properties of thermal conductivity and viscosity for pure ionized Argon and mixtures of ionized Argon and neutral Helium, have been developed, Yanow (1971). Those equations were employed in the above calculations.

The diffusion term was calculated according to an equation given by Camac, et al. (1963) for the Lewis number, for Argon in a similar thermodynamic state as that in this problem,

$$Le = 0.255 (T/10^4)^{-0.16} \quad (1-21)$$

This formula was based on use of ambipolar<sup>1</sup> diffusion in the Argon. As Back (1967) has shown, the Lewis number is fairly constant about a figure of 0.25 under this condition.

#### Free Stream Conditions

The free stream conditions used in the boundary layer calculations are those that exist after the oblique shock which is formed at the leading edge of the inclined flat plate. Consequently, a range of conditions was obtained by adjusting the tilt of the plate. As the inclination angle is increased (rear of the plate raised), the boundary layer free stream Mach number and flow velocity will decrease while the pressure and density will increase. The range of conditions could be further expanded by using both a 7.5° half angle nozzle with an exit area ratio of 147 and a 15° half angle unit with an exit area ratio of 1204.<sup>2</sup>

---

<sup>1</sup>That is, diffusion of electron-ion pairs.

<sup>2</sup>The former will be referred to as the "small exit" nozzle, the latter as the "large exit" nozzle.

Nozzle Area Ratio	% He by Mass	Stag. Enthalpy (cal/gm)	Plate Angle (deg.)	Shock Angle (deg.)	Pressure (dyne/cm <sup>2</sup> )	Density (gm/cc)	Temperature (degree-K)	Velocity (cm/sec)	Mach No.
147	0.0	7,635	9.5	18.9	1.44 E+5	7.46 E-6	9,274	7.18 E+5	4.00
	0.99	7,522		20.1	1.04 E+5	5.77 E-6	7,984	7.29 E+5	4.20
	4.76	7,268		16.8	9.08 E+4	7.93 E-6	3,853	7.41 E+5	5.36
1204	0.0	7,635	19.5	28.2	4.68 E+4	1.65 E-6	13,637	7.10 E+5	3.26
136	0.0	7,635	—	—	1.14 E+5	6.35 E-6	8,518	7.36 E+5	4.83

(12.88 cm.  
small exit)

22 -

TABLE 1.1

Typical Free Stream Boundary Layer Conditions for a Distance up the Plate from the  
Leading Edge of 2 cm. and 12.88 cm. Downstream of Throat in Small Exit Nozzle.

In general, it was desired to maintain a high free stream velocity and Mach number while using different free stream pressures. These basic parameters would ensure a very high stagnation enthalpy hypersonic flow with different values of free stream density, temperature, ionization, and transport properties.

There are many complicating factors which had to be taken into account when making the final choices of plate inclination-nozzle conditions. These, and the calculations that were carried out, are discussed in detail in Part 2 of this paper. For the purposes of this immediate discussion, let it simply be stated that two conditions will be shown; a  $9.5^\circ$  plate inclination with the small exit nozzle, and a  $19.5^\circ$  plate inclination with the large exit nozzle. Table 1.1 is an abridged version of Tables 2.8a and 2.9b, and illustrates typical free stream conditions at a distance of 2 cm. up the plate from the leading edge. Table 1.1 also shows the calculated free stream conditions in the small exit nozzle at a distance of 12.88 cm. from the throat. This latter calculation is included for illustrative purposes, to show conditions before the oblique shock.

#### Equilibrium Boundary Layer Calculations

Locally similar solutions were calculated for distances up the plate from the leading edge of 1, 2, and 3 cm. These were "Pieced" together to form the total theoretical curves shown. Flow divergence was taken into account in the manner described in Part 2 of this paper. Experimental points will be discussed in Part 3.

However, before looking at the flat plate results, let us establish some basic concepts and determine what changes result in solutions when the transport properties are allowed to vary throughout the boundary layer.

If the transport parameters, as defined above, are held constant, the parameter  $K_1$  as given by equation (1-15) also becomes a constant. It has been found useful to consider  $K_1$  a direct function of the velocity profile, or simply a "profile factor." This concept is illustrated in Figure 1.2. The thickness of the boundary layer is inversely proportioned to  $K_1$ .

$K_1$  is the inverse of the classic density-viscosity product looked at in a different light ( i. e.  $(\rho \mu / \rho_w \mu_w)^{-1}$  ). Over the years, this parameter has been set equal to one so often that its physical significance has been overlooked. It has been called the profile factor in this study to emphasize its significance.

The profile factor is a valuable concept when dealing with variable transport parameters throughout the boundary layer. One can then consider the effects that the transport parameters have on the velocity profile at various points in the boundary layer. This is illustrated in Figure 1.3, where the results are plotted for the small exit nozzle wall boundary layer 12.88 cm. downstream.

At the surface  $K_1$ , by definition, equals unity. Coming off the plate, the profile factor increases but remains below the free stream value for a period. Eventually, the free flow value of  $K_1$  is not only reached, but greatly surpassed. After peaking in value,  $K_1$  quickly falls back to its final free stream figure. The effect of this behavior is to make the boundary layer effectively very thick at the base. .

A detailed explanation of the change in velocity profile is given in equation (1-8a). The temperature increases as it ascends from the surface, with a consequent increase in the thermal conductivity. However, simultaneously the density drops off at a quicker rate, as is shown in Figure 1.4. The result is that the parameter  $Y$  decreases in value.

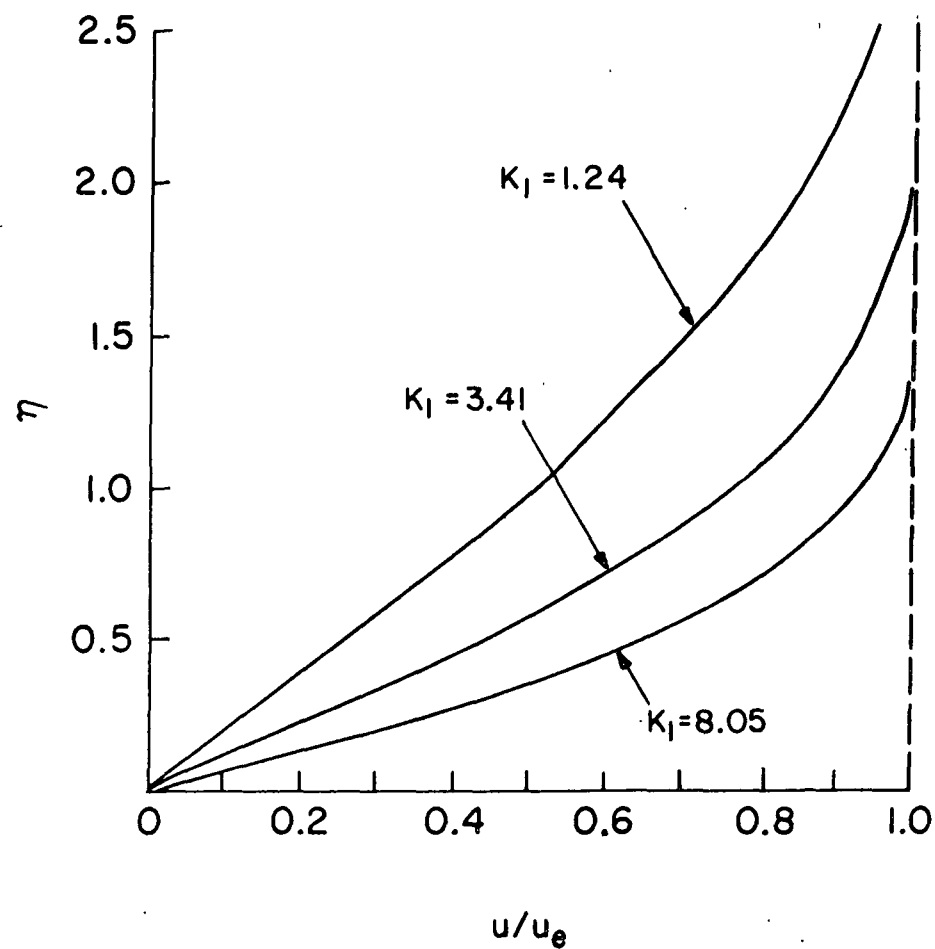


Figure 1.2

Velocity profiles for various values of the Profile constant, equilibrium boundary layer

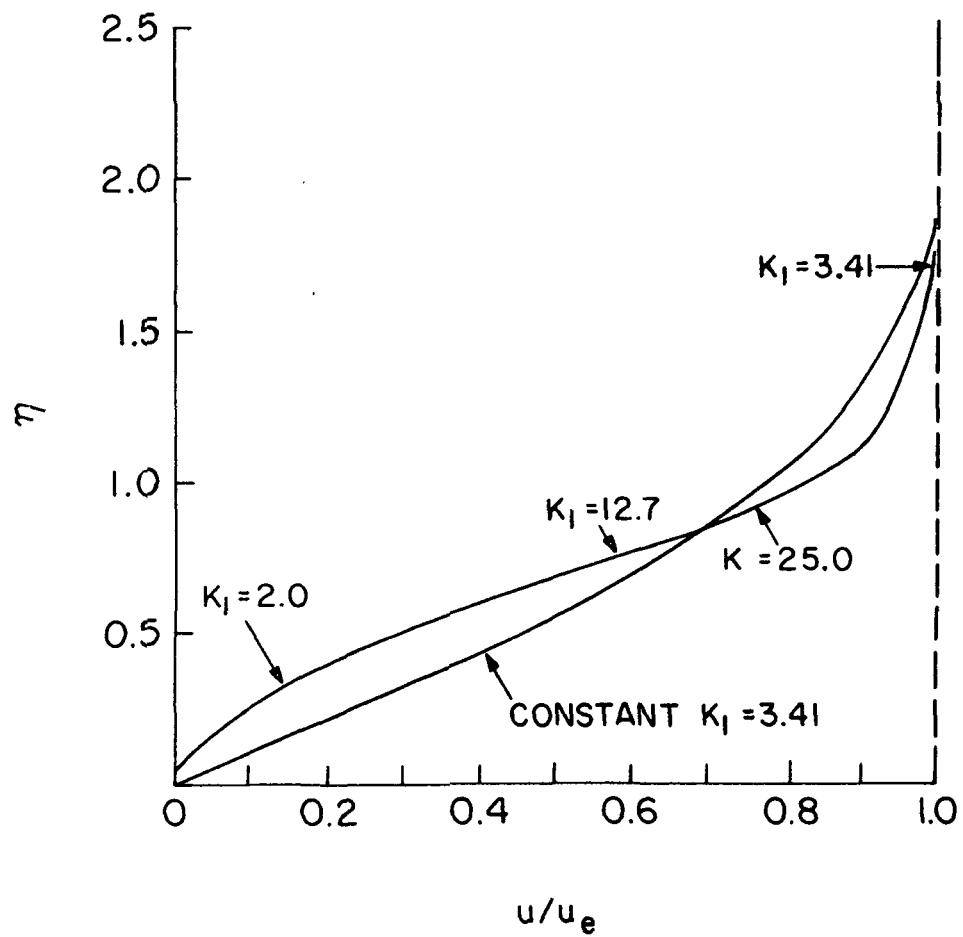


Figure 1.3

Velocity profiles for constant and variable transport parameters. Arrows are  $K_l$  at different levels

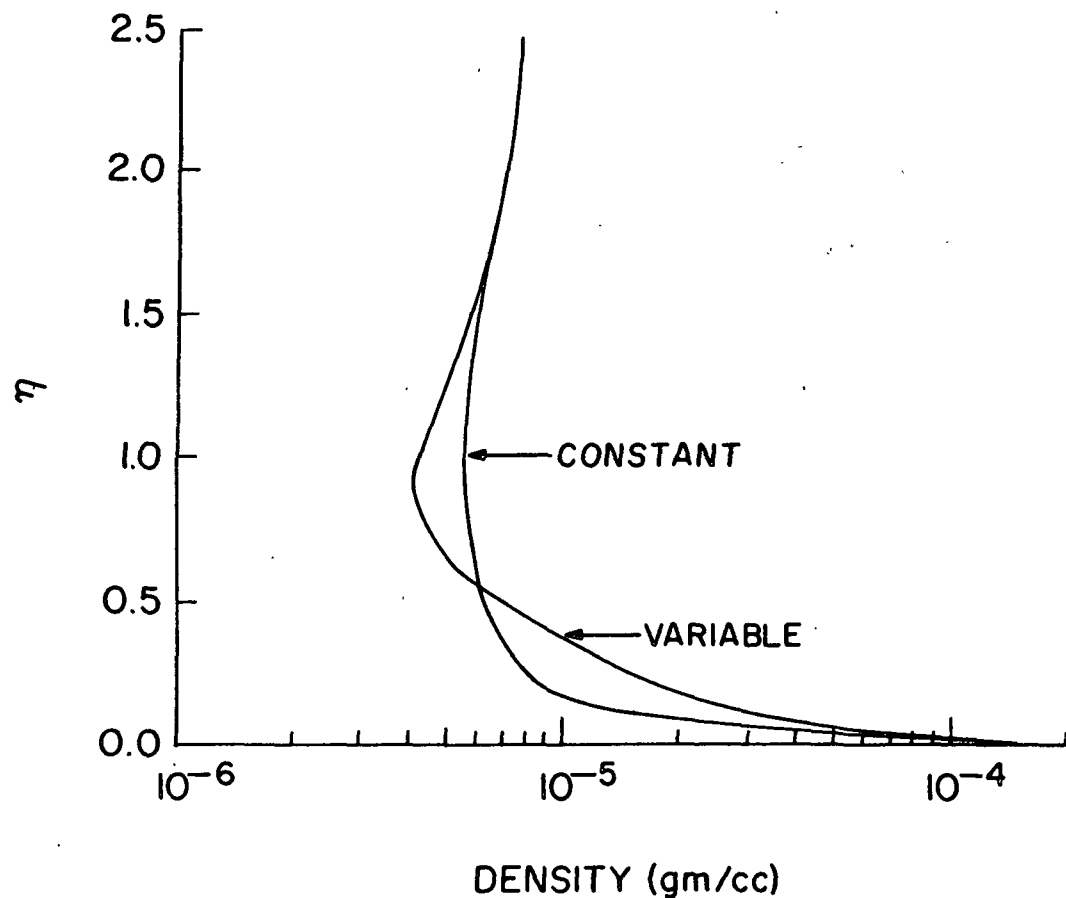


Figure 1.4

Density profiles for constant and variable transport parameter calculations, equilibrium boundary layer

This means that the derivative of  $C_1$  is negative and in fact is larger in absolute value than  $C_1$  itself. When  $C_1^1/C_1$ , a negative number greater in absolute value than one, is fed into equation (1-8a), this has a "braking" action on the integration with the observed effect on the velocity profile.

The inclusion of the variable transport parameters also has a marked effect on the enthalpy in the boundary layer. The new shape of the velocity profile produces a hot region well above the surface, but decreases the temperature gradient near and on the surface. These results are illustrated in Figures 1.5 and 1.6, the temperature and ionization profiles of the same boundary layer calculation of Figure 1.3.

The lowering of the wall temperature gradient will in turn produce a lower surface heat transfer rate. It should be realized that the above characteristics become more pronounced the higher the flow enthalpy, since the density drop off will be determined by the temperature gradient.

Figures 1.7 and 1.8 show two items that are of general interest in boundary layer studies. Figure 1.7 is the shear stress, defined by  $\mu (du/dy)$ , and it can be seen that there is a non-zero value at the surface. Although the velocity profile of the boundary layer with variable transport parameters appears as if it were suffering an adverse pressure gradient<sup>1</sup>, there should not be any separation at the surface. Figure 1.8 shows stagnation enthalpy as a function of velocity. As can be seen, the constant parameter calculation can be approximated with a linear relationship. This procedure will not be as good in the case of the variable calculation.

---

<sup>1</sup> The velocity profile with variable transport parameters also appears similar to that of a boundary layer with mass transfer (blowing).

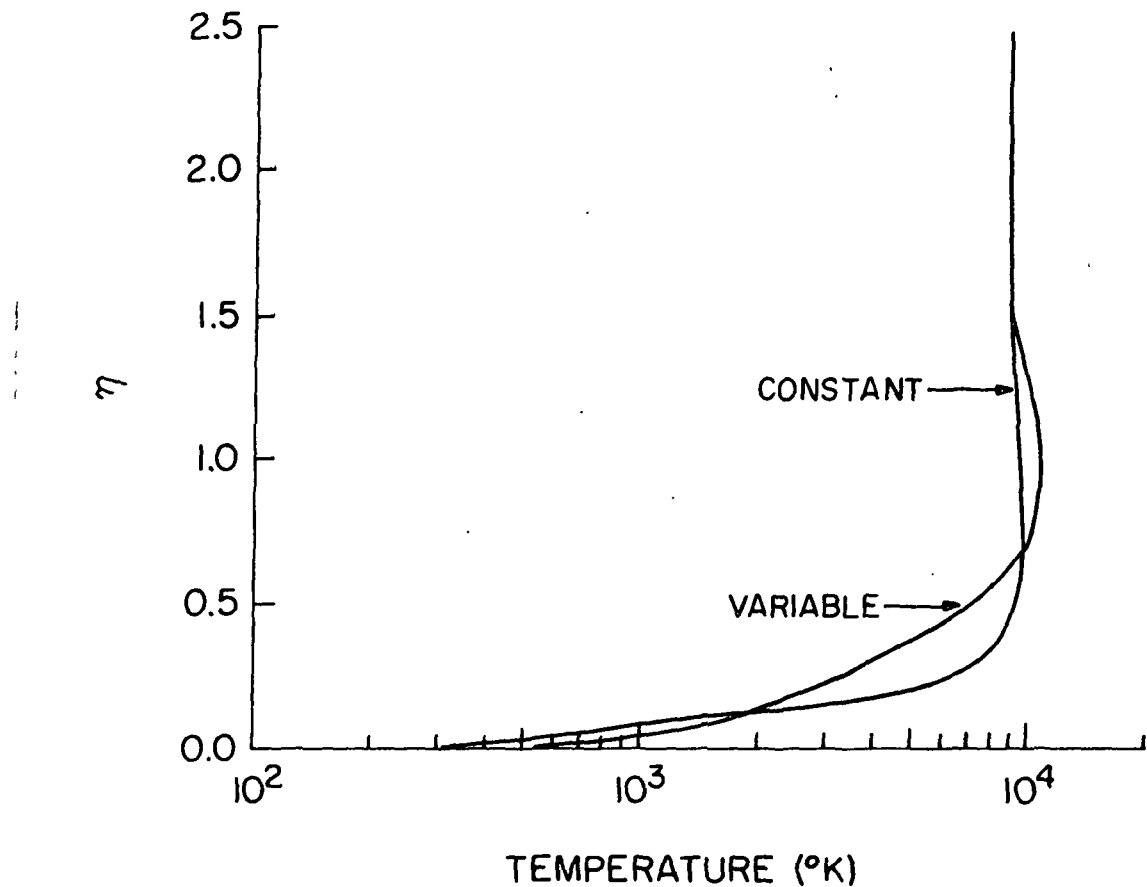


Figure 1.5

Temperature profile for constant and variable transport parameter calculations, equilibrium boundary layer.

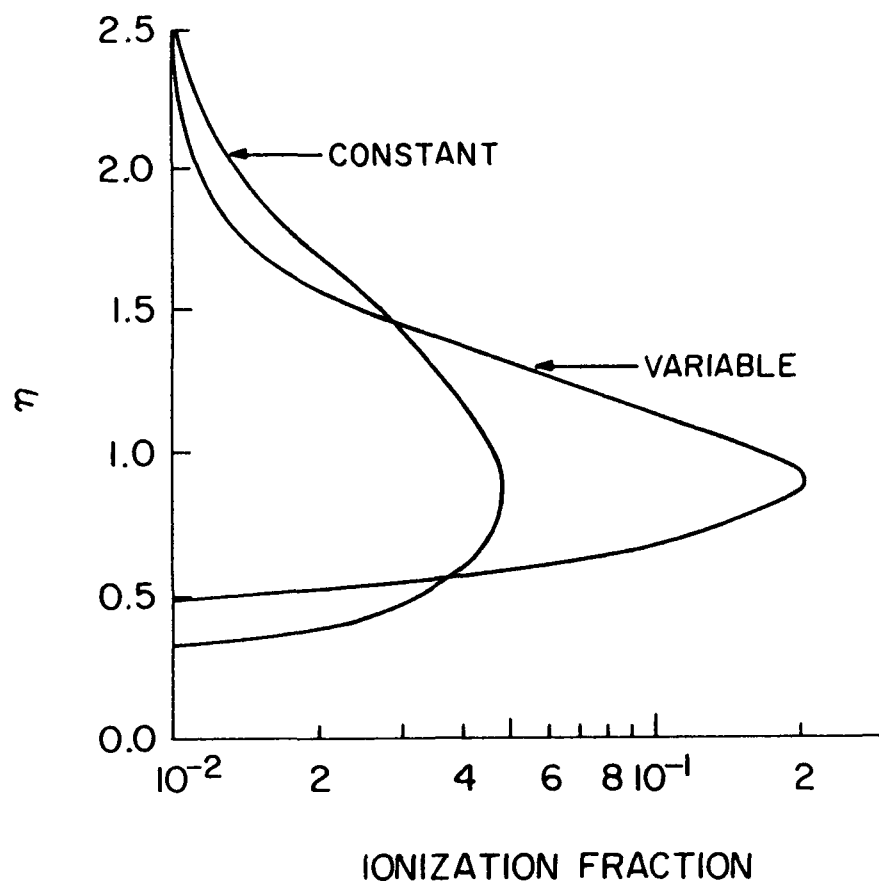


Figure 1.6

Ionization profile for constant and variable transport parameter calculations, equilibrium boundary layer

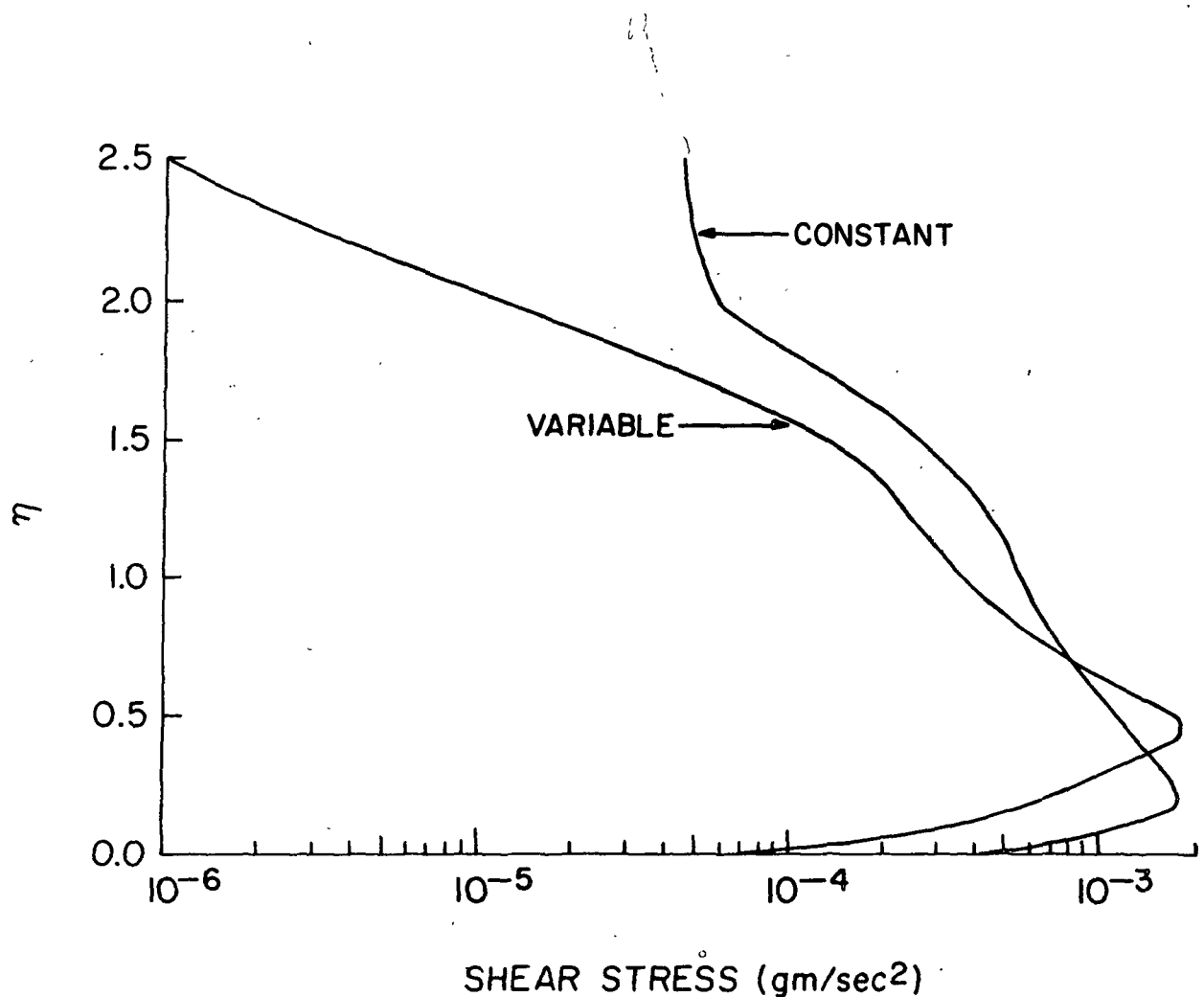


Figure 1.7

Shear stress for constant and variable transport parameter calculations, equilibrium boundary layer

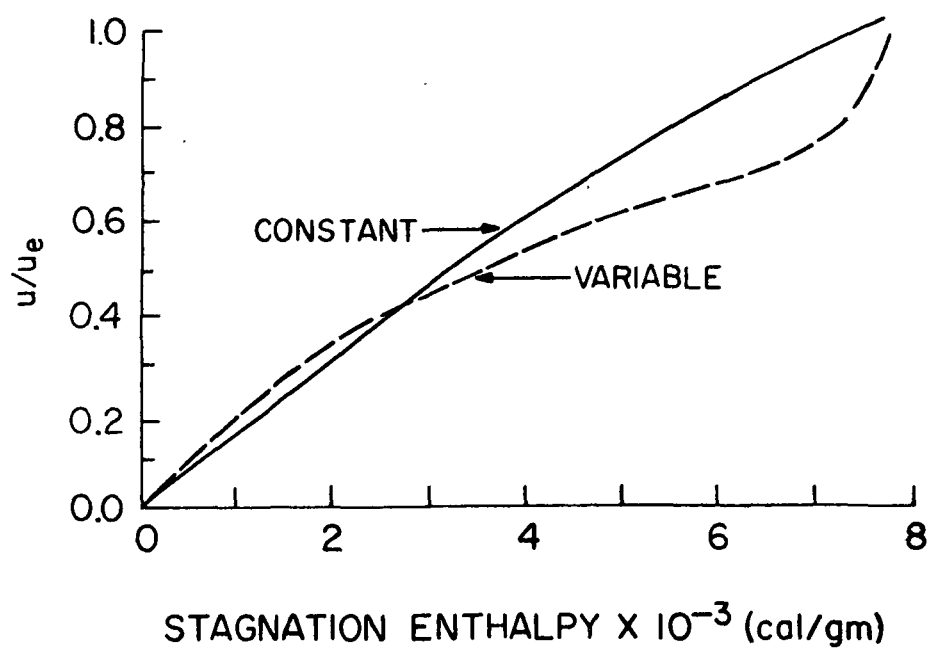


Figure 1.8

Stagnation enthalpy-velocity relationship for constant and variable transport parameters, equilibrium boundary layer, large exit,  $x_p = 1$  cm

With regard to the inclined flat plate in the test section, calculations and measurements will be shown for a  $19.5^{\circ}$  positive inclination with the large exit nozzle, and a  $9.5^{\circ}$  positive inclination with the small exit unit. These results will amply display the physics of the situation.

Figure 1.9 depicts the equilibrium velocity profiles. Figures 1.10, 1.11, and 1.12 show the calculated temperature, ionization, and density profiles for the  $19.5^{\circ}$  plate inclination, large exit case with variable transport parameters. Results for the distances up the plate from the leading edge of one and three cm. have been drawn to show the effects of flow divergence upon the internal structure of the boundary layer in an equilibrium condition.

The small exit  $9.5^{\circ}$  plate inclination results are alike, as might be expected from the similarity shown in the velocity profiles.

The flow divergence tends to lower the temperature and density throughout the boundary layer. In the case of ionization, the free stream value is lowered. At a distance of three cm., the curve is displaced upward. This last point can be seen by referral to Figure 1.13, which shows the conversion from the  $\eta$  to the  $y$  axis.

Figure 1.14 and 1.15 demonstrate the roles played by the transport properties in the equilibrium boundary layer. Figure 1.14 indicates the profiles of the thermal conductivity and viscosity. The thermal conductivity suffers a short term lowering of its value at about  $\eta = 0.5$ . This is attributed to the fact that the ion-atoms and ion-ion collision cross-sections are greater than the atom-atom. At the onset of ionization, the electron numbers are still very small, however, this number quickly builds up, and the electrons soon dominate with their

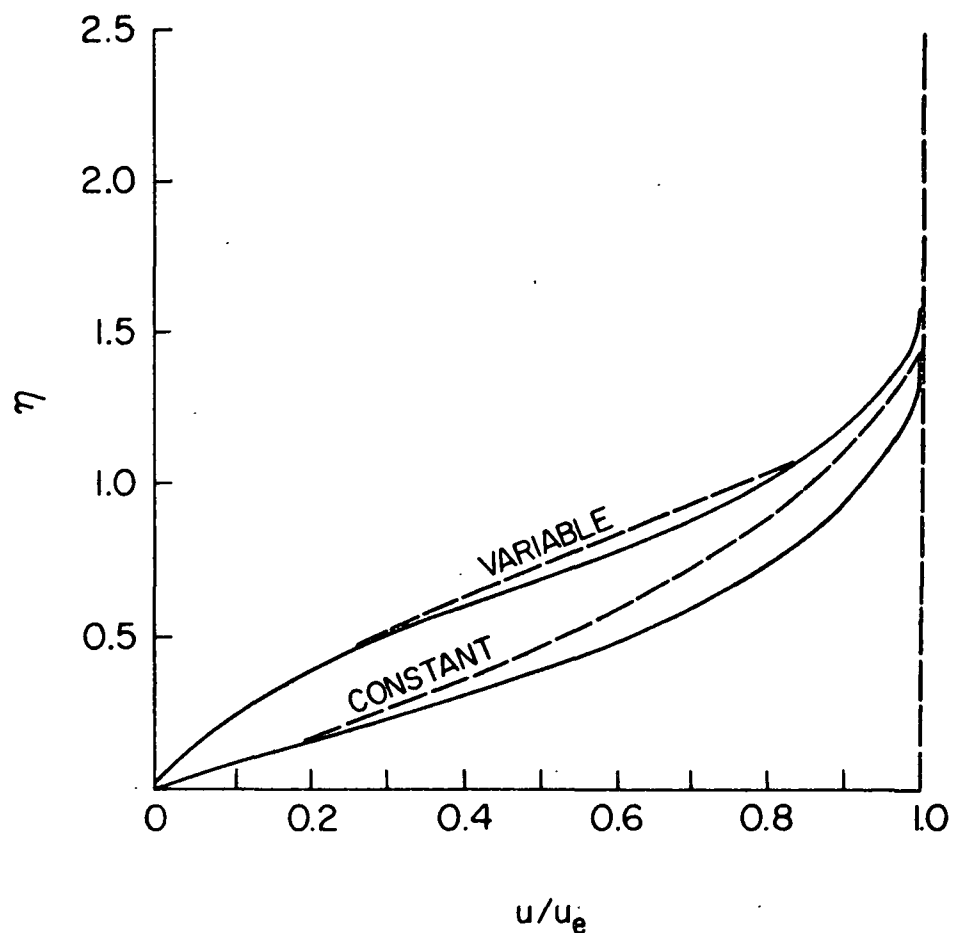


Figure 1.9

Equilibrium flat plate velocity profiles.  
Dotted lines are small exit nozzle,  $9.5^\circ$   
plate inclination. Solid lines are large exit  
nozzle,  $19.5^\circ$  plate inclination,  $x_p = 1 \text{ cm}$

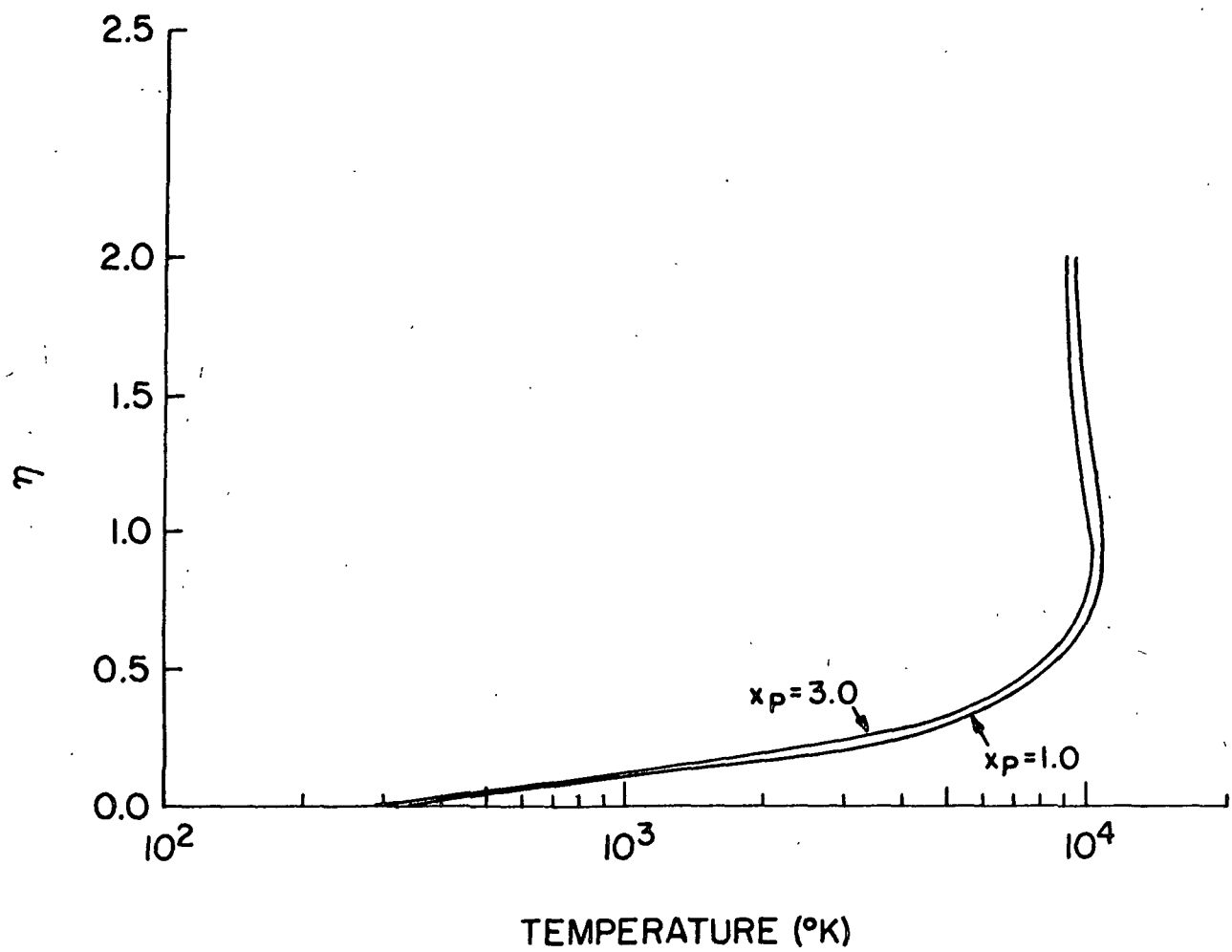


Figure 1.10

Temperature profile for variable transport parameter calculations, large exit nozzle, equilibrium boundary layer

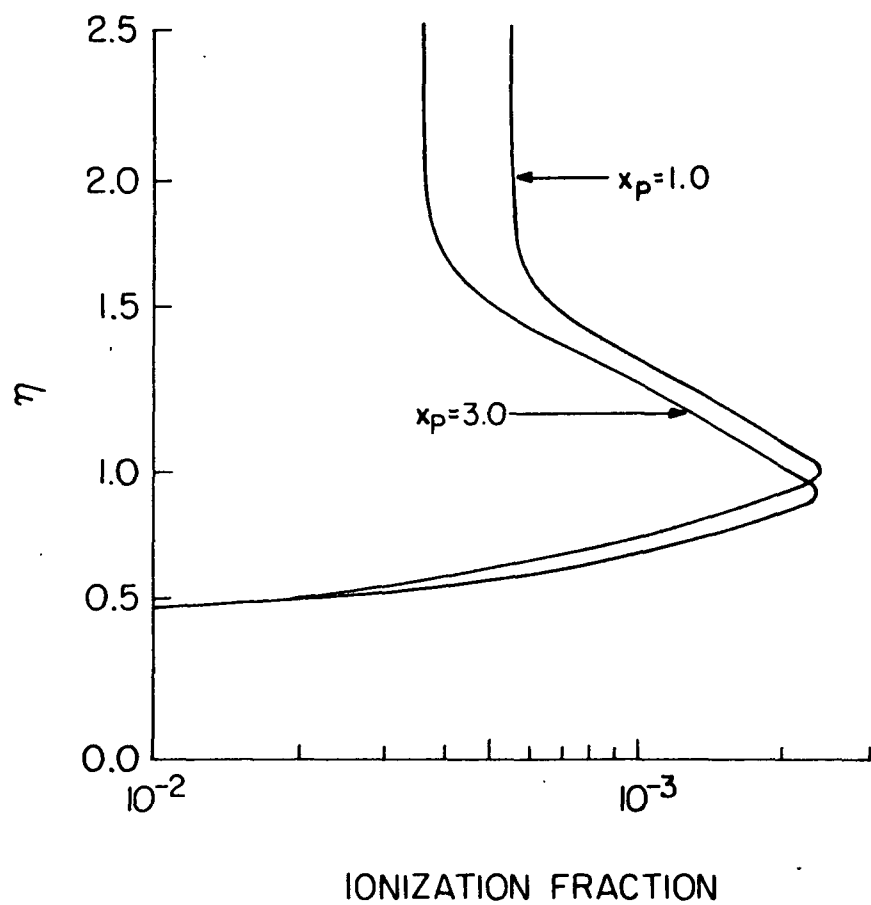


Figure 1.11

Ionization profile for variable transport parameter calculations, large exit nozzle, equilibrium boundary layer

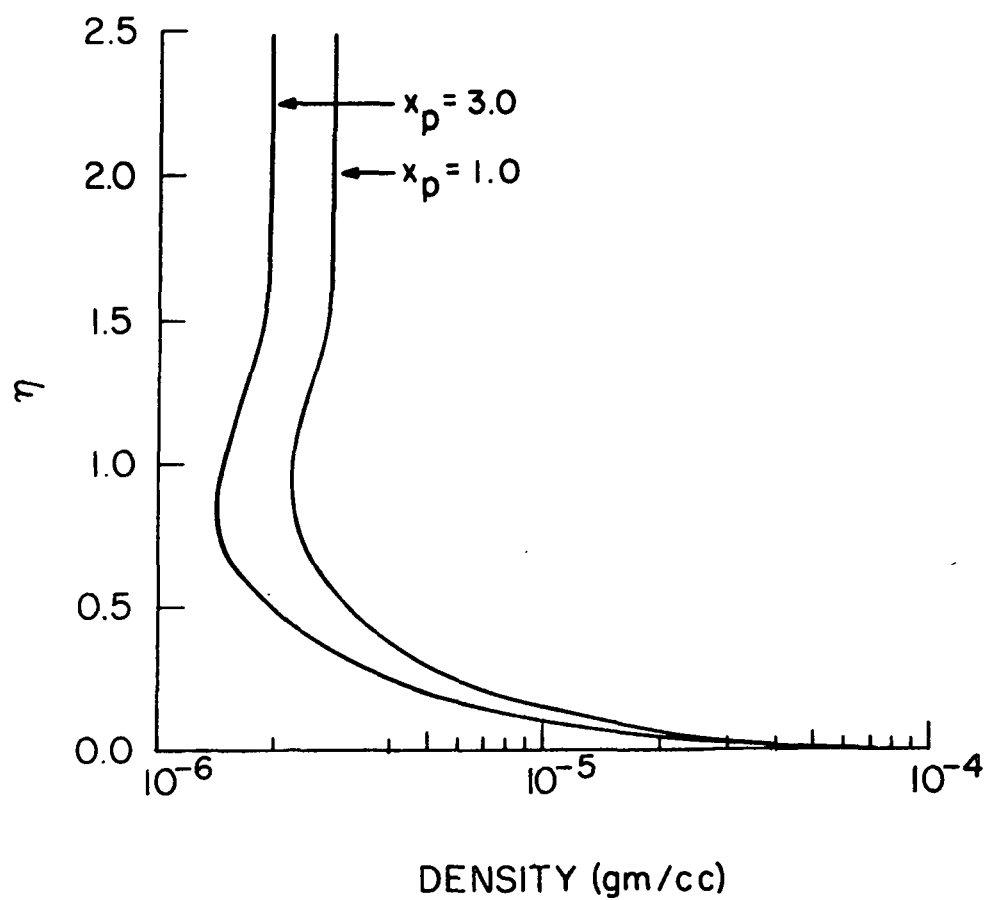


Figure 1.12

Density profile for variable transport parameter calculation,  
large exit nozzle, equilibrium boundary layer

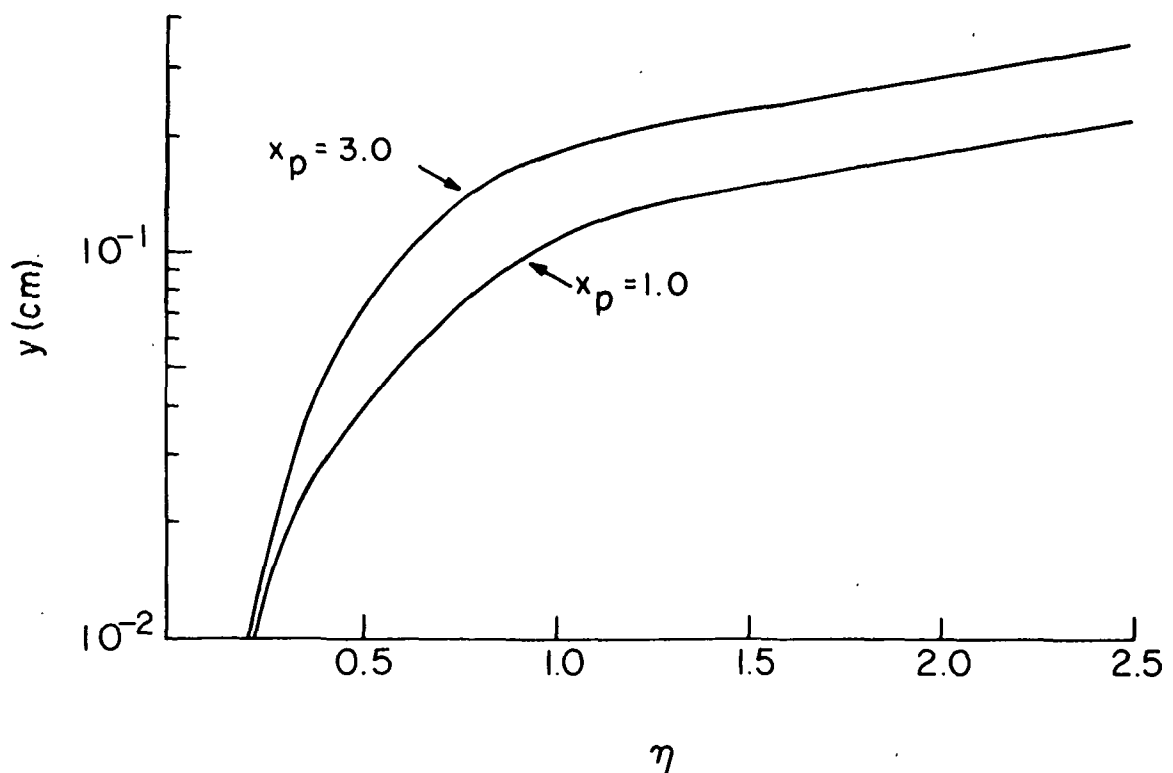


Figure 1.13

Conversion from  $\eta$  to y-axis for variable transport parameter calculations, large exit, equilibrium boundary layer

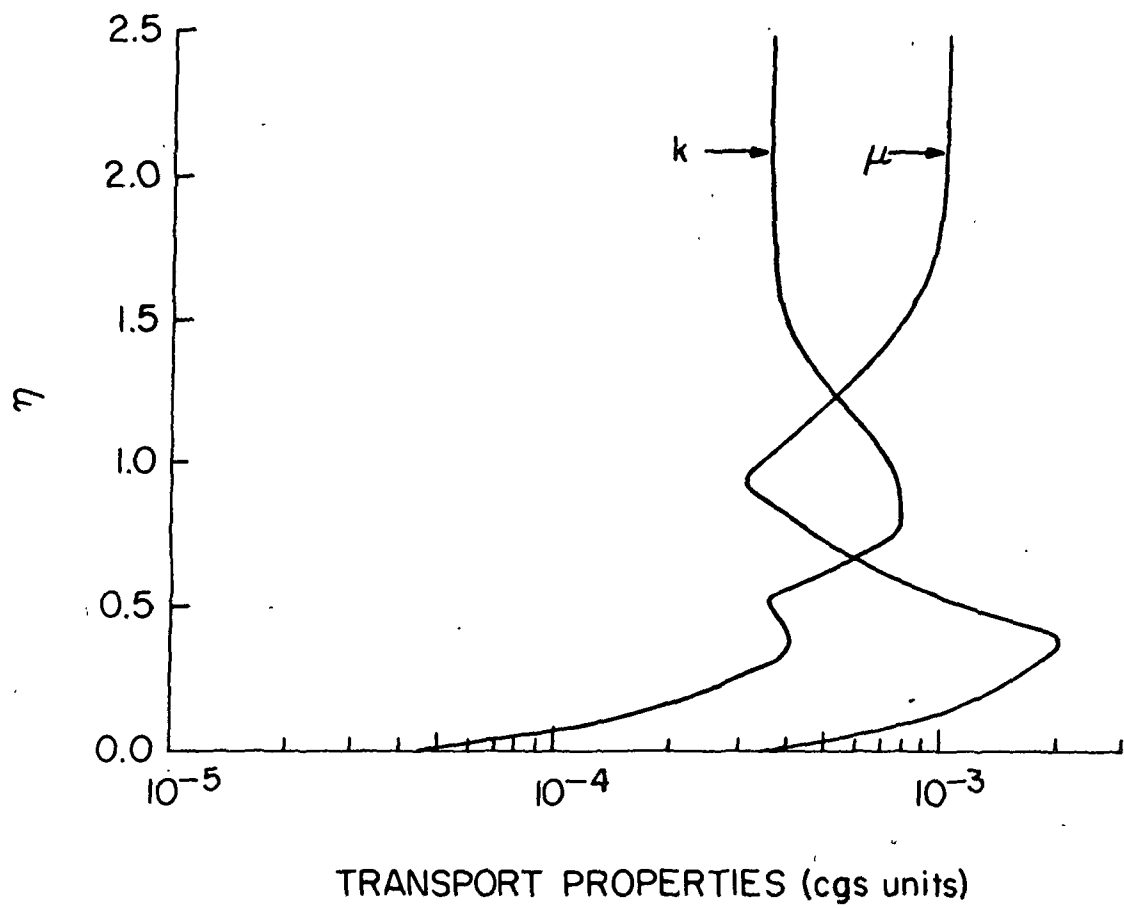
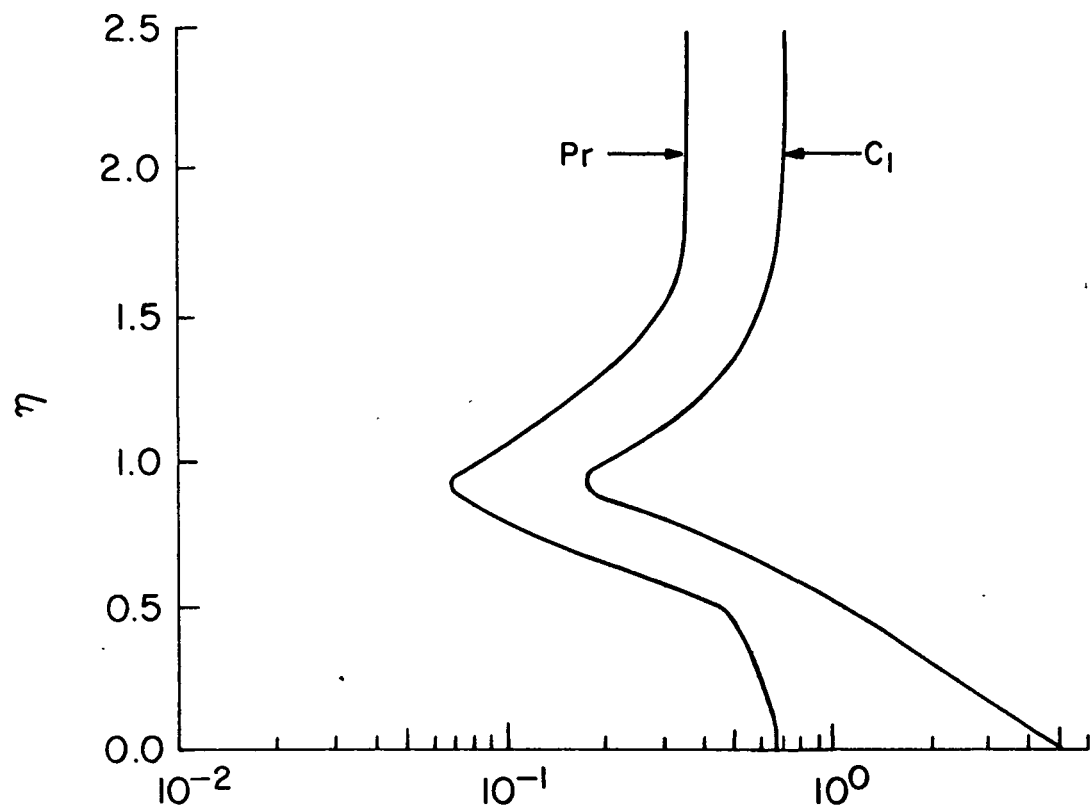


Figure 1.14

Thermal conductivity and viscosity for  
variable transport parameter calculation  
large exit nozzle, equilibrium boundary  
layer



### TRANSPORT PARAMETERS

Figure 1.15

Prandtl number and  $C_1$  for variable transport parameter calculation, large exit nozzle, equilibrium boundary layer

much larger thermal conductivity. The viscosity falls as the electron numbers build up. This is again a function of the ion-atom and ion-ion cross-sections.<sup>1</sup> The thermal conductivity peaks and the viscosity hits its minimum value at the point of maximum ionization.

Figure 1.15 discloses the profiles of the Prandtl number and the newly defined parameter  $C_1$ , as given in equation (1-14). The shape of the two is similar except in the very important lower regions where the Prandtl number goes to a constant limit, but  $C_1$  varies right into the plate surface. This behavior of  $C_1$  plays a major role in the variable transport parameter calculations.

Figure 1.16 shows the calculated surface heat transfer rates. The measurements will be discussed in Part 3. It is to be noted that a calculation which considers fully the variation of the transport properties gives a far lower heat transfer rate. This is due to the smaller temperature gradient at the surface that is predicted with the variable transport parameter calculation.

#### Frozen Boundary Layer Calculations

In the case of equilibrium, the boundary conditions of velocity and total enthalpy (along with pressure) were specified, but the temperature, ionization, and density take on different values, depending on the prediction of the Saha equation.

With a frozen boundary layer, the boundary conditions of velocity, temperature, and ionization, together with the pressure, are specified. The range of values which the thermodynamic and transport properties can take is much more limited, since the quantities are controlled by diffusion processes. Consequently, little difference was found between

---

<sup>1</sup> See Knöös (1968).

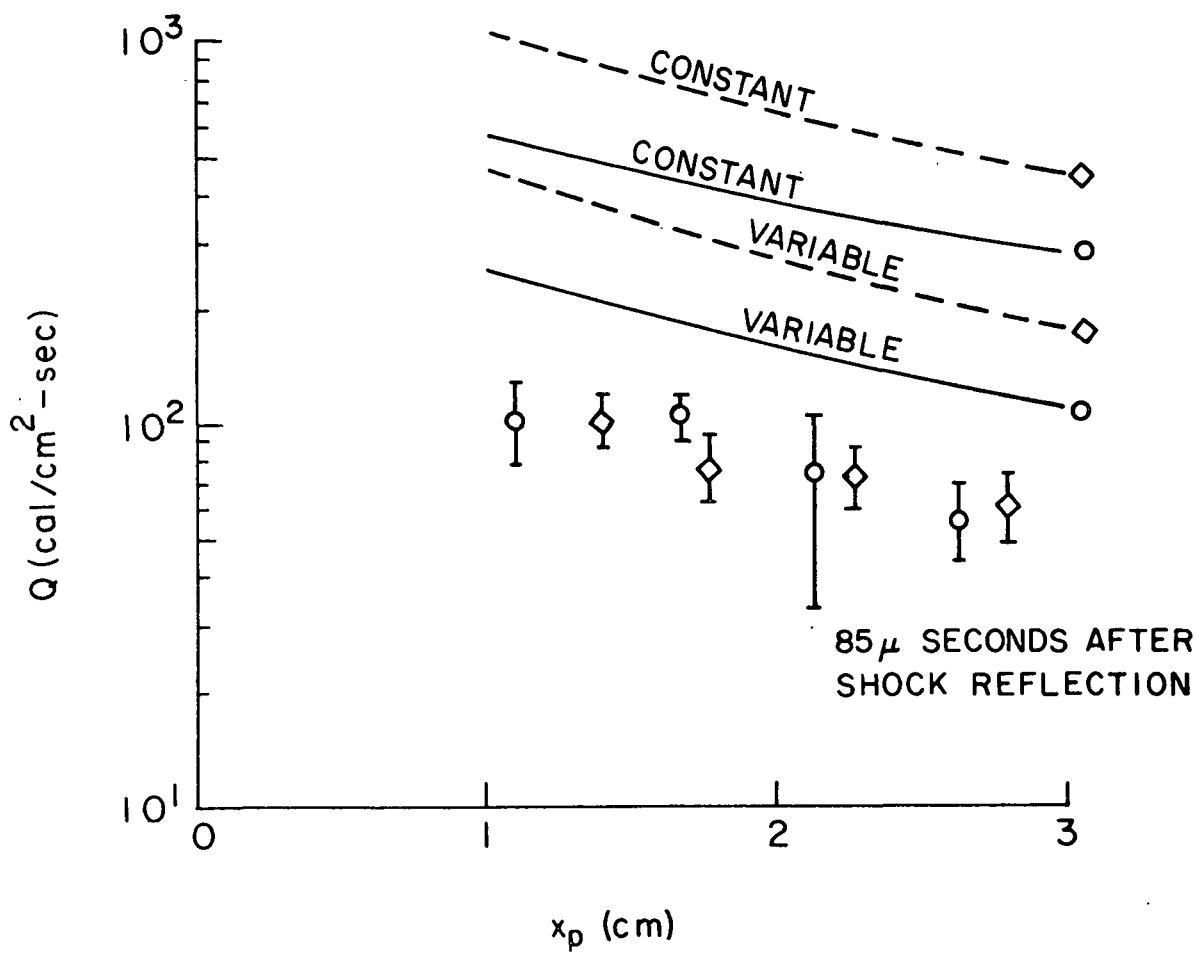


Figure 1.16

Heat transfer rates. Dotted lines ( $\diamond$  data) are small exit nozzle,  $9.5^\circ$  plate inclination. Solid lines ( $\circ$  data) are large exit nozzle,  $19.5^\circ$  plate inclination

constant and variable transport parameter frozen solutions. For example, the ionization does not obtain a value greater than the free stream figure. This is in contrast to the equilibrium calculation where the ionization reaches a peak value much bigger than the free stream ionization.

From a computer standpoint, the frozen solutions usually converged at a slow rate. After a series of survey calculations were made, it was decided that on a basis of computer economics the variable transport parameter frozen solutions could not be justified.

The free stream conditions used in a frozen boundary layer calculation pose a problem - if the free stream chemistry is frozen, the only ionization that would be in the flow is that which was present before the oblique shock. This would be zero in the case of the large exit nozzle, and about 1% in the case of the small exit. In order to allow a better comparison between the equilibrium and frozen boundary layer calculations, it was assumed that the free stream flow went to a state of thermochemical equilibrium after the oblique shock, and that only the boundary layer chemistry was frozen.

The results shown below will be for the same conditions, namely the small exit nozzle,  $9.5^{\circ}$  plate inclination, with a fully catalytic surface, with a fully non-catalytic surface, and at a distance up the plate of 1 cm. from the leading edge.

Figure 1.17 displays the velocity profiles. The surface recombination rate does have an effect upon the velocity in the boundary layer. If there is no recombination at the surface, the change of velocity in the boundary layer is more gradual and commences at a higher level than with the catalytic surface.

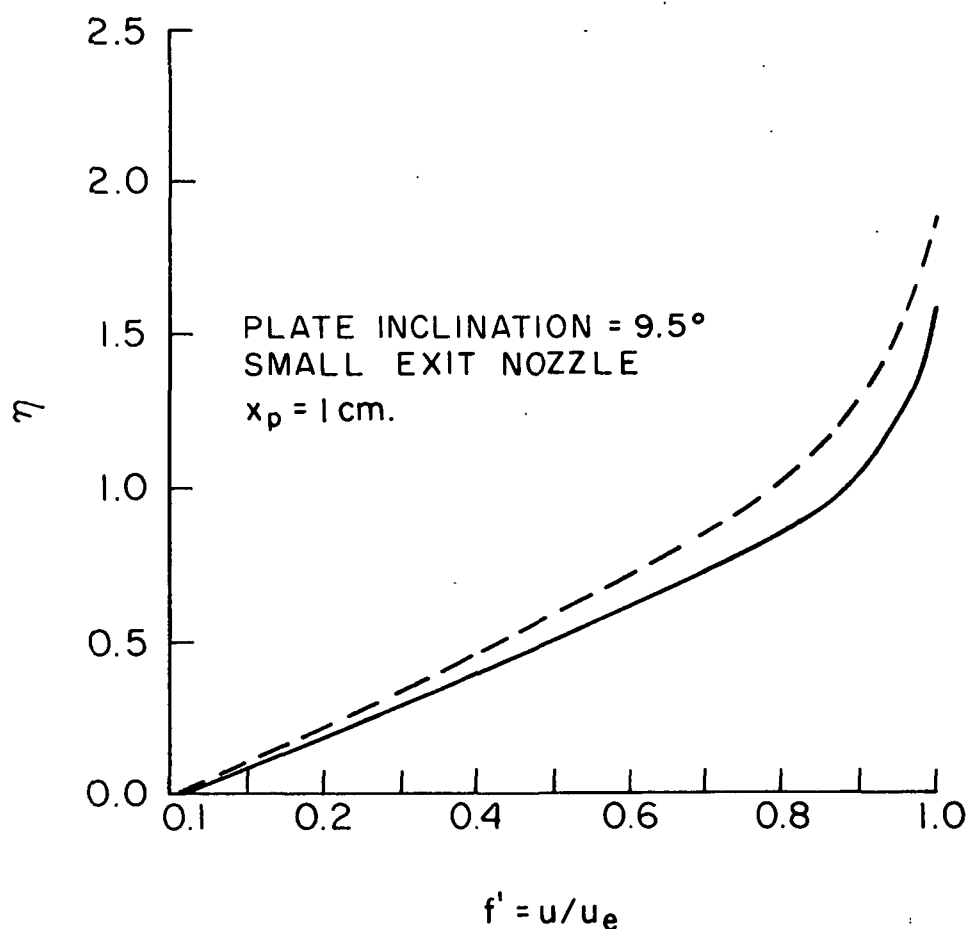


Figure 1.17

Velocity profile for frozen boundary layer.  
Transport properties set constant at free  
stream values. Solid line 100% catalytic  
surface; dotted line 100% non-catalytic  
surface

Figures 1.18, 1.19, and 1.20 exhibit the calculated temperature, density, and ionization profiles. The free stream values for these calculations are slightly different than the typical values shown in Table 1.1. For the work described below, these values are  $T_{\infty} = 9703^{\circ}\text{K}$ ,  $\rho_{\infty} = 9.69 \times 10^{-6}$  gm/cc, and  $\alpha_{\infty} = 0.034$ . The calculated differences between a catalytic and non-catalytic surface boundary layer<sup>1</sup> will, of course, be dependent on the amount of ionization that is present. It can be seen that free stream ionization levels as low as 3% will produce some change in the boundary layer structure. The ionization profile, with regard to the 100% catalytic surface, is determined by diffusion processes.

Figure 1.21 is to allow conversion from the  $\eta$  to the  $y$  axis, and Figure 1.22 is the calculated surface heat transfer rates for the catalytic and non-catalytic wall. The fully catalytic wall calculation, gives for all practical purposes the same surface heat transfer rates as with the constant transport property equilibrium boundary layer solution. This means that the heat energy transferred to the surface by conduction and diffusion processes will add up to give the same result in both cases. The non-catalytic surface has a lower heat transfer rate - if the parameter  $S_i^*$ , defined as  $\alpha/\alpha_e$ , is always equal to 1, then  $S_i^*$  must always be equal to zero. Therefore, the heat transfer component brought down to the surface by diffusion of electron-ion pairs is missing (reference to equation (1-20a) will verify). Dorrance (1962)<sup>2</sup> explains this physically by a "pile up" of diffusion-inhibiting blanket of unrecombined particles which reduces the heat transfer. The larger the free stream ionization, the larger will be the difference between the catalytic and non-catalytic surface heat transfer rates.

<sup>1</sup> i. e. Either complete ion-electron recombination or no recombination at the surface, respectively.

<sup>2</sup> See page 91 of reference.

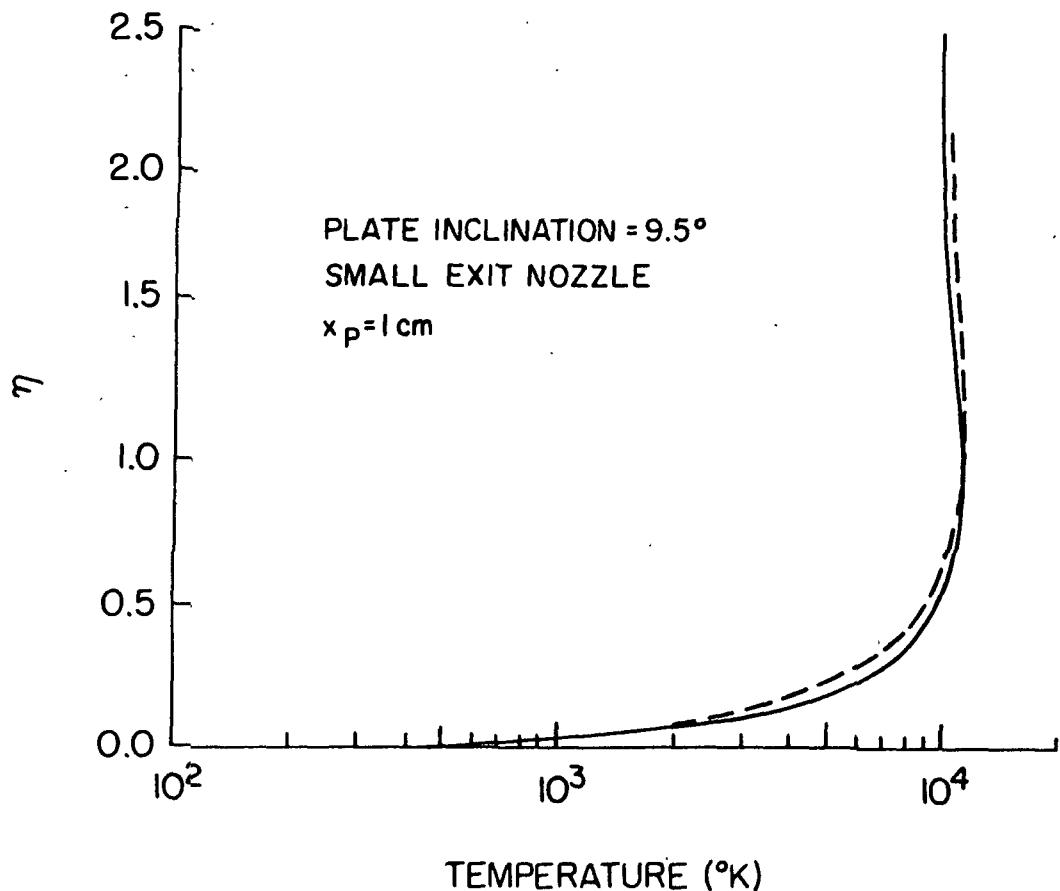


Figure 1.18

Temperature profile for frozen boundary layer. Transport properties set constant at free stream values. Solid line 100 % catalytic surface; dotted line 100 % non-catalytic surface.

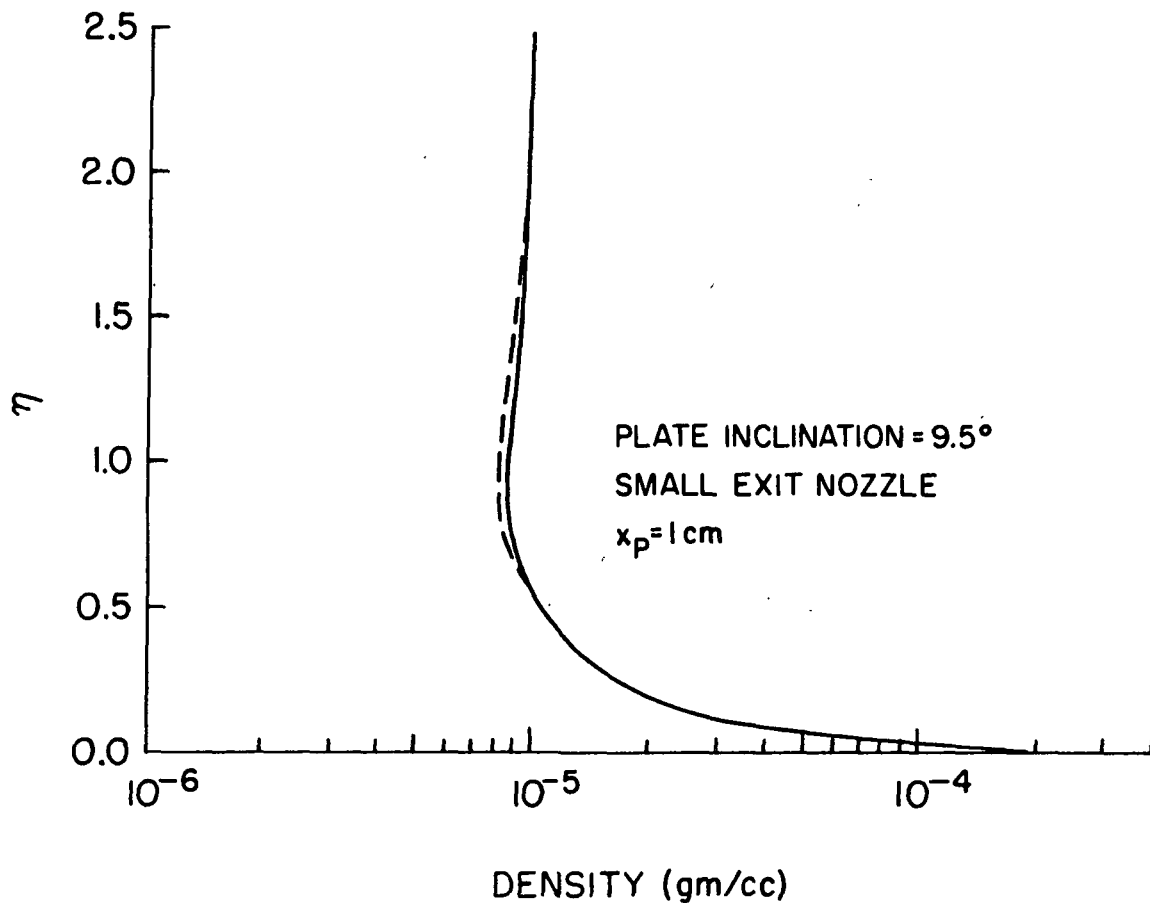


Figure 1.19

Density profile for frozen boundary layer.  
Transport properties set constant at free  
stream values. Solid line 100% catalytic  
surface; dotted 100% non-catalytic surface

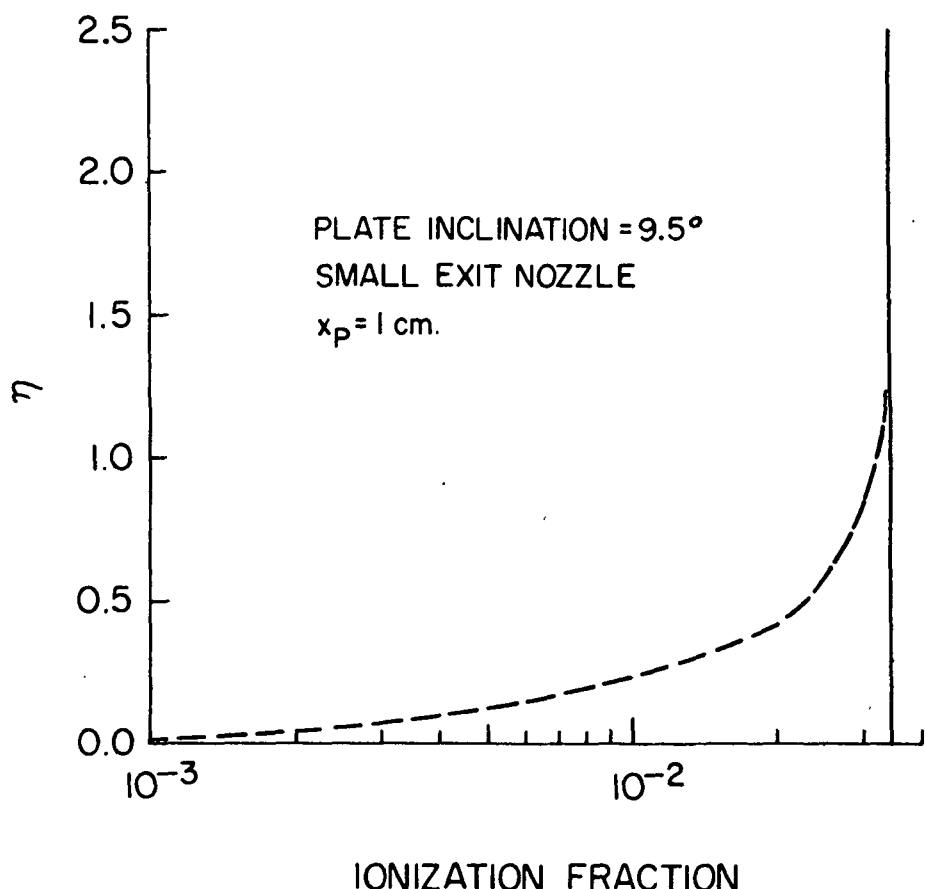


Figure 1.20

Ionization profile for frozen boundary layer.  
Transport properties set constant at free  
stream values. Solid line 100 % non-catalytic  
surface; dotted line 100 % catalytic surface

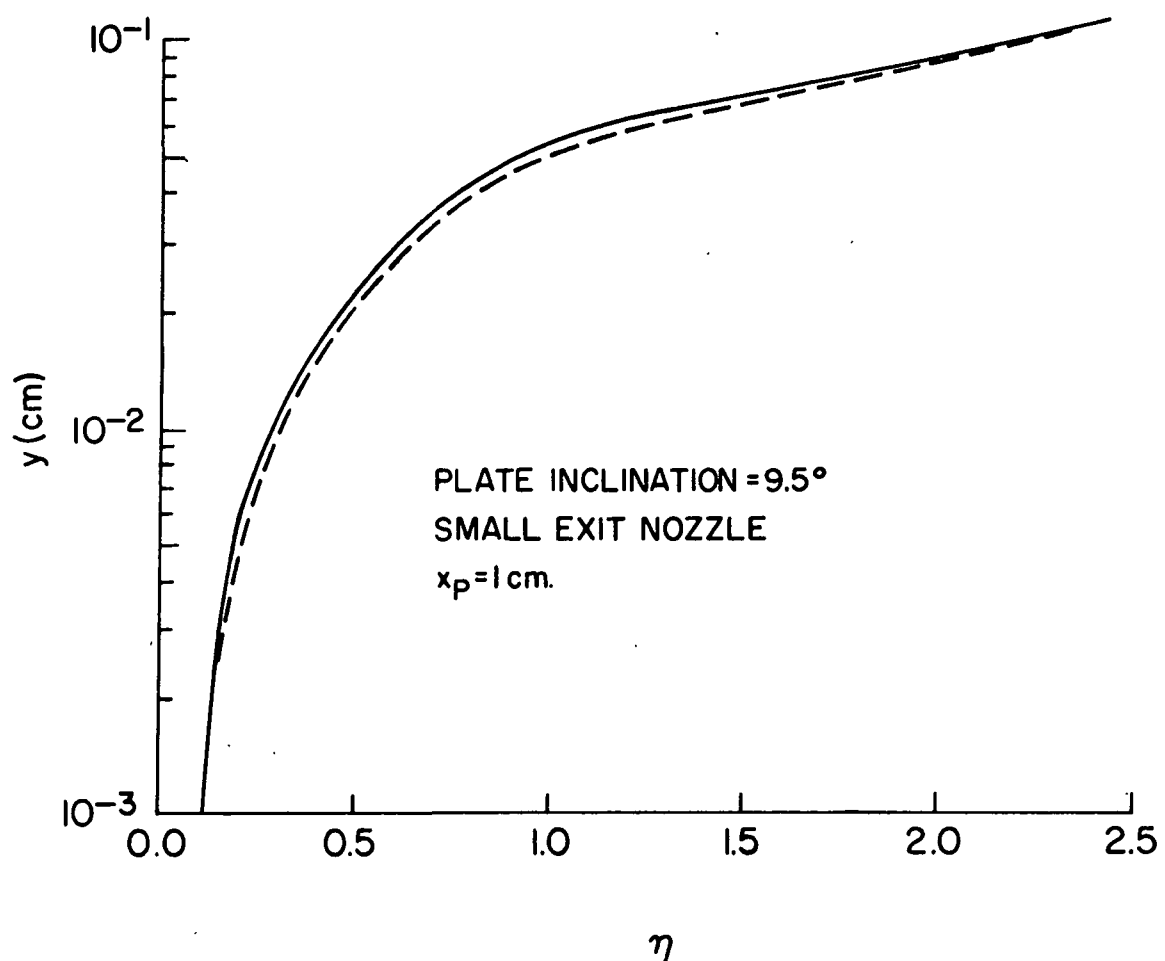


Figure 1.21

Conversion from  $\eta$  to  $y$ -axis for frozen boundary layer. Transport properties set constant at free stream values. Solid line 100% catalytic surface; dotted line 100% non-catalytic surface

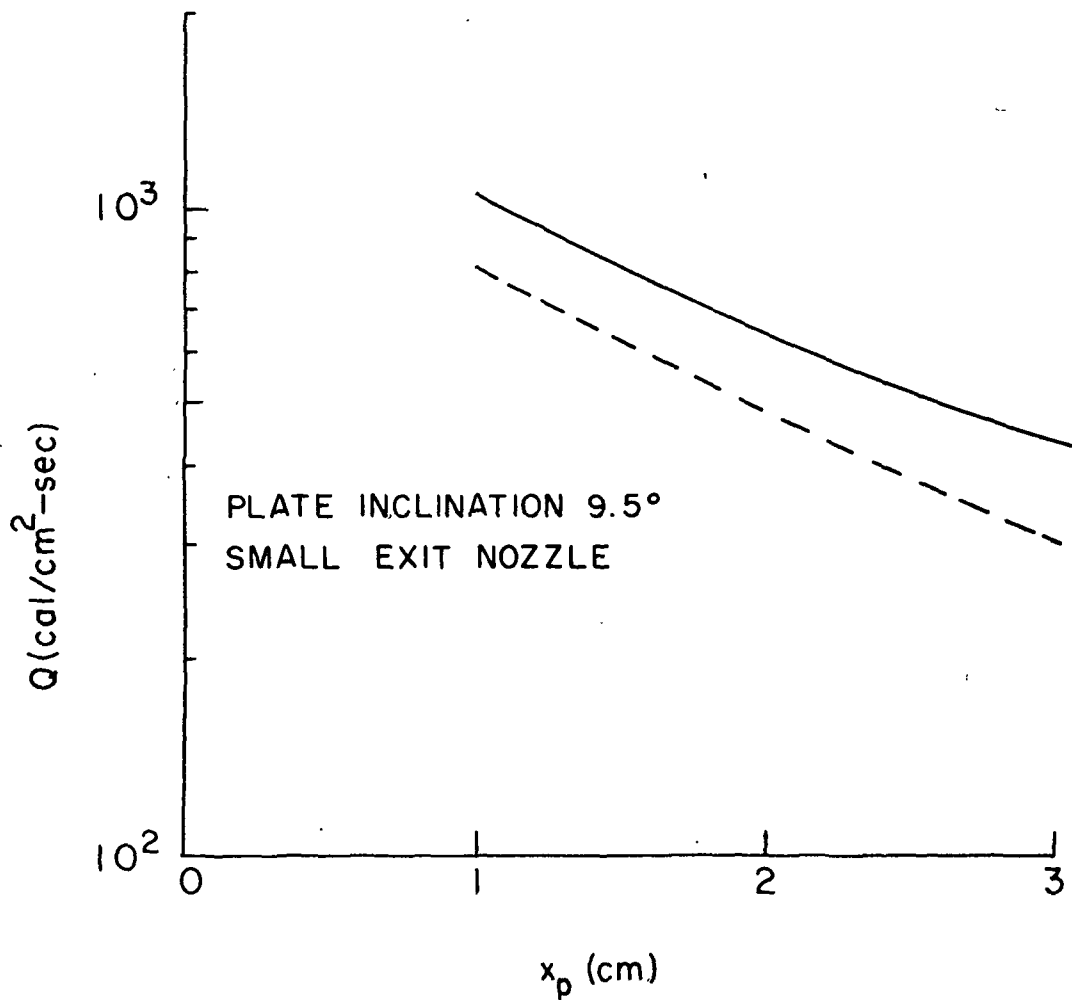


Figure 1.22

Surface heat transfer rate for frozen boundary layer. Transport properties set constant at free stream values. Solid line 100% catalytic surface; dotted line 100% non-catalytic surface

The above arguments also hold if there is some, but not complete, recombination on the surface. In this case, the derivative  $S'$  is not zero, but is nevertheless diminished in value.

### 3. Conclusion

New transport parameters have been defined and these have been fully differentiated to form boundary layer equations that take into complete account the variation of the transport properties throughout the boundary layer.

These relations have been integrated in a fully coupled manner. The importance of using variable transport parameters, in the case of the equilibrium condition, has been demonstrated. Their use results in lower predicted surface heat transfer rates for pure Argon flows.

At the same time, the work has shown that the added computing time for a full variational transport parameter frozen calculation is not warranted, and the setting of the transport properties to their constant free stream values is sufficient. In the case of a frozen boundary layer, the surface heat transfer rate is lowered if there is either no recombination or slow recombination on the surface of the plate.

PART 2

FREE STREAM CONDITIONS AND EFFECTS  
OF HELIUM CONTAMINATION\*

## 1. Introduction

The gas conditions in the test section of a shock tunnel are determined by the reflected shock heated gas acting as a reservoir for the nozzle flow. It is important to have a knowledge of the processes that produce the high enthalpy gas and that occur during the subsequent nozzle expansion. It is also important to have an understanding of the conditions that will alter these processes, and to what extent flow characteristics will be altered.

In this part of the paper theoretical investigations are made of the reflected shock region, of the nozzle flow, and of the changes produced in the gas by passage across the oblique shock front produced by the inclined flat plate in the test section. As discussed in Part 1, previous work suggests that there may be a low level of Helium driver gas contamination early in the flow. Consequently, the above investigations take into account the possible changes produced by the presence of varying amounts of Helium in the test gas. In the case of contamination, possible changes in the boundary layer structure, or surface heat transfer, are also examined.

## 2. Pure Argon

### Development of the Reflected Shock Region

The conditions across the initial shock front, generated at the time of the metal diaphragm rupture, will be governed by the normal shock jump conservation relations, in shock co-ordinates

$$\text{mass: } \rho_1 u_1 = \rho_2 u_2 , \quad (2-1)$$

momentum:  $P_1 + \rho_1 u_1^2 = P_2 + \rho_2 u_2^2$ , (2-2)

energy:  $h_1 + u_1^2/2 = h_2 + u_2^2/2$ , (2-3)

where the subscripts 1 and 2 refer to the regions before and after the shock passage, respectively.

Additionally, there are the thermodynamic equations of specific enthalpy, state, and, if equilibrium is assumed, the Saha equation, i.e.

$$h = \frac{5}{2} (1 + \alpha) RT + \alpha I, \quad (2-4)$$

$$P = (1 + \alpha) \rho RT, \quad (2-5)$$

$$\frac{\alpha^2}{(1 - \alpha)} = \frac{(2m_e k)}{h^2} \frac{kT^{3/2}}{\rho} 2 \frac{Z_1}{Z_o} \exp \left( -\frac{\epsilon}{kT} \right). \quad (2-6)$$

Equations (2-1) through (2-6) have been solved in an iterative manner for the six unknowns of  $\rho_2$ ,  $u_2$ ,  $h_2$ ,  $P_2$ ,  $\alpha$ , and  $T$ . The results obtained, based on an initial shock tube pressure of  $6.77 \times 10^5$  dyne/cm<sup>2</sup> (2" hg) Argon and a measured shock velocity of  $5.52 \times 10^5$  cm/sec, are shown in Table 2.1.

The normal shock will reflect at the nozzle end of the shock tube. In laboratory co-ordinates, the reflected shock front will move back up the tube with a velocity  $W_R$ , and the gas behind the front is brought to rest in the laboratory system.

$u_2$  - 4.74 E+5 cm/sec  
 $P_2$  - 2.84 E+7 dyne/cm<sup>2</sup>  
 $\rho_2$  - 7.74 E-4 gm/cc  
 $h_2$  - 3,600 cal/gm  
 $T_2$  - 15,280 degree-K  
 $\alpha_2$  - 0.156

TABLE 2.1  
CALCULATED FIRST NORMAL SHOCK CONDITIONS

$u_3$  - 1.19 E+5 cm/sec  
 $P_3$  - 2.46 E+8 dyne/cm<sup>2</sup>  
 $\rho_3$  - 3.86 E-3 gm/cc  
 $h_3$  - 7,635 cal/gm  
 $T_3$  - 21,535 degree-K  
 $\alpha_3$  - 0.424  
 $a_3$  - 2.82 E+5 cm/sec

TABLE 2.2  
CALCULATED REFLECTED SHOCK CONDITIONS

$a_*$  - 2.65 E+5 cm/sec  
 $T_*$  - 19,940 degree-K  
 $\rho_*$  - 2.40 E-3 gm/cc  
 $P_*$  - 1.37 E+8 dyne/cm<sup>2</sup>  
 $h_*$  - 6,800 cal/gm  
 $\alpha_*$  - 0.375

TABLE 2.3  
CALCULATED CONDITIONS IN THE THROAT OF THE NOZZLE

A pocket of very high enthalpy gas is formed, and then in turn this gas forms a reservoir for the nozzle. Equations (2-1) through (2-6) can be rearranged using relations (2-7) to the forms

$$\rho_3 = \rho_2(u_3 + v_2)/u_3, \quad (2-1R)$$

$$u_3 = (1/v_2) (P_3/\rho_2) - (P_2/\rho_2) - v_2, \quad (2-2R)$$

$$h_3 = h_2 + v_2(v_2 + 2u_3)/2, \quad (2-3R)$$

$$h_3 = 5/2 (P_3/\rho_3) + \alpha I, \quad (2-4R)$$

with equations (2-5) and (2-6) remaining the same. Iteration over this set of equations, using the results shown in Table 2.1, gave rise to the values shown in Table 2.2.

The values of Table 2.2 may be modified further, depending on how far the shock tube operation is from the "tailored" mode. This is, the pressures on either side of the Argon-Helium contact surface are such that this interface remains stationary. The Australian National University Free Piston Shock Tunnel, "T2," design is such that when an initial shock tube pressure of 2" hg of Argon is used, the measured reflected shock region pressure is within 5% of that shown in Table 2.2, and therefore the shock tube operation was considered, for all practical purposes, tailored.

Without specifying what mechanisms may occur, a parametric investigation was carried out of the effects of enthalpy loss and/or freezing in the reflected shock heated region.<sup>1</sup> The results of these calculations were carried through to the test section in the form of a sensitivity study and will be discussed in more detail below.

---

<sup>1</sup> e. g. There may be loss via radiation or loss via heat conduction to the walls of the shock tube.

The prime assumptions made were that regardless of the loss the pressure of the reflected shock region remained constant, and the gas always returned to a state of thermodynamic equilibrium. That is, any loss of enthalpy was followed by a lowering of the temperature, loss of ionization, and a density change, with the new values satisfying the Saha Equation.

The speed of sound in a gas is given by

$$a^2 = \left( \frac{\partial P}{\partial \rho} \right)_S \quad (2-8)$$

For an ideal gas equation (3-8) becomes

$$a^2 = \gamma (P/\rho) \quad (2-9)$$

By comparison of equation (2-8) and (2-9), one may define an "effective  $\gamma$ " for isentropic conditions, namely

$$\gamma_{\text{eff}} = \frac{dP}{P} \frac{\rho}{d\rho} \quad (2-10)$$

Stalker (1961), using Lighthill's (1957) concept of an "ideal dissociating gas," derived an expression for the effective gamma of a dissociating gas. A similar solution can be obtained in the case of an ionizing gas.

Using equations (2-4) through (2-6) with the standard thermodynamic result obtained by a combination of the First and Second Law of Thermodynamics,

$$T dS = dh - dP/\rho \quad (2-11)$$

it can be shown that the differential change of entropy of a monatomic gas,  $dS$ , is given by

$$dS = \frac{5}{2} R d\alpha + I \frac{d\alpha}{T} - (1 + \alpha) I \frac{dT}{T^2} + 2 R \frac{d\alpha}{\alpha} + 2 R \frac{d\alpha}{(1 - \alpha)} \quad (2-12)$$

Under isentropic conditions  $dS = 0$  and therefore equation (2-12) may be solved for the rate of change of ionization with temperature.

The result is

$$\frac{d\alpha}{dT} = \frac{(1 + \alpha) I}{5/2 R T^2 + I T + 2 R T^2 [\alpha(1 - \alpha)]^{-1}} \quad (2-13)$$

Equation (2-10) may also be rewritten for isentropic conditions in the form

$$\gamma_{\text{eff}} = \frac{dP}{P} \frac{\rho}{d\rho} \quad (2-14)$$

The quantity  $dP/P$  can be obtained from the equation of state, equation (2-5), and a value for  $\rho/d\rho$  can be calculated from Saha's Equation, equation (2-6). The final result is

$$\gamma_{\text{eff}} = \frac{5/2 T + I/(R T^2) - 2 \alpha(1 - \alpha^2)^{-1} \frac{d\alpha}{dT}}{3/2 T + (I/R) T^2 - (2 - \alpha) \alpha(1 - \alpha)^{-1} \frac{d\alpha}{dT}} \quad (2-15)$$

and the speed of sound is then evaluated from the relation

$$a^2 = \gamma_{\text{eff}} \frac{P}{\rho} \quad (2-16)$$

#### Nozzle Conditions

The mass conservation equation, equation (2-1), is modified for the problem of nozzle flow to

$$\rho_1 u_1 A_1 = \rho_2 u_2 A_2 = \rho_* u_* A_* . \quad (2-17)$$

Equation (2-2) does not apply to nozzle flow, but equations (2-3) through (2-6) remain the same, except now the conditions of region 2 refer to those in the throat of the nozzle, while region 1 refers to the reflected shock conditions<sup>1</sup>. Additionally, there are now equations (2-13), (2-15), (2-16), and an integrated form of equation (2-12), i. e.

$$S = \frac{5}{2} R \alpha + 2 R \ln \frac{\alpha}{(1-\alpha)} + \frac{(1+\alpha) I}{T} + S_o \quad (2-18)$$

where the entropy change is referenced to the unspecified value  $S_o$ . All of these equations were solved by iteration for the conditions in the throat of the nozzle. A value of the ionization fraction lower than that in the reflected shock region would be chosen. Using equation (2-16), a corresponding value of the temperature would be found. A calculation of the throat flow velocity could then be made via equations (2-6), (2-4), and (2-3). An independent determination of the velocity was also obtained through equations (2-13), (2-15), and (2-16). These two results were compared and the iteration continued until their difference fell within a specified tolerance. The results obtained, based on the values shown in Table 2.2, are given in Table 2.3.

Logan (1971) has examined the possibility of non-equilibrium nozzle flow in this nozzle at these conditions. His results indicate that equilibrium isentropic flow is a good first approximation in the case of Argon, and this condition has been adopted in this work.

---

<sup>1</sup> Note that in equation (2-3) the energy of the reflected shock region equals the stagnation enthalpy.

Nozzle flow calculations were carried out for two conical configurations, each with the same throat radius of 0.159 cm. The first nozzle had a  $15^{\circ}$  half angle and an on axis length of 20 cm. The second nozzle had a  $7.5^{\circ}$  half angle and an on axis length of 13.4 cm. Figure 2.1 shows the relationship between on axis position and area ratio for the two configurations.

As a first approximation, it has been assumed that the nozzle wall boundary layer is sufficiently thin to not significantly displace the flow.

#### Results and Discussion for Pure Argon

##### Enthalpy Loss in the Reflected Shock Heated Gas

As stated, a sensitivity study was carried out on the effect of enthalpy loss in the reflected shock heated gas, and the results of this work are illustrated in Figure 2.2. The most sensitive parameter to enthalpy loss, under isobaric equilibrium conditions, is the ionization fraction. The density also showed a sensitivity to enthalpy loss with almost a unity ratio between the percentage of enthalpy loss and the percentage of density gain. The temperature and the speed of sound displayed about the same characteristic of a much lesser response to enthalpy losses.

##### Exit Conditions

Mach No.: The maximum stagnation enthalpy was taken at 7,635 cal/gm, as shown in Table 2.2. Nozzle calculations have been carried out for this figure and for possible stagnation enthalpy losses of up to about 25%. Figure 2.3 illustrates the calculated exit Mach No. for the two nozzles as a function of the stagnation enthalpy. The  $15^{\circ}$  half angle

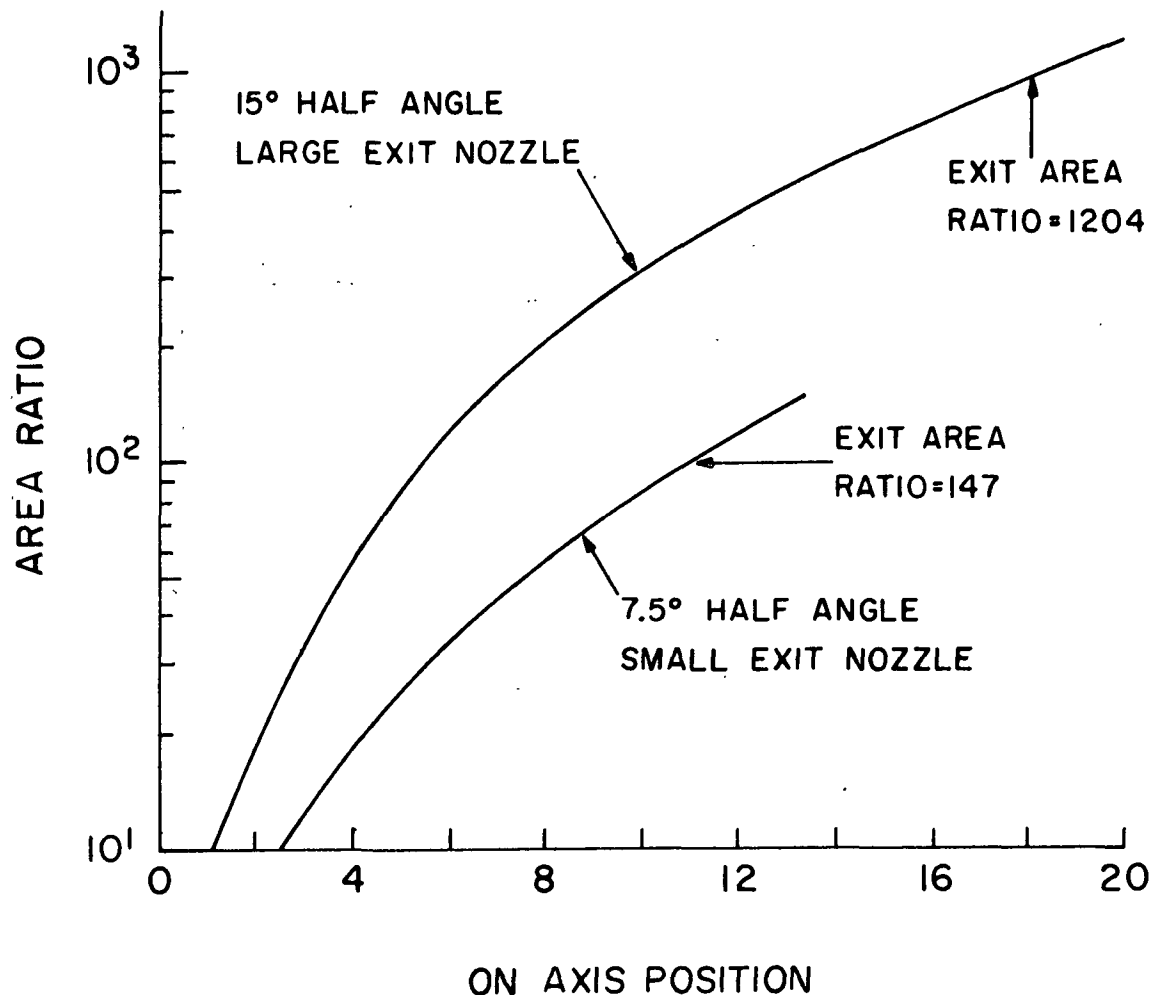


Figure 2.1

Nozzle area ratio as a function of on axis distance from throat

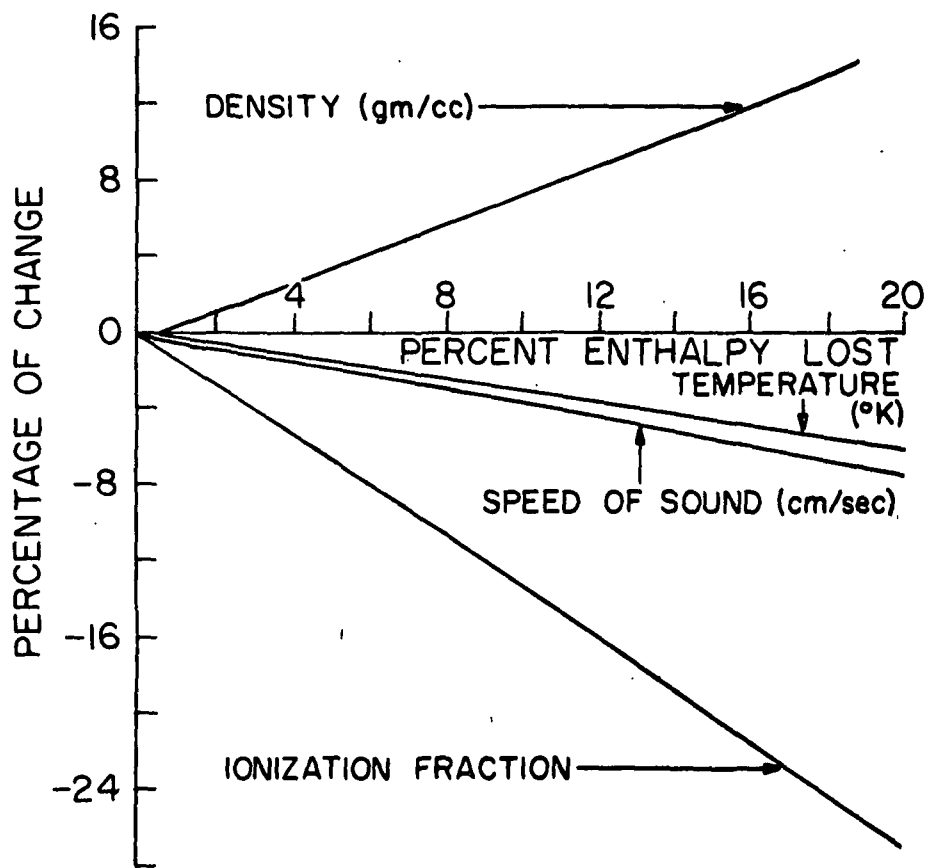


Figure 2.2  
Reflected shock gas changes due to enthalpy loss

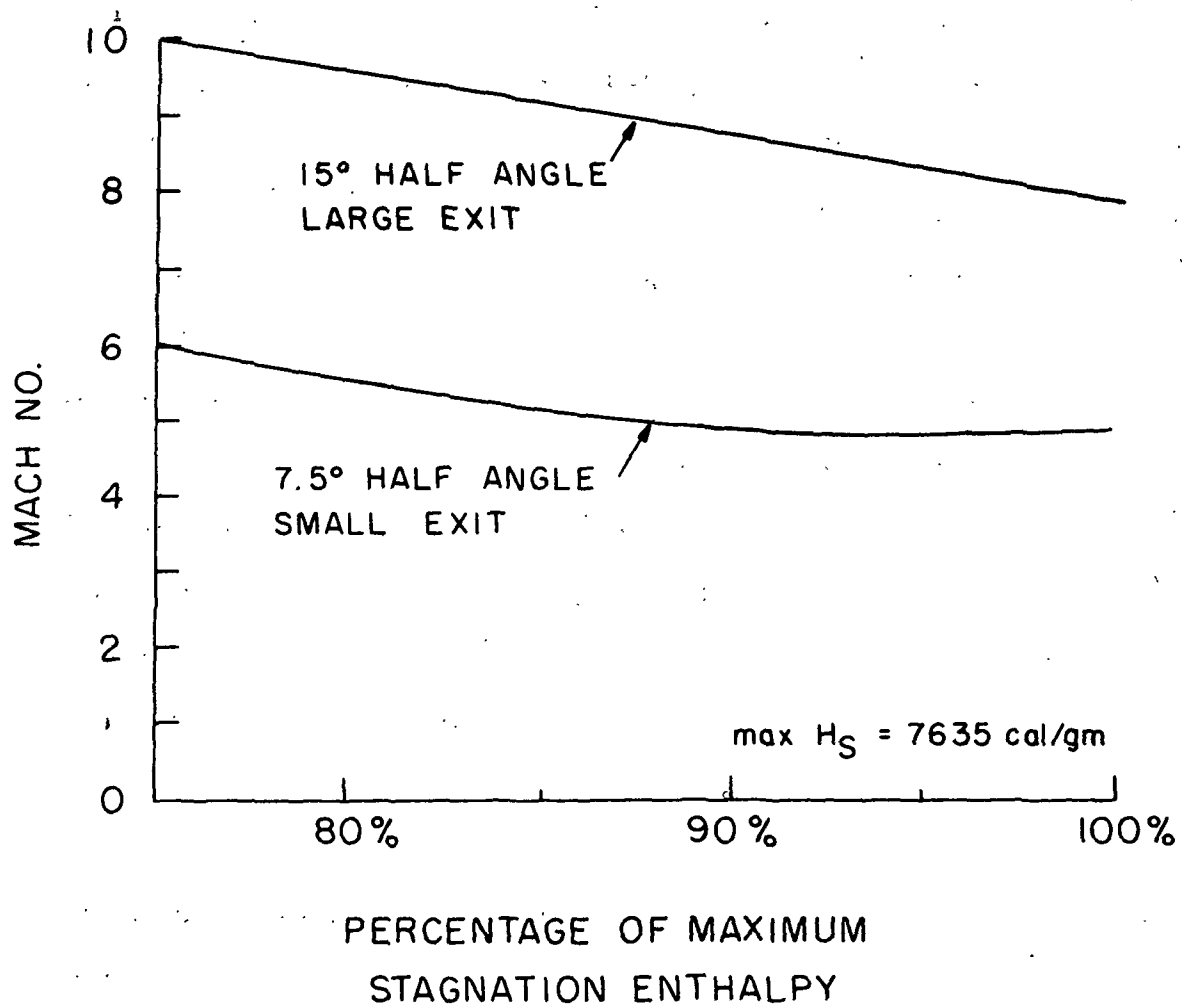


Figure 2.3

Exit Mach No. as function of stagnation enthalpy

nozzle exit Mach No. exhibited a linear behavior and actually increases in value as enthalpy was lost. This interesting feature is explained by the fact that while both the exit gas velocity and speed of sound decrease as enthalpy is lost, the speed of sound decreases at a slightly more rapid rate.

The  $7.5^\circ$  half angle nozzle displayed a non-linear behavior in contrast to the larger exit nozzle. This is probably due to the fact that while the ionization fraction is zero for all practical purposes in regards to the  $15^\circ$  half angle nozzle, this is not the case with the  $7.5^\circ$  half angle unit. For the values of 100%, 94%, 87%, 80%, and 75% of the maximum possible stagnation enthalpy, there were ionization fractions of  $6.7 \times 10^{-3}$ ,  $1.3 \times 10^{-3}$ , and  $4 \times 10^{-5}$ , respectively, for the first three, and the last two had ionization fractions of less than  $10^{-6}$ .

Any ionization fractions as small as  $10^{-3}$  must be called "significant"; for example, the value of the effective gamma is slightly lowered from 1.67 to 1.66 at the ionization level of  $4 \times 10^{-5}$ ; at the level of  $1.3 \times 10^{-3}$  this lowering has increased to the point where the effective gamma is 1.53.

#### Pitot Pressure

Figure 2.4 shows the calculated pitot pressures as a function of the stagnation enthalpy. The most striking feature is the almost complete insensitivity of this parameter to enthalpy loss. The experimental points shown will be discussed in Chapter 4.

### 3. Argon-Helium Mixtures

#### Theory

In this phase of the investigation, it is assumed that the final effects of adding an arbitrary amount of Helium to the pure Argon test

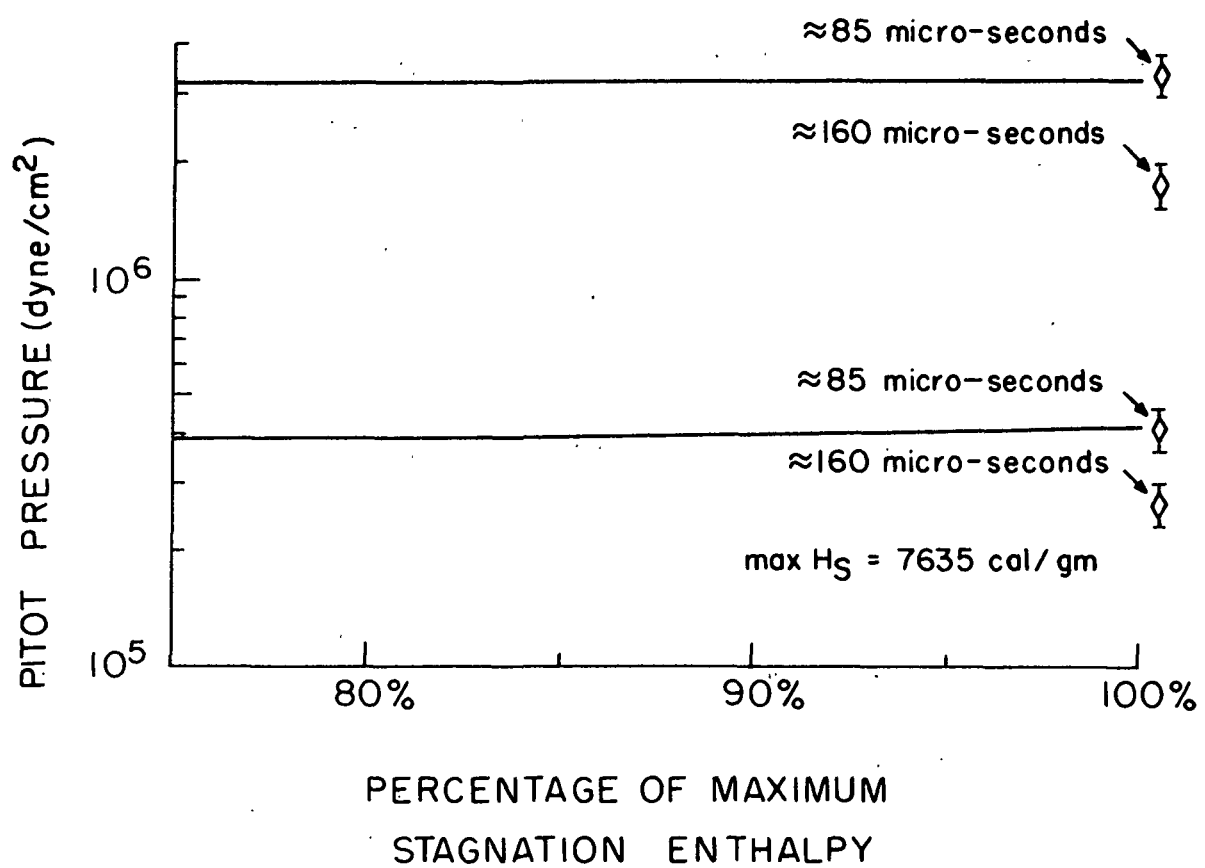


Figure 2.4

Exit Pitot pressure as function of stagnation enthalpy

slug are independent of the manner in which the contamination is added. There is one qualification in that the characteristic time taken for contamination must be short enough so that the properties of the pure Argon alone would not have significantly changed.

Consequently, the following model has been adopted: At some arbitrary time, a specified amount of cold Helium is added to the known amount of pure Argon at reflected shock conditions, in the volume defined by the reflected shock region. The gases interact. The temperature of the reflected shock region is the order of  $20,000^{\circ}\text{K}$  at high pressures and therefore as a first approximation it is justified to assume that no ionization of the Helium takes place. Hence, the mixture affects the rate of ionization of the Argon by absorbing some of the enthalpy of the system but not by direct chemical reaction such as increasing the three body recombination rate.

The total enthalpy of a mixture of gases is given by

$$h = \sum_i x_i h_i , \quad (2-19)$$

where  $x_i$  is the mass fraction of component i. Specifically, in the case at hand

$$h = x_A h_A + x_H h_H , \quad (2-20)$$

or

$$h = x_A \frac{5}{2} (1 + \alpha) R_A T + \alpha I + \frac{5}{2} x_H R_H T . \quad (2-21)$$

Since no further mass is added or taken from the system, (the later nozzle flow will be considered as an expansion of the system and not a loss of mass) the mass fractions are taken to remain constant. In this context, the mass fraction of the Argon includes the mass of Argon ions.

The total pressure of ionized Argon and neutral Helium mixture has four components,

$$P = P_H + P_{AN} + P_{AI} + P_e , \quad (2-22)$$

where the subscripts AN, AI, and e refer to the neutral Argon atoms, the first ionized Argon ions, and the electrons resulting from the Argon ionization. The density ratio between the Argon total density (atoms and ions) and the Helium density can be obtained through the respective equations of state,

$$\frac{\rho_A}{\rho_H} = \frac{P_A}{1 + \alpha} \frac{1}{P_H} \frac{R_H}{R_A} , \quad (2-23)$$

Equations (2-22) may be written as

$$P = \frac{R_o T}{V} (n_{AN} + n_{AI} + n_e + n_H) , \quad (2-24)$$

where the n terms are the numbers of moles of each component in the total volume V.  $R_o$  is the universal gas constant. The definition of the ionization fraction,  $\alpha$ , is given by

$$\alpha = \frac{n_{AI}}{n_{AN} + n_{AI}} \quad (2-25)$$

and from charge neutrality,  $n_{AI} = n_e$ . The first three terms in the bracket of equation (2-24) can be factored. Then,

$$P = \frac{R_o T}{V} (n_{AN} + n_{AI}) (1 + \alpha) + n_H . \quad (2-26)$$

The Argon partial pressure is given by the Argon mole fraction and the total pressure,

$$P = \frac{(n_{AN} + n_{AI})(1 + \alpha)}{(n_{AN} + n_{AI})(1 + \alpha) + n_H} P . \quad (2-27)$$

Similarly, the Helium partial pressure is given by

$$P_H = \frac{n_H}{(n_{AN} + n_{AI})(1 + \alpha) + n_H} P , \quad (2-28)$$

and using these two relations, equation (2-23) becomes,

$$\frac{\rho_A}{\rho_H} = \frac{(n_{AN} + n_{AI})}{n_H} \frac{R_H}{R_A} . \quad (2-29)$$

The right hand side of equation (2-29) is constant in value, so the Helium density may be defined by

$$\rho_H = F \rho_A , \quad (2-30)$$

where  $F$  is some arbitrary constant of value less than one.

This same result is obtained for the case of no Argon ionization. Thus, in all cases there will be differential changes of pressure between the two gases, but the density will change in a like manner for both gases.

The entropy of a gas mixture is given by the general relation

$$S = \sum_i x_i S_i \quad (2-31)$$

or specifically in the case at hand by

$$S = x_A \left( \frac{5}{2} R_A \alpha + \frac{I}{T} + \frac{(1 + \alpha) I}{T} \right) + 2 R_A \ln \frac{\alpha}{1 + \alpha} + S_o + x_H R_H \left( \frac{3}{2} \ln \frac{T}{T_o} - \ln \frac{\rho_H}{\rho_{Ho}} \right) , \quad (2-32)$$

where  $S_o$ ,  $T_o$ , and  $\rho_{Ho}$  are all referenced to some arbitrary datum level. In this study, to avoid any complications from entropy changes resulting from diffusion of one gas into the other, this reference level has been set at the final reflected shock conditions of the completely mixed system after any possible isentropic expansions.

By differentiating equation (2-32), considering the mixture to behave in an isentropic manner, and differentiating equation (2-29), a value of the rate of ionization change with temperature can be determined,

$$\frac{d\alpha}{dT} = \frac{(1 + \alpha) + \frac{x_H}{x_A} \frac{R_H}{R_A} I}{\frac{5}{2} R_A T^2 + I T + \frac{2 R_A T^2}{\alpha(1 - \alpha)} + \frac{x_H}{x_A} \frac{(2 - \alpha)}{\alpha(1 - \alpha)} R_H T^2} . \quad (2-33)$$

The effective value of gamma as defined in equation (2-10) can also be determined for the mixture. In this event

$$\frac{dP}{P} = \frac{dP_A}{P} + \frac{dP_H}{P} , \quad (2-34a)$$

and

$$\frac{dp}{\rho} = \frac{dp_A}{\rho_A} , \quad (2-34b)$$

and therefore

$$\gamma_{\text{eff}} = \frac{\frac{5}{2} T + \frac{I}{R_A T^2} - \frac{P_A}{P} \frac{2}{\alpha(1 - \alpha)^2} + \frac{P_H}{P} \frac{(2 - \alpha)}{\alpha(1 - \alpha)} \frac{d\alpha}{dT}}{\frac{3}{2 T} + \frac{I}{R_A T^2} - \frac{(2 - \alpha)}{\alpha(1 - \alpha)} \frac{d\alpha}{dT}} . \quad (2-35)$$

where the term  $\frac{d\alpha}{dT}$  is defined by equation (2-33).

If  $P_H/P$  is set equal to zero and  $P_A/P$  set equal to one, equation (2-35) simply becomes equation (2-15). However, it should be noted that for a non-zero Helium pressure component, both of these equations tend to a value of  $5/3$  as the ionization fraction goes to zero.

The final values of  $T$ ,  $\alpha$ , and  $P$  of the various mixture ratios can be solved by using equations (2-21), (2-6), (2-30), and the equations of state for the pure gases. The nozzle flow conditions can be determined with the added use of equation (2-35).

#### Argon-Helium Mixtures Calculations

##### Reflected Shock Region

Table 2.4 illustrates the effects of Helium contamination in specified amounts on the original pure Argon reflected shock conditions.

The addition of Helium cooled the test gas with a corresponding drop in temperature and ionization. There was a rise in the density and pressure, but the enthalpy was assumed to remain unchanged. Fast response stagnation pressure readings of the reflected shock region taken by Stalker (1967) show no significant changes during the first few hundreds of micro-seconds after shock reflection, other than from a pressure "dip" at about 20 micro-seconds. Accordingly, if Helium is added to the test slug, a corresponding expansion of the mixture must occur to maintain a constant pressure. It has been assumed that this expansion is isentropic, and the reflected shock conditions following such a process are shown in Table 2.5.

The gas mixture must do work on its surroundings to expand, therefore the enthalpy of the gas mixture drops, as shown in Table 3.5. The expansion reverses the trend of the density, and rather than increasing as contamination level is increased, it drops. The temperature and

% Mass He	Pressure (dyne/cm <sup>2</sup> )	Density (gm/cc)	Temperature (°K)	Ionization Fraction	Sonic Velocity (cm/sec)
0	2.46 E+8	3.86 E-3	21,537	0.42	2.82 E+5
0.99	2.59 E+8	3.90 E-3	21,351	0.41	2.88 E+5
4.76	3.08 E+8	4.05 E-3	20,641	0.36	3.09 E+5
8.26	3.55 E+8	4.21 E-3	19,974	0.31	3.27 E+5

$H_s = 7,635$  (cal/grm)  
stagnation enthalpy

TABLE 2.4

Calculated Effects of Helium Contamination Upon Original Argon	Reflected Gas System
--	----------------------

% Mass He	Pressure (dyne/cm <sup>2</sup> )	Density (gm/cc)	Temperature ( <sup>o</sup> K)	Ionization Fraction	Specific Enthalpy (cal/gm)	Sonic Velocity (cm/sec)
0	2.46 E+8	3.86 E-3	21,537	0.42	7,635	2.82 E+5
0.99	2.41 E+8 @	3.67 E-3	21,138	0.04	7,522	2.86 E+5
4.76	2.41 E+8	3.43 E-3	20,022	0.34	7,268	3.02 E+5
8.26	2.41 E+8	3.07 E-3	18,776	0.27	6,876	3.13 E+5

@ Value measured by Stalker (1967)

TABLE 2.5

Calculated Final Conditions with Helium After Isentropic Expansion  
in the Reflected Shock Region

% Mass He	Pressure (dyne/cm <sup>2</sup> )	Density (gm/cc)	Temperature (°K)	Ionization Fraction	Specific Enthalpy (cal/gm)	Sonic Velocity (cm/sec)
0	1.37 E+8	2.40 E-3	19,940	0.375	6,800	2.65 E+5
0.99	1.34 E+8	2.28 E-3	19,548	0.35	6,600	2.69 E+5
4.76	1.39 E+8	2.14 E-3	18,413	0.28	6,305	2.84 E+5
8.26	1.32 E+8	1.91 E-3	17,137	0.21	5,844	2.94 E+5

TABLE 2.6

Calculated Throat Conditions with Helium Contamination

ionization fraction are further lowered. The speed of sound, while still increasing as more Helium is added, does so at a lesser rate after expansion.

Using the conditions of Table 2.5 as the final reservoir values, the gas mixtures were further expanded to obtain the gas conditions in the throat of the nozzle. These results are shown in Table 2.6.

The specific enthalpy drop is accounted for by the kinetic motion which the gas has obtained. This velocity amounts to, in enthalpy units, about 1000 cal/gm. The throat pressure changes very little as Helium is added, while the density, temperature and ionization fraction drop.

#### Nozzle Flow

The pressure of the Helium contamination modifies the real gas thermodynamics during the expansion of the test gas down the nozzle. Calculations for both nozzle configurations were carried out. The only parameter that is different between the two units, as far as the solution is concerned, is the area ratio, and therefore the physics is fully demonstrated by the results for the 7.5° half angle nozzle alone.

#### Temperature

Figure 2.5 shows how the calculated temperature varies down the small exit nozzle for different levels of contamination. Additionally, a curve for a pure Helium flow is included, but note should be taken of the different stagnation enthalpy for this case, 11,670 cal/gm, as compared to a maximum of 7,635 cal/gm for the Argon system. This former value is obtained if the shock tube is filled initially with 20" hg of Helium<sup>1</sup>, and is included only for a relative comparison with the other results.

<sup>1</sup> This condition is dynamically equivalent to filling the shock tube with 2" Hg of Argon, if the Argon acted as a "perfect gas."

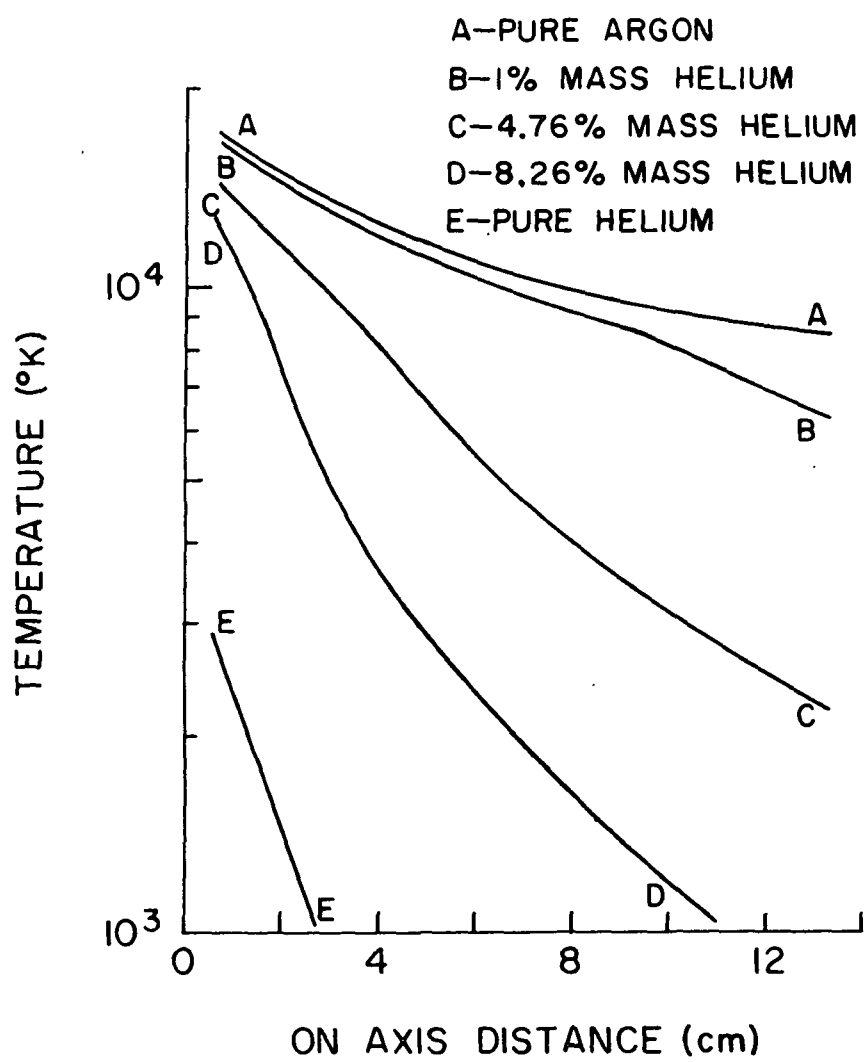


Figure 2.5

Gas temperature down small exit nozzle  
as function of Helium contamination

The most interesting result is the change of slope or general curve character from that of a pure Argon flow as Helium is added. Curve "B", 1% mass Helium, shows an "Argon character" until a distance down the nozzle of approximately 10 cm (area ratio of about 86), and then there is a change of slope. This changeover point moves progressively up the nozzle towards the throat as more Helium is added to the system.

#### Velocity, Density, Pitot Pressure and Static Pressure

No curves are shown for these parameters. The first three quantities proved to be very insensitive to contamination. For example, in the case of a Helium content of 4.76% by mass, the exit velocity was affected by an amount less than 5% of the pure Argon value. Similar results were also true for the density and Pitot pressure calculations.

The static pressure in the nozzle and at its exit dropped by relatively large amounts, as high as an order of magnitude when approximately 10% by mass of Helium was present in the mixture. This pressure drop compensated the fall in temperature so the density remained fairly constant in value.

#### Reynold's Number

The predicted Reynold's Number, as given by  $\rho ux/\mu$ , is of quite different character as the contamination level is increased. In Figure 2.6 it can be seen that with only 1% mass Helium, curve "B", the slope shows a change at a position of about 10 cm. It may be noted that this is about the same point at which the corresponding temperature curve showed modification.

As the level of Helium is raised, the changes become more pronounced and the slope changes from negative to positive.

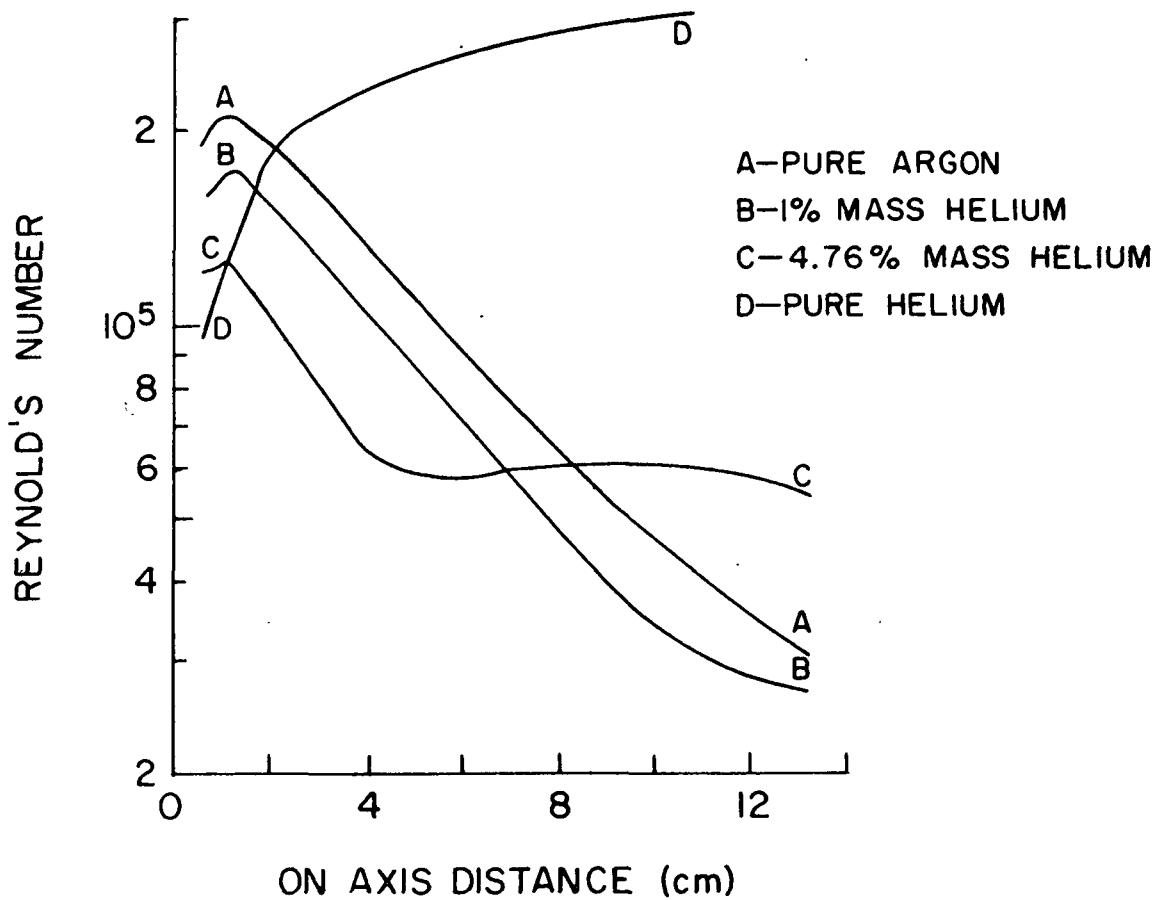


Figure 2.6

Reynold's number down small exit nozzle  
as function of Helium contamination

#### 4. Test Section Conditions

##### Nozzle Exit Values

The gas conditions at the nozzle exit for the various cases considered are summarized in Table 2.7. The stagnation enthalpies have already been presented in Table 2.5. It should be noted that as the Helium level goes beyond about 1% by mass, the Mach Number increases. At a concentration of 8.26% by mass, the exit Mach Number of the  $7.5^{\circ}$  half angle nozzle is within about 30% of the value obtained with the pure Helium flow shown.

##### Flow Divergence

A conical nozzle configuration has been used throughout this investigation. The emerging flow can, therefore, be considered a source-type (that is, as if the flow were produced at a point source in the nozzle throat), if the nozzle wall boundary layer is thin as assumed. Consequently, the velocity vector of the gas will diverge as one proceeds from the on axis position toward the nozzle wall.

This divergence means that the density and pressure of the flow continually decrease after the gas leaves the nozzle. Since these parameters are important in the boundary layer calculations, it is necessary to estimate the effects of flow divergence upon the gas conditions.

Hall (1963) has investigated divergence effects in flow over hypersonic test bodies. Hall's analysis included centrifugal effects. For flat plate flow, these are not present since the stream lines after the oblique shock are assumed to remain parallel to the surface. The original problem, as defined by Hall for two dimensional flow over a sharp wedge, is solved here in a simple geometrical manner. The problem is illustrated in Figure 2.7.

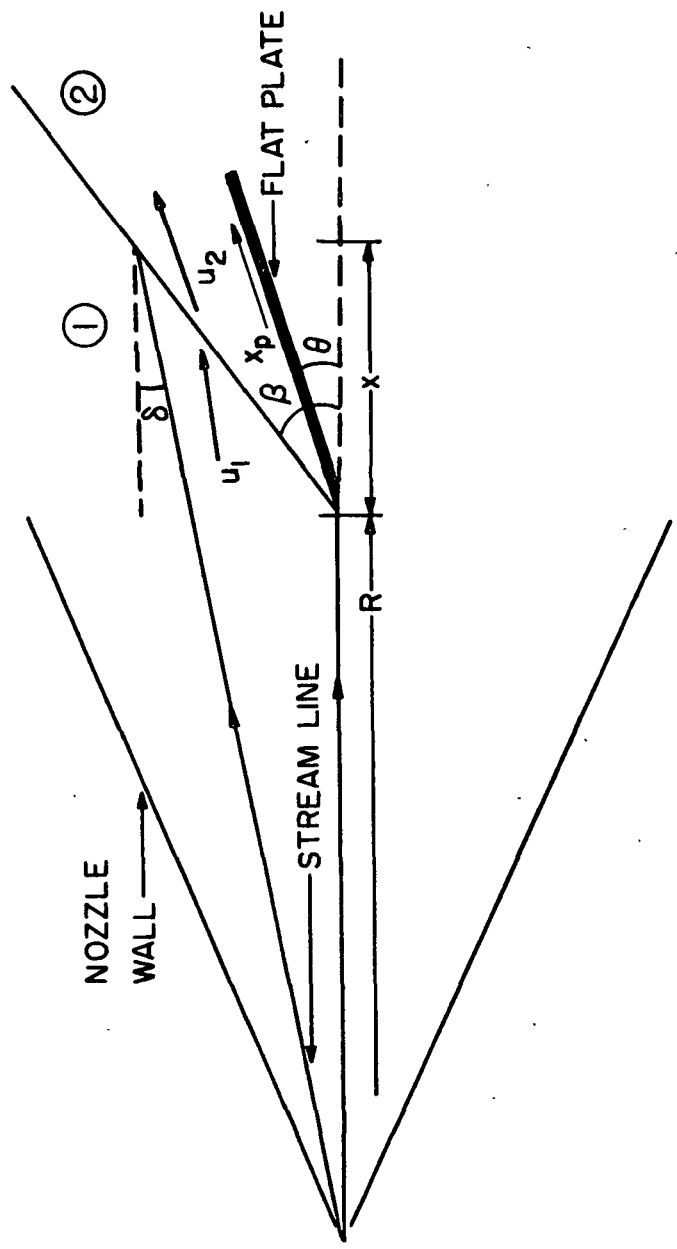


Figure 2.7

Two dimensional diverging flow over sharp leading edge inclined flat plate  
( after wedge problem of Hall ( 1963 ) )

Nozzle angle	% Mass He	Pressure (dyne/cm <sup>2</sup> )	Density (gm/cc)	Temperature (degree-K)	Ionization Fraction	Velocity (cm/sec)	Mach No.
15° half angle	0.0	3.97 E+3	6.76 E-7	2816.0	0.0	7.18 E+5	7.90
	100.0	1.36 E+2	1.35 E-7	48.0	0.0	1.09 E+6	26.75
	(10 <sup>11</sup> Hg)						
7.5° half angle	0.0	1.02 E+5	5.86 E-6	8335.0	8.41 E-3	7.38 E+5	4.87
	0.99	8.08 E+4	5.58 E-6	6381.0	2.47 E-4	7.46 E+5	4.86
	4.76	3.60 E+4	5.45 E-6	2221.0	0.0	7.59 E+5	7.24
	8.26	1.69 E+4	5.44 E-6	857.0	0.0	7.91 E+5	11.0
	100.0	7.25 E+3	2.19 E-6	159.0	0.0	9.77 E+5	13.15
	(20 <sup>11</sup> Hg)						

TABLE 2.7

Nozzle Exit Conditions

The relationship between the ambient density, velocity, and pressure changes in high Mach Number diverging flow was given by Hall as

$$\frac{dp}{\rho} \approx \frac{2x}{R} , \quad (2-36)$$

and

$$\frac{dP}{P} \approx \frac{2\gamma x}{R} . \quad (2-37)$$

#### Conditions Across the Oblique Shock Front

To simplify the analysis, the shock front is considered to remain straight. Therefore, the complications brought about by divergence of the flow are (1) the ambient pressure (or density) has been lowered and (2) the stream line is not parallel to the axis of the nozzle. The first problem is handled by using equations (2-36) and (2-37) to correct the nozzle exit values. For the second item, the mass conservation equation (2-1) is taken as valid, and examination of the velocity vector components after the oblique shock (they will add a form a flow parallel to the surface of the plate) will show that from the geometry

$$\frac{u_{2n}}{u_{1n}} = \frac{\rho_1}{\rho_2} = \frac{\tan(\beta-\theta)}{\tan(\beta-\delta)} , \quad (2-38)$$

where  $n$  denotes normal to the shock front,  $\delta$  is the flow divergence angle and its value is obtained from the relation

$$\delta \approx \frac{x_p \cos \theta \tan \beta}{R + x_p \cos \theta} \quad (2-39)$$

where  $\delta$  is in radians. The term  $x_p$  is the point where the stream line contacts the shock front, given in terms of distance parallel to the surface of the flat plate measured from the leading edge.

The work of Petschek and Byron (1957); Wong and Bershader (1966); and Oettinger and Bershader (1967), has indicated that the position of the shock front (the angle  $\beta$ ) is determined by ideal gas or frozen conditions. This is because the finite relaxation time of the gas flow is enough to prevent immediate production of ionization after passage of the shock layer.

The shock angle and inclination angle have been taken to be related by the standard result

$$\frac{\tan(\beta - \theta)}{\tan \beta} = \frac{(\gamma_N - 1) M_N^2 \sin^2 \beta + 2}{(\gamma_N + 1) M_N^2 \sin^2 \beta} \quad (2-40)$$

where  $M_N$  and  $\gamma_N$  are the free stream nozzle exit Mach Number and effective  $\gamma$ .

Equations (2-36), (2-37), (2-38) and (2-39) were used to calculate the frozen after shock conditions for various  $x_p$  distances.

The results of the above calculations are shown in Tables 2.8a and 2.8b. Table 2.8a is for a pure Argon flow and Table 2.8b is for an Argon-Helium flow. As can be seen, the flow divergence can produce lowering of the pressure and density in excess of 100% of the non-divergent values.

Suggested modification of the shock angle with the addition of Helium to the flow is quite interesting. A maximum value, as shown in Table 2.8b, was obtained with a contamination level of about 1%. This is due to the fact that with this amount the calculated exit Mach Number is approximately unchanged from the pure flow value, but the calculated effective value of the quantity  $\gamma$  is higher. At greater levels of contamination, the exit Mach Number, as calculated, increased with corresponding lowering of the shock angle.

$\theta$	$\beta$	$x_p$ (cm)	Pressure (dyne/cm <sup>2</sup> )	Density (gm/cm <sup>3</sup> )	Temperature (°K)	$u_2$ (cm/sec)	$M_2$
15° half angle	9.5	16.2	0.0	2.31 E+4	1.67 E-6	6,634.0	7,55 E+5
		1.0	1.85 E+4	1.44 E-6	6,181.0	7.58 E+5	5.18
		2.0	1.46 E+4	1.22 E-6	5,731.0	7.61 E+5	5.39
		3.0	1.13 E+4	1.03 E-6	5,270.0	7.63 E+5	5.64
	19.5	28.2	0.0	7.16 E+4	2.25 E-6	15,316.0	6.93 E+5
7.5° half angle		1.0	5.81 E+4	1.93 E-6	14,469.0	7.02 E+5	3.00
		2.0	4.68 E+4	1.65 E-6	13,637.0	7.10 E+5	3.13
		3.0	3.73 E+4	1.40 E-6	12,815.0	7.17 E+5	3.26
		18.9	0.0	2.76 E+5	1.21 E-5	10,942.0	7.08 E+5
		1.0	2.02 E+5	9.61 E-6	10,124.0	7.14 E+5	3.81
19.5		2.0	1.44 E+5	7.46 E-6	9,274.0	7.18 E+5	-
		3.0	9.64 E+4	5.59 E-6	8,280.0	7.22 E+5	4.00
		28.7	0.0	6.21 E+5	1.98 E-5	15,060.0	6.56 E+5
		1.0	4.63 E+5	1.58 E-5	14,086.0	6.69 E+5	3.03
		2.0	3.37 E+5	1.24 E-5	13,109.0	6.79 E+5	3.18
		3.0	2.37 E+5	9.43 E-6	12,084.0	6.87 E+5	3.36

TABLE 2.8a

Calculated Conditions After the Oblique Shock in the Test Section for Pure  
Argon (Ideal Gas Shock Angle Determination), No Enthalpy Loss

$\%$ He	$\theta$	$\beta$	$x_p$ (cm)	Pressure (dyne/cm <sup>2</sup> )	Density (gm/cm <sup>3</sup> )	Temperature (°K)	$u_2$ (cm/sec)	$M_2$
7.5°	half angle	0.99	9.5	20.1	0.0	2.19 E+5	9.36 E-6	10, 325.0
		1.0		1.55 E+5	7.43 E-6	9, 193.0	7.24 E+5	3.88
		2.0		1.04 E+5	5.77 E-6	7, 984.0	7.29 E+5	4.20
		3.0		6.43 E+4	4.34 E-6	6, 544.0	7.33 E+5	4.66
		19.5	32.0	0.0	5.52 E+5	1.35 E-5	18, 008.0	6.52 E+5
	angle (10" Hg He)	1.0		4.02 E+5	1.08 E-5	16, 491.0	6.69 E+5	2.68
		2.0		2.86 E+5	8.44 E-6	14, 935.0	6.82 E+5	2.87
		3.0		1.95 E+5	6.48 E-6	13, 281.0	6.93 E+5	3.09
		4.76	9.5	16.8	0.0	1.87 E+5	1.29 E-5	4, 872.0
		1.0		1.33 E+5	1.02 E-5	4, 369.0	7.37 E+5	5.01
4.76	angle (10" Hg He)	2.0		9.08 E+4	7.93 E-6	3, 853.0	7.41 E+5	5.36
		3.0		5.76 E+4	5.93 E-6	3, 267.0	7.44 E+5	5.35
		19.5	29.4	0.0	5.59 E+5	1.76 E-5	10, 698.0	6.71 E+5
		1.0		4.08 E+5	1.40 E-5	9, 813.0	6.85 E+5	3.11
		2.0		2.91 E+5	1.10 E-5	8, 940.0	6.96 E+5	3.31
	angle (10" Hg He)	3.0		2.01 E+5	8.38 E-6	8, 054.0	7.05 E+5	3.53
		15°	100.0	9.5	13.1	0.0	6.20 E+5	4.98 E-7
		half		1.0		4.99 E+5	4.27 E-7	562.0
		2.0		3.98 E+5		3.63 E-7	527.0	1.07 E+6
		3.0		3.13 E+5		3.05 E-7	495.0	1.07 E+6

TABLE 2.8b

Calculated Conditions After the Oblique Shock in Test Section for Ar-He Mixtures  
(Ideal Gas Shock Angle Determination), No Enthalpy Loss

## 5. Contamination Effects on Boundary Layer Calculations

The effects of Helium contamination on the boundary layer calculations will manifest themselves in changes to the thermodynamics (e.g. equation of state, determination of specific enthalpy, and specific heat) and to the transport properties. The new thermodynamic relation has been discussed previously, and the new transport property equations are discussed by Yanow (1971).

### Nozzle Calculations

Initially, interest was focused on what effects, if any, the nozzle throat and nozzle wall boundary layers might have on the free stream flow. These problem areas are far more complicated than the equations of Part 1 were designed to handle, but work was carried out to get a relative comparison between pure Argon, Argon-Helium, and pure Helium produced boundary layers.

To enable any use of the flat plate equations, it was necessary to assume that the radius of curvature of the nozzle region was large in comparison to the boundary layer thickness, and then limit the integration to a very localized section - so localized that the pressure could be taken to remain constant over it. Calculations were carried out for the small exit nozzle configuration with use of the sonic conditions in the throat, the conditions 2.24 cm. down stream, and 12.88 cm. down stream. The pure Argon flow was based on an initial shock tube pressure of two inches Hg; the Argon-Helium mixture assumed 4.76% mass Helium; and the pure Helium flow was based on an initial shock tube pressure of 20 inches Hg.

The integrations in the case of the first two Argon flows used a variable transport parameter technique, while the pure Helium flow assumed

constant parameters. The results of the displacement thickness are shown in Table 2.9. The displacement thickness parameter is given in terms of  $\delta^*/R_x^*$ , where  $R_x$  is the radius of curvature at the distance  $x$  down the nozzle from the throat.

As can be seen in Table 2.9, pure Argon displacement thickness is thin at all times.

Helium in the flow causes the displacement thickness to increase. The value is still very small, however, and not significant in relation to changing the effective area ratio.

Consequently, it would appear that some major change in boundary layer displacement of the flow when Helium is homogeneously mixed into the test gas does not occur.

#### Flat Plate Calculations

##### Equilibrium Boundary Layer

Figures 2.8, 2.9, and 2.10 show the changes that occur to the temperature, ionization fraction, and density respectively, while Figure 2.11 allows conversion from the  $\eta$  axis to the  $y$  axis. All the information shown in these curves is for the small exit,  $9.5^\circ$  plate inclination, two cm. up the plate, and with variable transport parameters.

The Helium will cause the temperature to drop throughout the boundary layer. The density is interesting, in that with 1% mass Helium the value is lowered throughout the boundary layer, but with the larger 4.76% mass contamination the density regains some of its lost value. In the latter case, the minimum density peak is also flattened. The lowering of the specific enthalpy of the Argon is best illustrated by the major changes in the ionization fraction. The peak ionization with

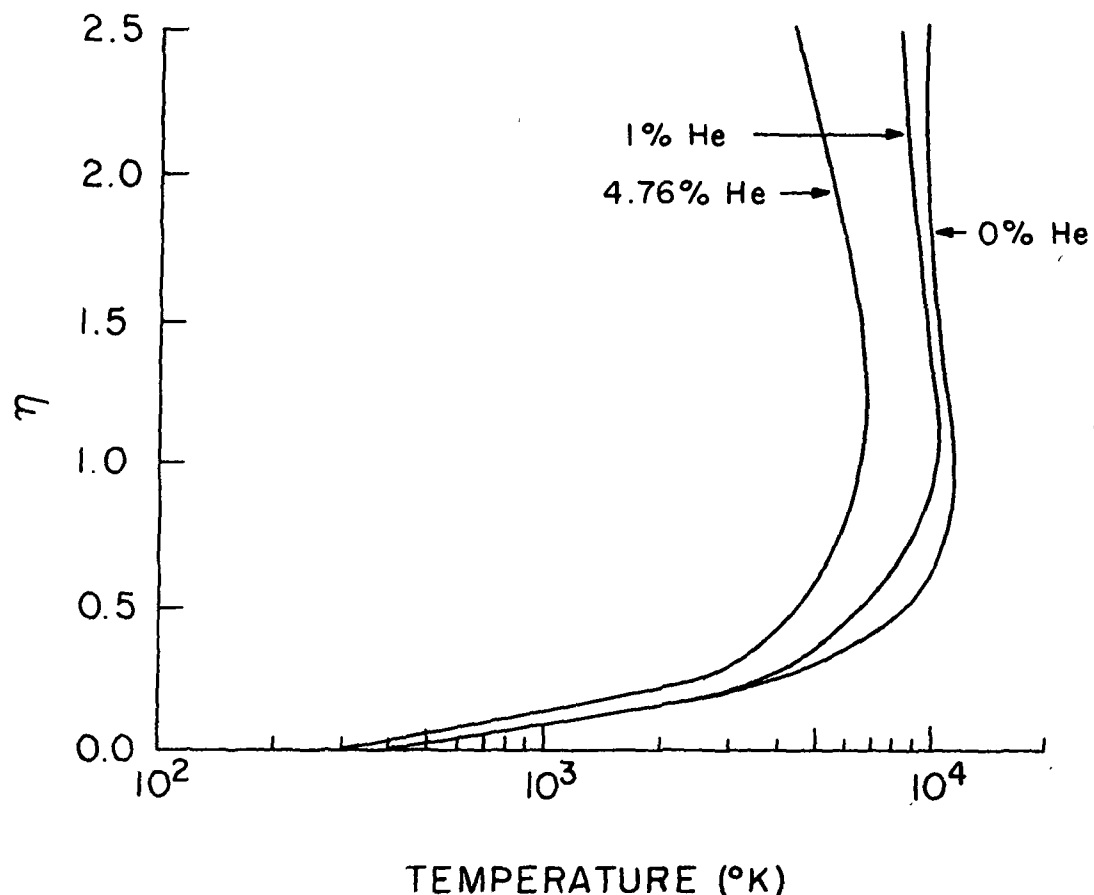


Figure 2.8

Temperature profile for variable transport parameter calculation, small exit nozzle with contamination at  $x_p = 2.0$  cm

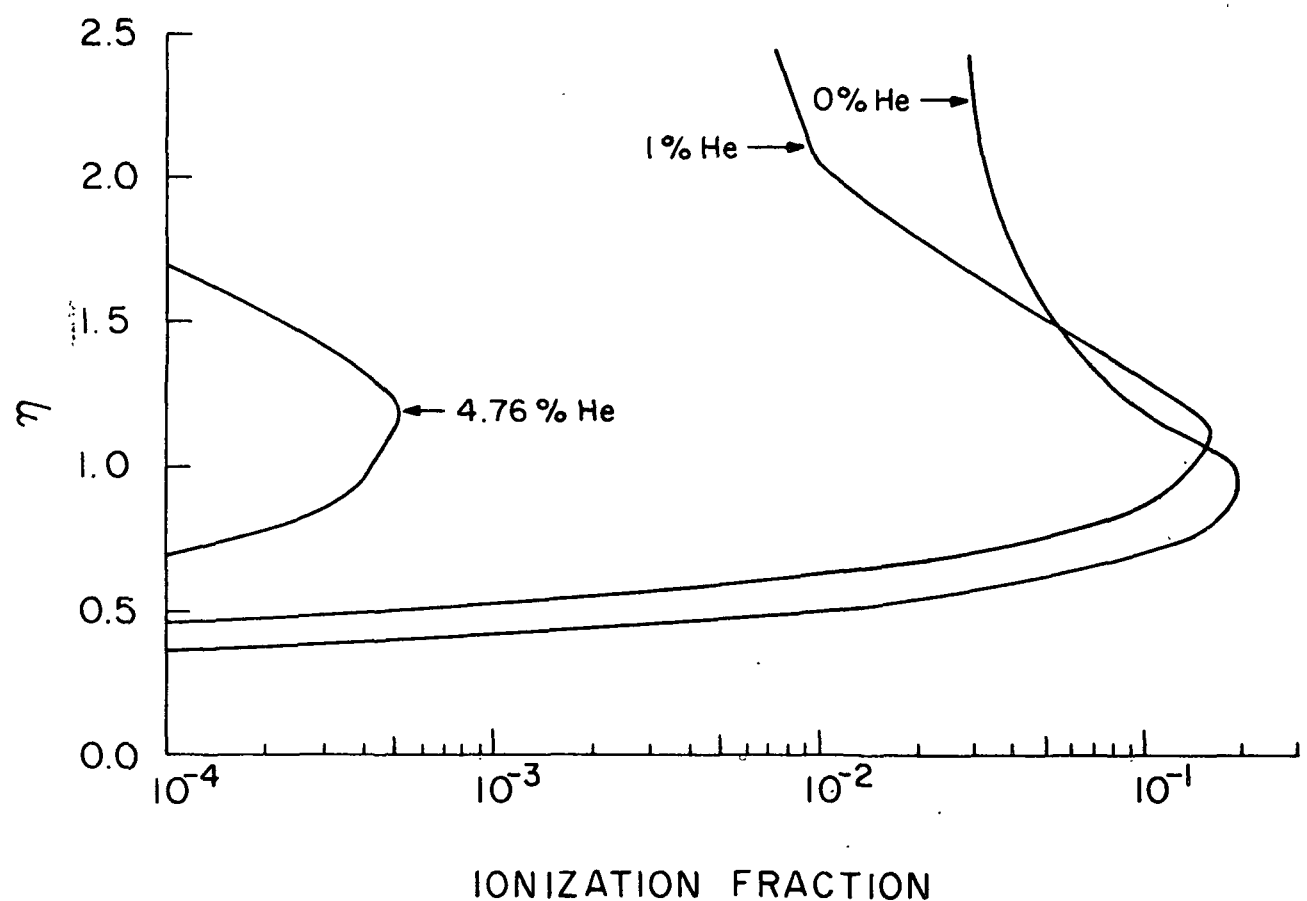


Figure 2.9

Ionization profile for variable transport parameter calculation,  
small exit nozzle with contamination at  $x_p = 2.0$  cm

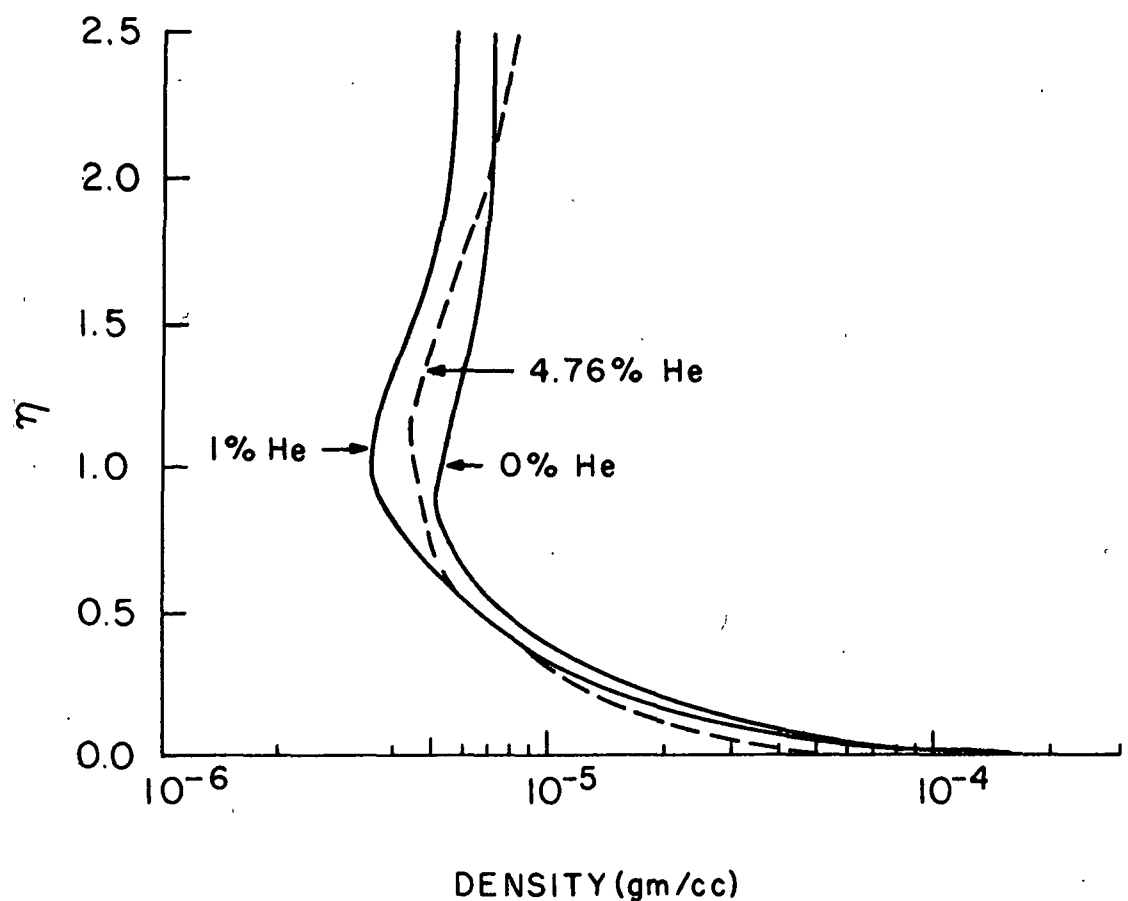


Figure 2.10

Density profile for variable transport parameter calculation,  
small exit nozzle with contamination at  $x_p = 2.0$  cm

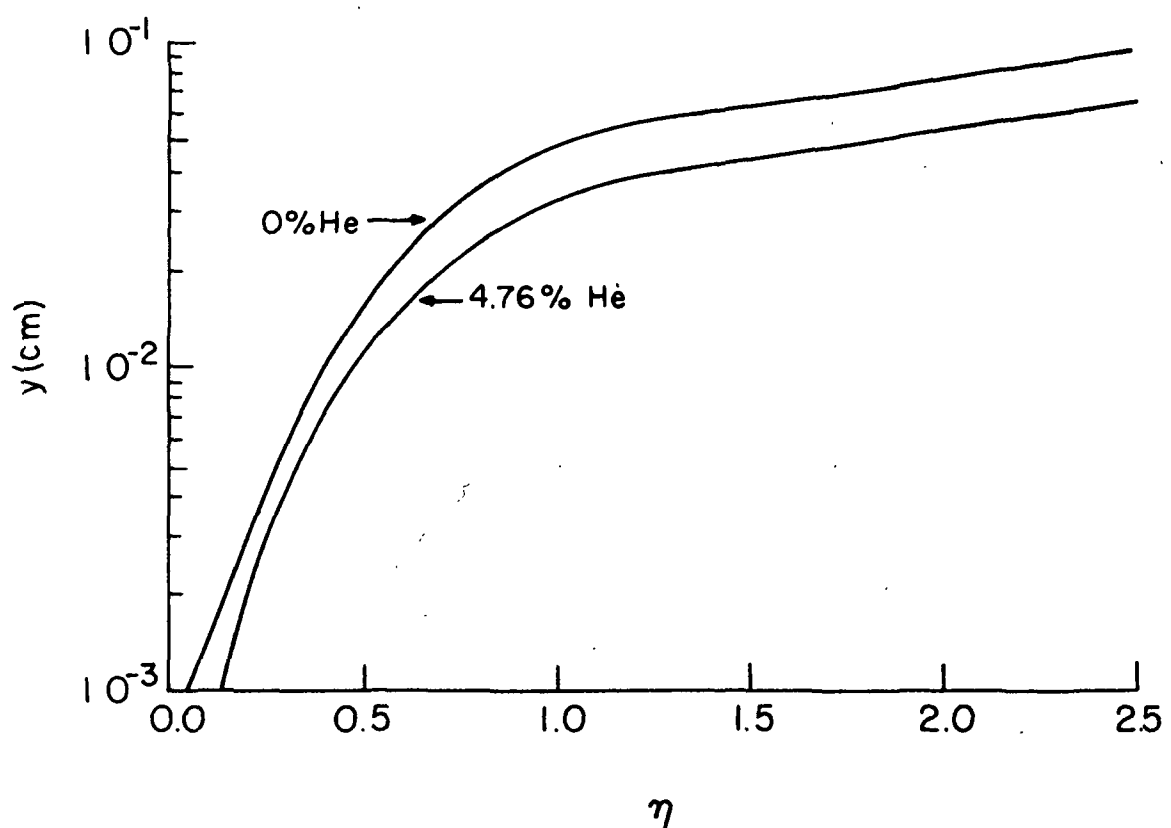


Figure 2.11

Conversion from  $\eta$  axis to  $y$ -axis for variable transport parameter calculation, small exit nozzle with contamination at  $x_p = 2.0$  cm

a contamination level of one percent is not much below the pure Argon value, but occurs slightly higher in the boundary layer; the free stream value for the one percent level is considerably lowered.

The 4.76% by mass Helium content resulted in a drop in the peak ionization of almost two orders of magnitude. The actual thickness of the boundary layer, however, was changed very little by the Helium contamination.

The changes in the transport properties due to the presence of Helium are shown in Figures 2.12, 2.13, 2.14; Figures 2.12 and 2.13 are profiles of the thermal conductivity and viscosity, respectively, for the same calculations as the preceding drawings. Notice how a small amount of Helium, in this instance 1% by mass, does not destroy the basic shape of the curves, but only changes the positions of maxima and minima. At a level of 4.76% mass Helium, the situation is quite different, and the influence of ionization upon the results are greatly abated.

Figure 2.14 shows how the modifications of the transport properties feeds through to the transport parameters of Prandtl Number and  $C_1$ . The same basic comments made previously hold here also. With 4.76% Helium by mass, the Prandtl Number is practically a constant throughout the whole boundary layer.  $C_1$  is also drastically changed. The most important feature here is the modification to the value of the gradient of  $C_1$  at the surface. It is most interesting that these changes are such to maintain the surface heat transfer rate at almost the same value regardless of the level of Helium for the figures shown.

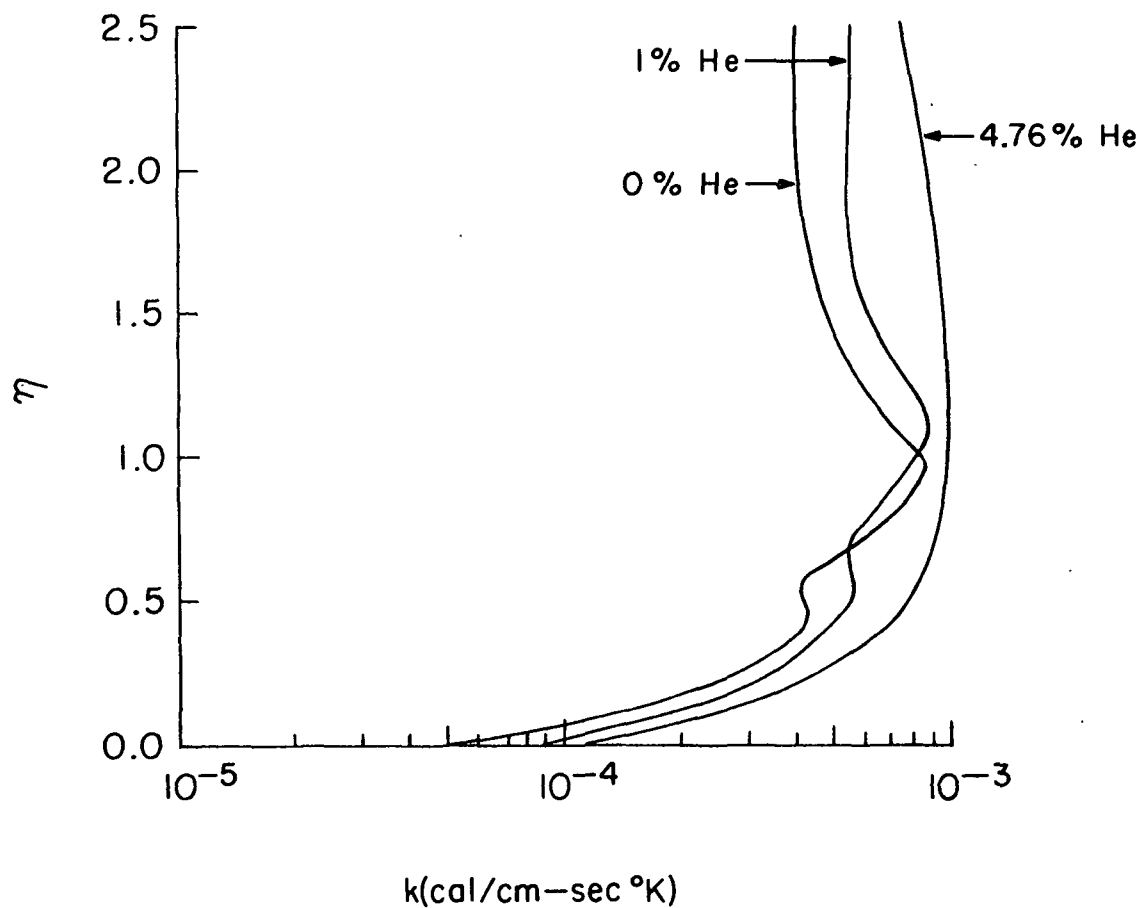


Figure 2.12

Thermal conductivity for variable transport parameter calculation with contamination at  $x_p = 2.0 \text{ cm.}$ , equilibrium boundary layer

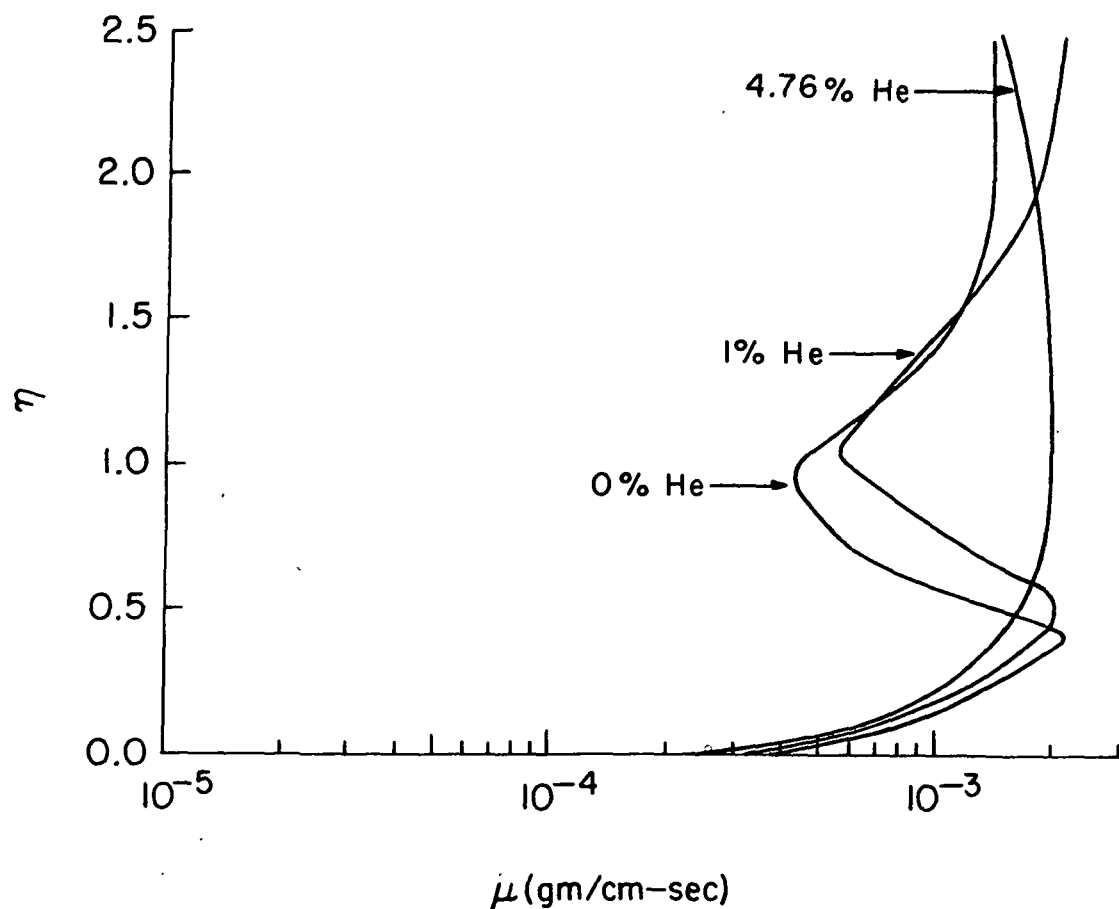


Figure 2.13

Viscosity for variable transport parameter calculation  
with contamination at  $x_p = 2.0 \text{ cm.}$ , equilibrium boundary  
layer

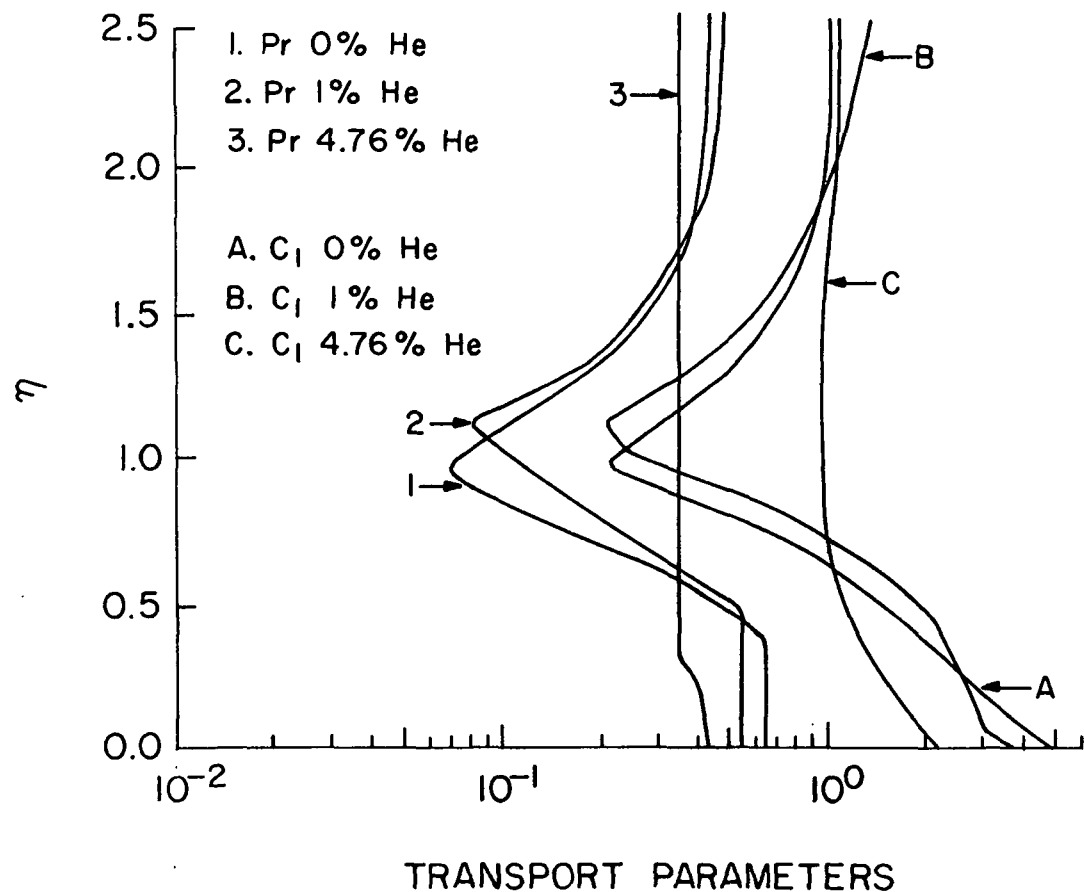


Figure 2.14

Transport parameters for variable transport parameter calculation with contamination at  $x_p = 2.0 \text{ cm.}$ , equilibrium boundary layer

Figure 2.15, the calculated surface heat transfer rates, shows the importance of using a variable transport parameter calculation. With a constant parameter solution, it would appear that a substantial lowering of the heat transfer would occur with contamination. However, it turned out in each case that the transport parameter derivatives were of such a value to compensate and the final heat transfer rates predicted varied very little, regardless of the contamination level up to at least 5% by mass.

#### Frozen Boundary Layer

If there are no chemical reactions in the boundary layer during the period of interest, the chemistry is considered "frozen."

All results shown will be for the small exit nozzle, 9.5° plate inclination, and at a distance up the plate from the leading edge of 2 cm.

Figure 2.16 shows the velocity profiles for a frozen boundary layer with a fully catalytic wall. A contamination level of 1% Helium by mass modifies the velocity profile.

Figures 2.17 and 2.18 are the temperature and density profiles for the above conditions. 1% Helium by mass lowers the temperature throughout the boundary layer, by partition of the total available enthalpy. The density was also lowered, and the maximum decrease correlates with the maximum difference between the velocity profiles.

Figure 2.19 is the ionization profile. As can be seen, the level of ionization is reduced considerably by introduction of 1% mass Helium. The smaller number of electrons in the gas will produce an increase in the viscosity. Consequently, it is not surprising that the viscous effects cause the velocity to start to drop off at a higher level in the boundary layer.

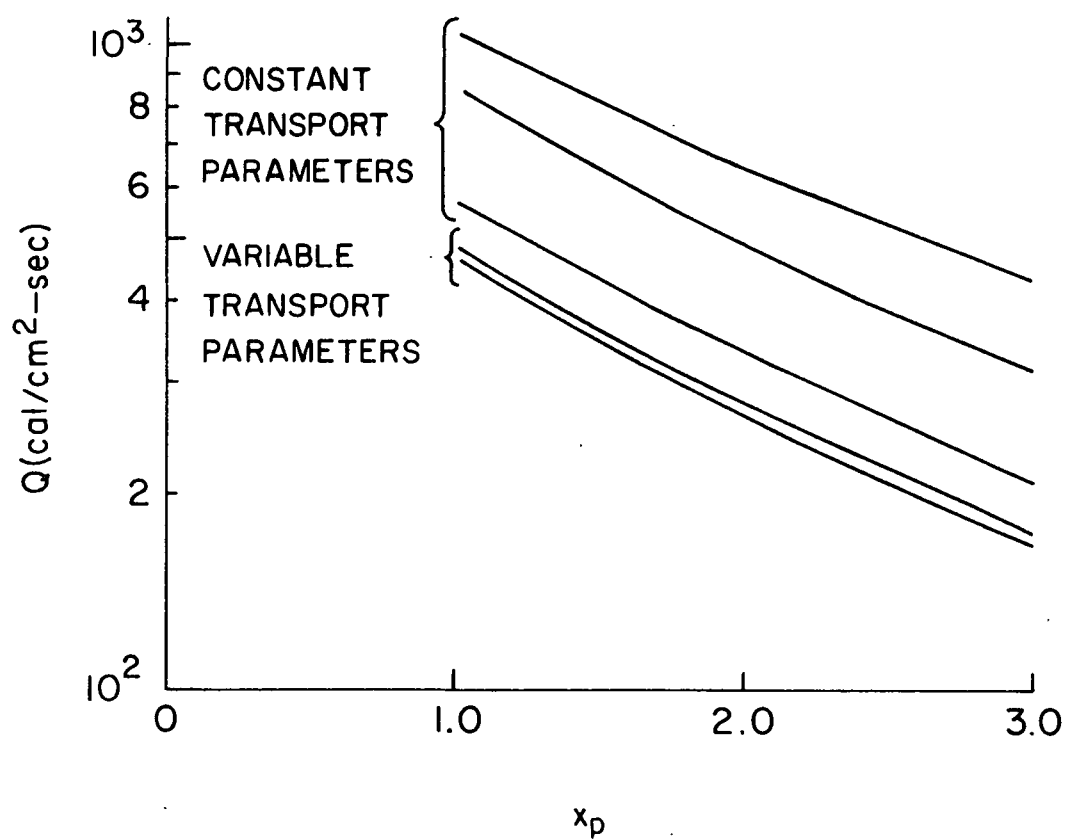


Figure 2.15

Calculated surface heat transfer rates for small exit nozzle with contamination, equilibrium boundary layer

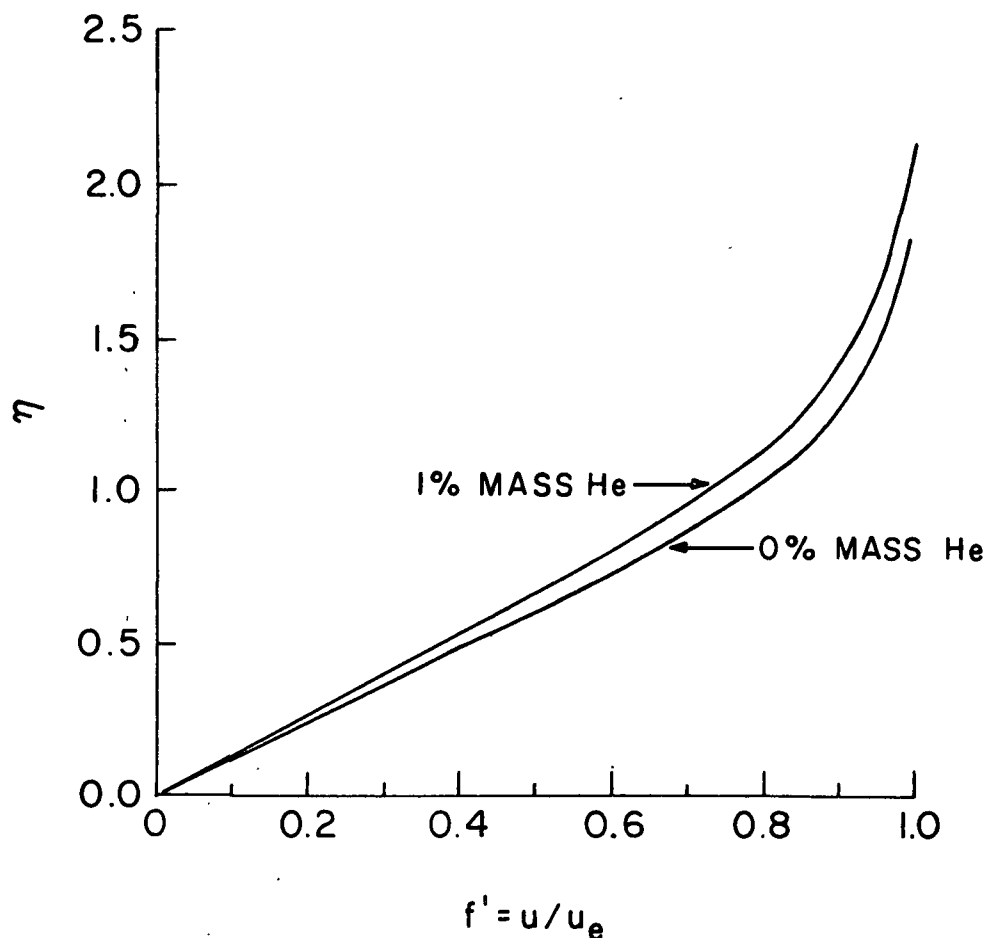


Figure 2.16

Frozen boundary layer velocity profile for small exit nozzle,  $9.5^\circ$  plate inclination,  $x_p = 2.0$  cm., 100% catalytic surface, with Helium contamination

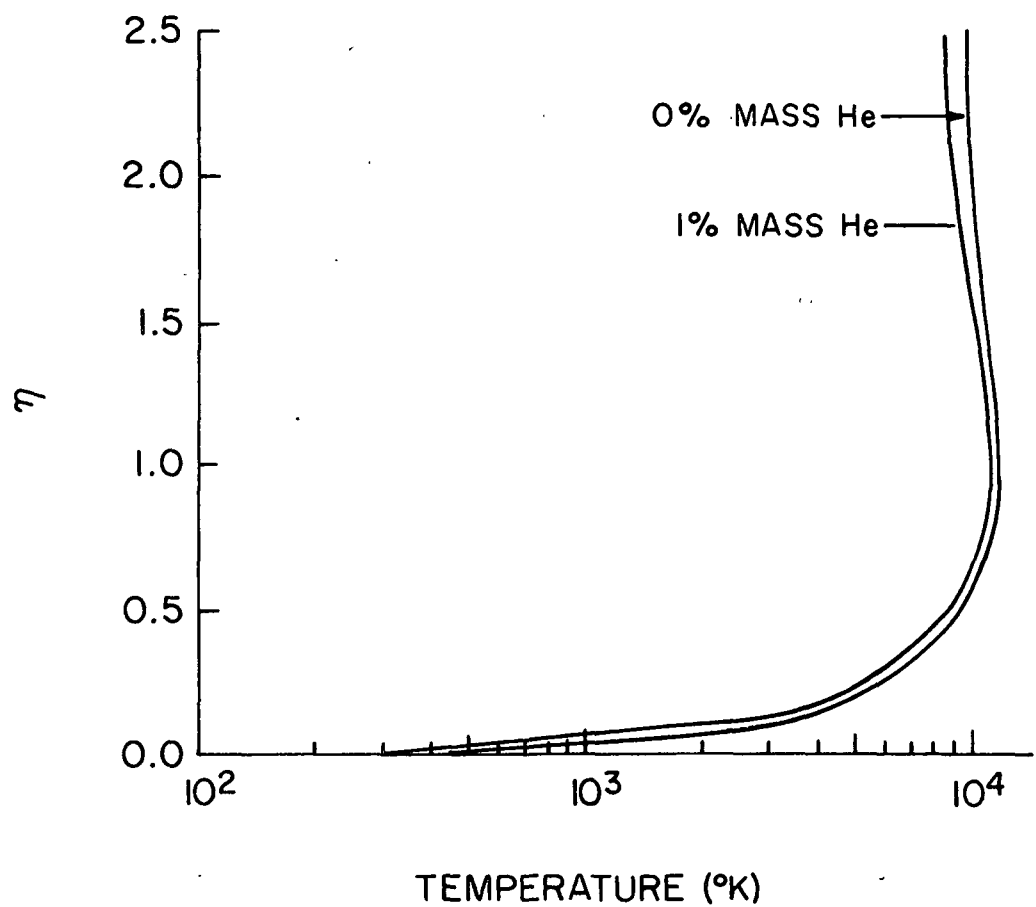


Figure 2.17

Frozen boundary layer temperature profile for  
small exit nozzle,  $9.5^\circ$  plate inclination,  $x_p = 2.0$  cm.,  
100% catalytic surface, with Helium contamination

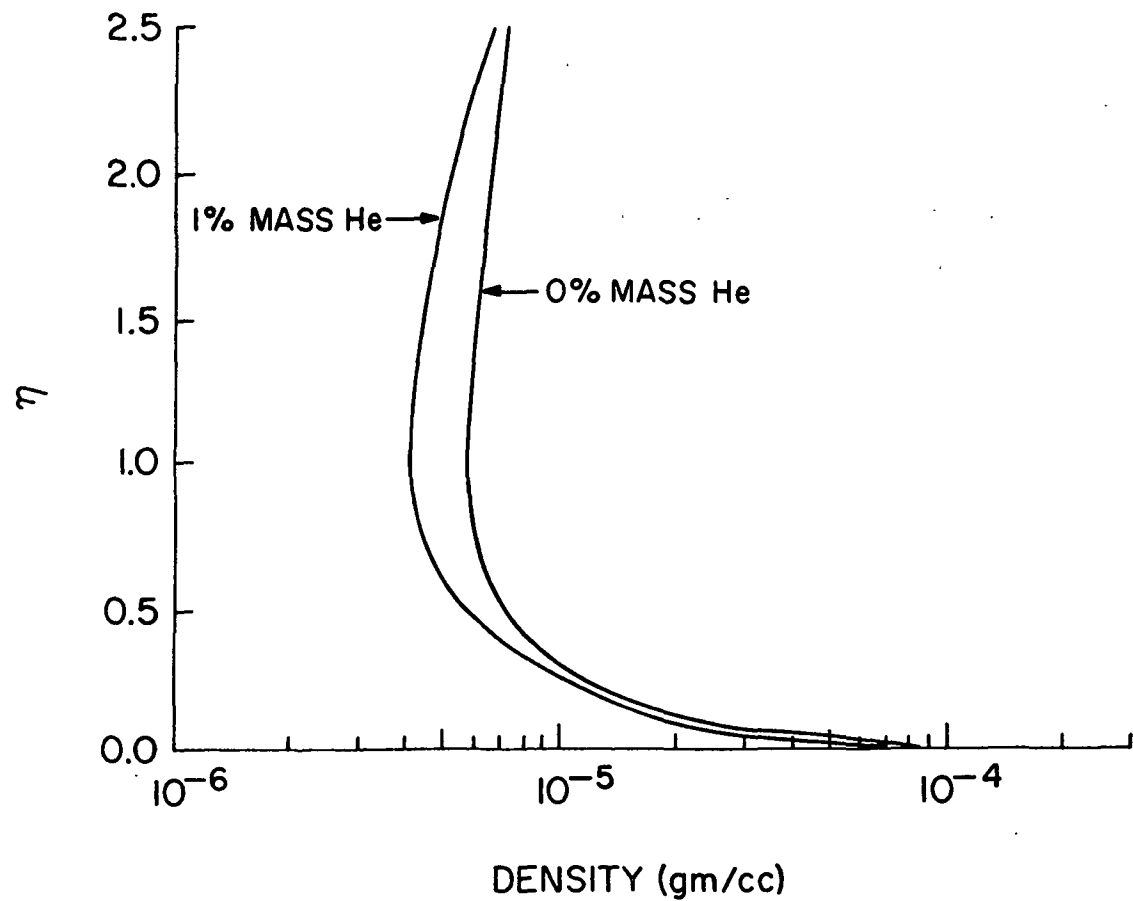


Figure 2.18

Frozen boundary layer density profile for small exit nozzle, 9.5° plate inclination, 100% catalytic surface,  $x_p = 2.0$  cm., with Helium contamination

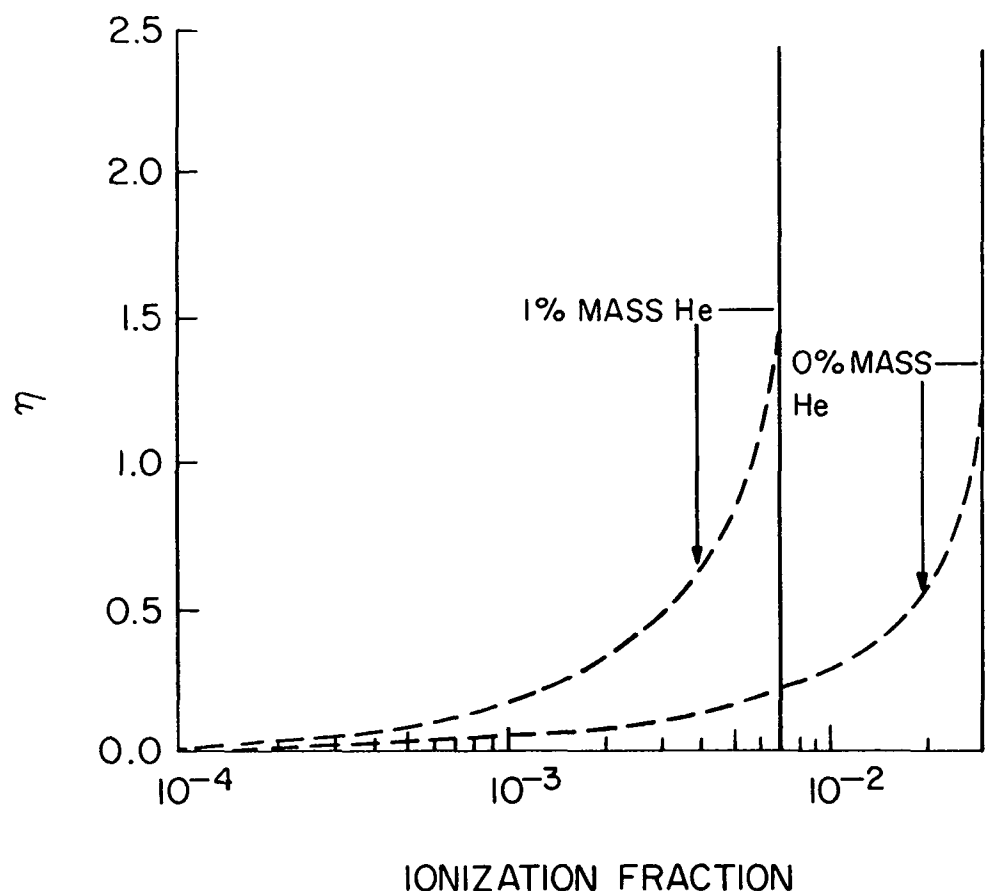


Figure 2.19

Frozen boundary layer ionization profile for small exit nozzle,  $9.5^\circ$  plate inclination, 100 % catalytic surface,  $x_p = 2.0$  cm., with Helium contamination. Solid line 100 % non-catalytic surface; dotted line 100 % catalytic surface

<u>Region</u>	<u>Gas</u>	<u>Displacement</u>
		<u>Thickness</u> <u>Parameter</u> $\left( \frac{\delta^*}{R_x^*} \right)$
Throat	100% Ar	assumed 0
	95.24% Ar + 4.76% He	assumed 0
	100% He	assumed 0
2.24 cm down stream	100% Ar	less than 3.0E-04
	95.24% Ar + 4.76% He	less than 3.0E-04
12.88 cm down stream	100% Ar	less than 2.0E-04
	95.24% Ar + 4.76% He	order of .8.0E-04
	100% He	order of 3.0E-03

TABLE 2.9

Relative Nozzle Displacement Thickness

Figure 2.20 shows the difference that Helium contamination causes in the conversion from the  $\eta$  to the  $y$  axis.

A level of 1% mass Helium in the boundary layer caused essentially no change to the surface heat transfer rate for the fully catalytic plate and therefore no graph is shown. This result is explained in the following manner. The free stream ionization is lower with contamination and consequently the diffusion of ion-electron pairs to the surface contributes less to the overall heat transfer. However, the temperature gradient at the surface, as shown in Figure 2.17, is larger and compensates by producing a larger conduction of heat flux to the surface. The thermal conductivity at the surface is made larger with the presence of Helium. These results mean that the lowering of the surface heat transfer rate with a non-catalytic surface is not as great with Helium contamination.

## 6. Summary of Part 2

This study has included the effects of enthalpy loss and Helium driver gas contamination. The results of the work have been used to predict the nozzle exit conditions for a pure Argon test gas flow and with various levels of Helium contamination. The Helium increases the exit Mach Number of the nozzle, while lowering the temperature. Calculations were then made of the changes to these values when the gas flow traverses an oblique shock front.

The presence of Helium will alter the displacement thickness of the boundary layer in the throat and on the walls of the nozzle. However, this parameter remains small in all cases and would not be expected to cause any changes to the effective area ratio of the nozzle.

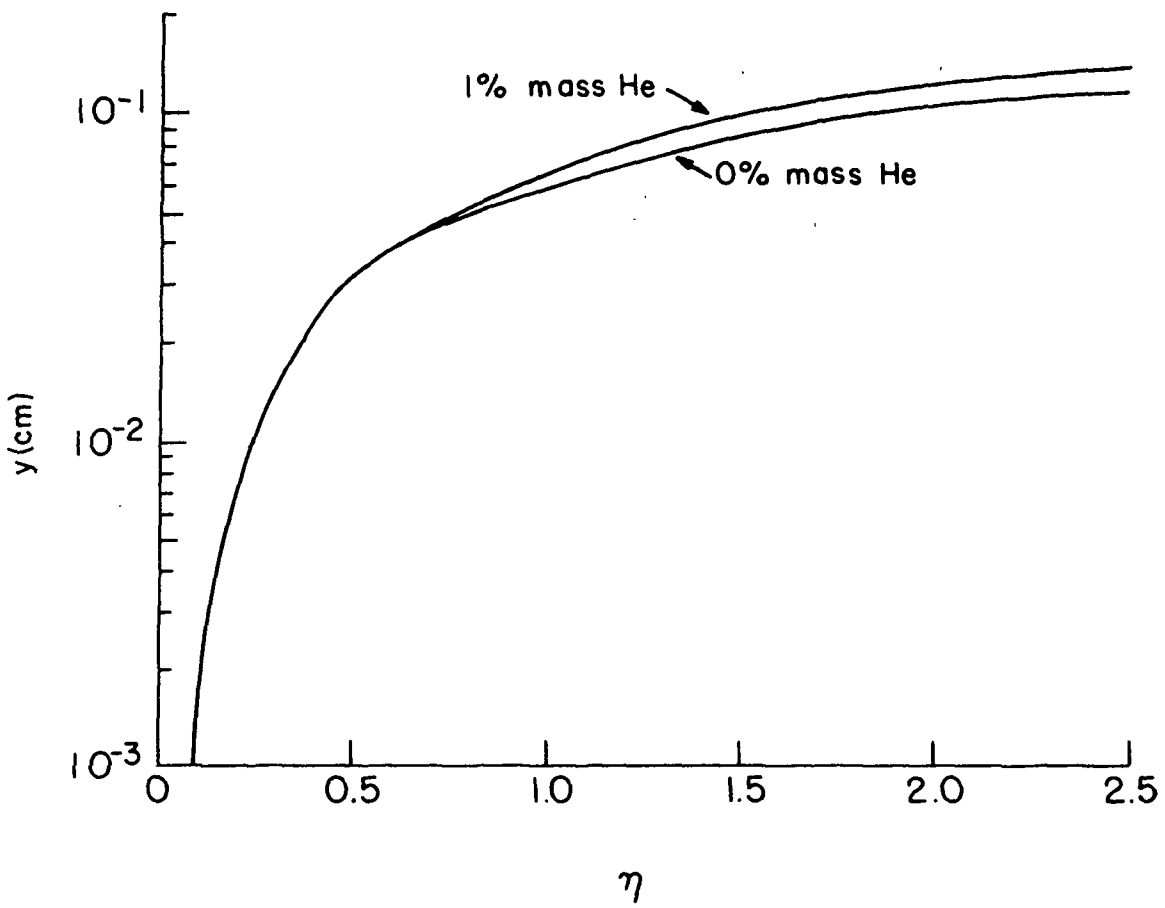


Figure 2.20

Conversion from  $\eta$  axis to the  $y$ -axis for the frozen boundary layer,  
small exit,  $9.5^\circ$  plate inclination,  $x_p = 2.0$  cm., 100 % catalytic surface

The flat plate boundary layers are also affected by the presence of Helium. The Helium lowers the temperature, density, and ionization in the boundary layer. If contamination levels of 5% by mass are reached the general profiles of the thermal conductivity and viscosity will be greatly altered.

With regard to calculations of equilibrium boundary layers with full variation of the transport properties, and frozen boundary layers with fully catalytic surfaces, the Helium contamination up to about 5% by mass will cause practically no change to the surface heat transfer rates. In the case of a frozen, non-catalytic surface calculation with contamination, the lowering of the heat transfer by the absence or diminishing of the diffusion of electron-ion pairs is lessened due to the lower level of free stream ionization.

**PART 3**

**EXPERIMENTS AND DATA CORRELATION WITH THEORY\***

## 1. Introduction

The Free Piston Shock Tunnel is unique in its ability to produce very high stagnation enthalpy flows. In this study, conditions were used which gave rise to a calculated stagnation enthalpy of 7,635 cal/gm for a pure Argon flow. This figure would be in excess of 100% greater than that obtainable with combustion driven shock tunnels.

The Free Piston Shock Tunnel is a comparatively new device, and it is important to carefully check the flow behavior to determine test times for various experiments. In Part 3, experimental data will be presented and discussed for test section pitot pressure, and surface heat transfer rates on the flat plate.

In all the data shown, the point is the mean average of many determinations, and the flags are the standard deviations of the data.

For details of the equipment and data reduction methods the reader is in reference to Yanow (1971).

## 2. Properties of the Test Section Flow

### Calculated Conditions

The test section has previously been discussed in Part 2 of this paper. However, for purposes of clarity, the calculated pure Argon flow nozzle exit conditions are repeated below in Table 3.1 with some additional information.

### Pitot Pressure Measurements

For ease of reading Figure 2.4, the calculated test section pitot pressures are redrawn.

The first experimental points are based on the Pitot pressure measurements taken 85 micro-seconds  $\pm$  15 micro-seconds from the

	Large Exit Nozzle	Small Exit Nozzle
Area Ratio	1204	147
Density (gm/cc)	6.76 E-7	5.86 E-6
Ionization Fraction	assumed 0	0.008
Temperature ( $^{\circ}$ K)	2,816	8,335
Pressure (dyne/cm $^2$ )	3.97 E+3	1.02 E+5
Velocity (cm/sec)	7.81 E+5	7.38 E+5
Speed of Sound (cm/sec)	9.89 E+4	1.52 E+5
Mach No.	7.90	4.87
Effective Gamma	1.67	1.32
Pitot Pressure (dyne/cm $^2$ )	4.13 E+5	3.19 E+6
Thermal Conductivity (cal/cm-sec- $^{\circ}$ K)	2.24 E-4	4.08 E-4
Viscosity (gm/cm-sec)	1.16 E-3	1.95 E-3
Specific Heat (cal/gm- $^{\circ}$ K)	0.1247	0.1257
Prandtl Number	0.64	0.60
$\rho k / \rho_w k_w$	0.571	0.348
Local Reynold's Number	9.14 E+3	2.99 E+4

TABLE 3.1  
Calculated Conditions at the Exit of the Nozzles, no losses

time of shock reflection. The experimental technique used is discussed fully in Yanow (1971). There is good agreement between theory and experiment, validating the assumption of isentropic nozzle flow with insignificant boundary layer effects at this time.

The pitot pressure at a flow time of 160 micro-seconds  $\pm$  15 micro-seconds from shock reflection is a different matter. The measured value dropped by a very significant amount. Three typical oscillograms illustrating this pressure fall are shown in Figures 3.1a, 3.1b, and 3.1c. The data of Figure 3.1a has a time base of 50 micro-seconds per division, while that of Figure 3.1b is 20 micro-seconds per division. Both traces are for the small exit nozzle; Figure 3.1c has a 20 micro-second base and is large exit data.

The initial 30-40 micro-seconds of the traces can be attributed to nozzle starting time. The rise time of the pitot pressure gauge was a function of the density of the gas flow. In the instance of the small exit unit, this latter time was estimated at about 30 micro-seconds, and when using the 15° half angle nozzle this period lengthened to about 40-50 micro-seconds.

At first glance, these observations look analogous to the pressure dip in the reflected shock region, observed by Dunn (1969a, 1969b) and others. Dunn explained this dip as resulting from an expansion wave generated at the initial interaction of the reflected shock and the driver-test gas interface. Dunn also defined the usable test time as the period required for this expansion wave to reach the shock tube end wall, and obtained typical values for usable test time of about 200 micro-seconds. Stalker (1967) has observed a dip in reflected shock pressure measurements of the Australian National University device at

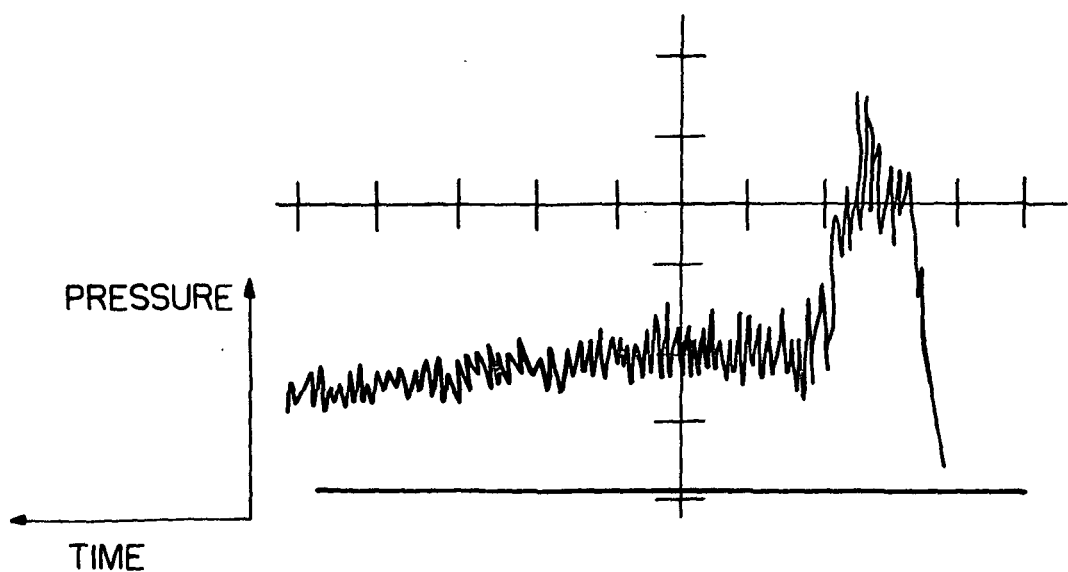


Figure 3.1a

Typical pitot pressure oscillogram for small exit nozzle with 50 micro-seconds/division time base

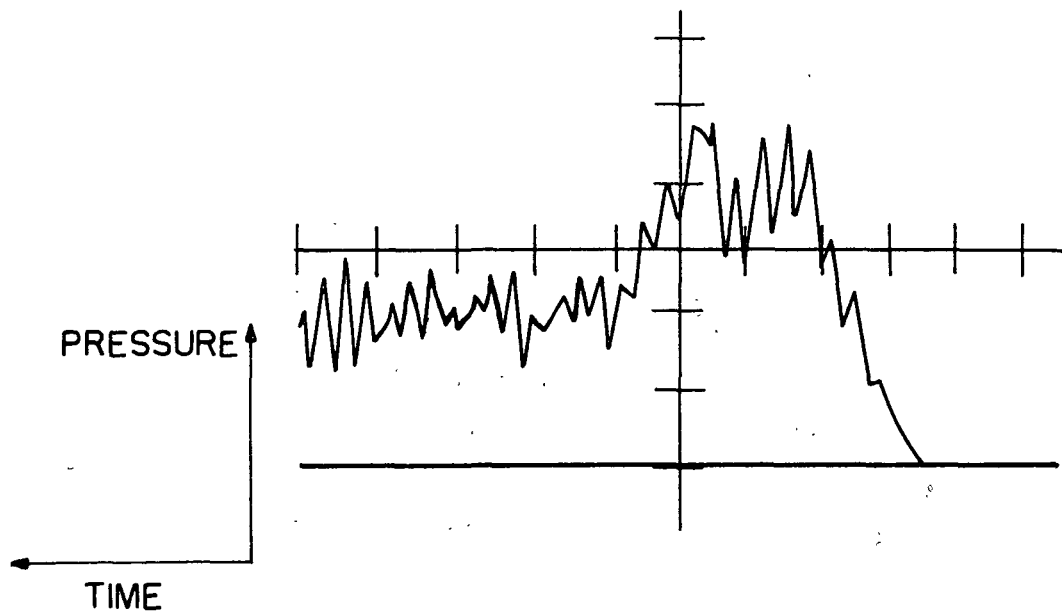


Figure 3.1b

Typical pitot pressure oscillogram for small exit nozzle with 20 micro-seconds/division time base

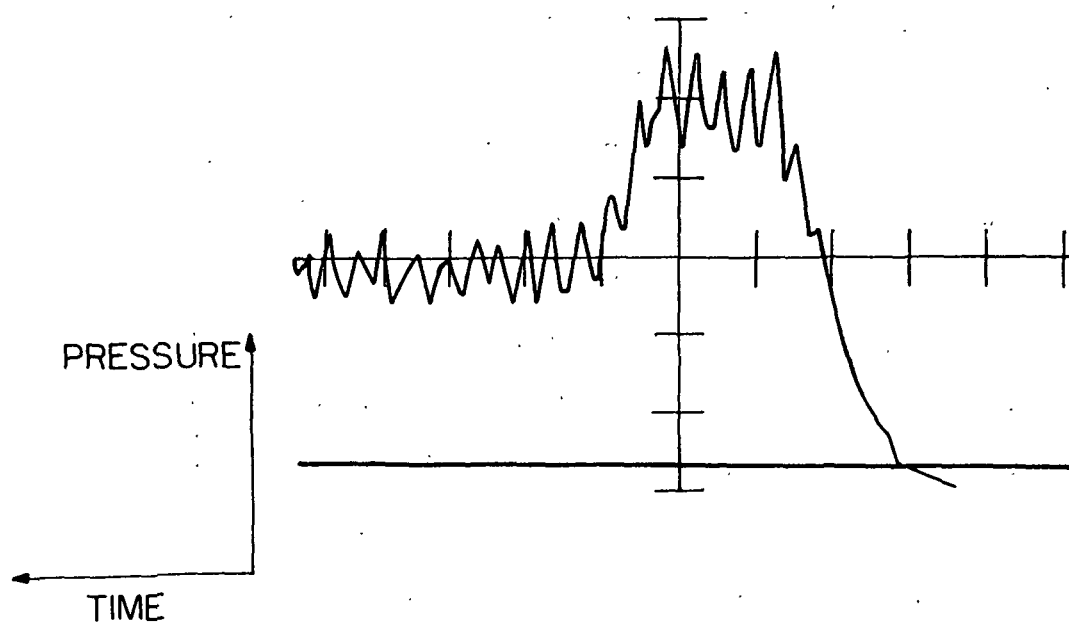


Figure 3.1c

Typical pitot pressure oscillogram for large exit nozzle with 20 micro-seconds/division time base

approximately 20-30 micro-seconds after shock reflection. Logan (1971) using streak photography has correlated this time interval with the period required for the expansion wave to reach the end wall. Thus the pressure dip arising from the reflected shock expansion occurs on a time scale which is too short to be clearly evident in the pitot pressure traces, indicating that the observed pitot pressure drop must be due to some other source.

Davies and Wilson (1969) have investigated the problem of interaction of the reflected shock front and shock tube boundary layer. As the reflected shock moves back up the shock tube, it comes in contact with the wall boundary layer formed after the initial forward passage of the front. The stagnation pressure of the majority of this boundary layer is less than that of the free stream, and therefore the boundary layer gas may not penetrate the reflected shock front. Because the boundary layer cannot negotiate this pressure jump, it separates ahead of the shock. An oblique shock forms at this point, and eventually combines with the normal front at some distance from the surface. This is illustrated in Figure 3.2.

Boundary layer gas is trapped under the separated region beneath the shock, and is carried along with the front. This system is known as a "bifurcated foot." Some of the gas immediately above the boundary layer traverses the double oblique shock system ahead of the reflected shock and into the region behind it. A small amount of the boundary layer gas may also get passed across this shock configuration, and if so it will move along the wall with the other penetrating gas toward the end of the shock tube at a velocity higher than that of the reflected shock free stream.

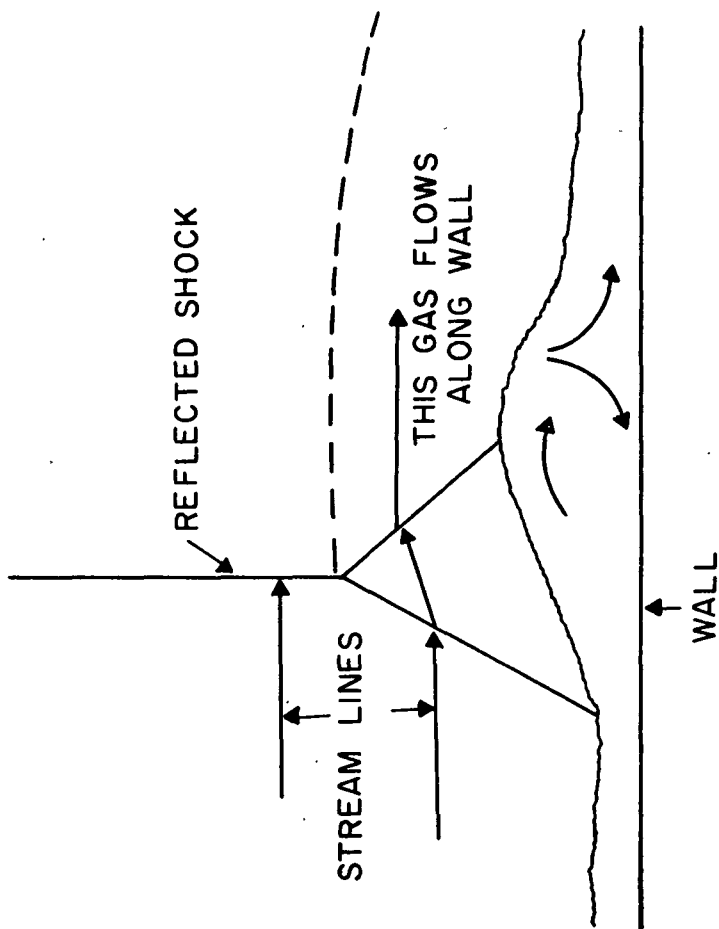


Figure 3.2

Bifurcated Shock

It is possible, according to Davies and Wilson, that when the reflected shock passes through the Helium-Argon contact surface a small amount of Helium driver may leak into the test gas slug, move along the side wall, gather at the nozzle end of the shock tube, and finally move toward the center in front of the entrance to the throat of the nozzle.

Based on the discussion in Part 2, the drop in test section Pitot pressure is not likely attributed to energy loss mechanisms, Helium mixing with the Argon in the reflected shock region, or the Helium altering the throat or nozzle wall boundary layer.

When Helium was used as a test gas and a driver gas, no Pitot pressure drop was observed. This suggests that the fall of Pitot pressure is due to some difference between the flow characteristics of the Argon and Helium. Consequently, a plausible explanation for the observed Pitot pressure is that the contaminating, relatively cold Helium gathers at the nozzle end of the reflected shock region and moves toward the center of the shock tube. When this gas mass reaches the area of the throat, it feeds into the periphery of the Argon flow. The Helium may occupy a greater relative area in the throat than further down the nozzle, as shown in Figure 3.3. This would effectively increase the area ratio as far as the Argon was concerned and thereby cause a Pitot pressure drop. The possibility of this happening can be substantiated using a very simple argument.

Let it be assumed that the gases are not mixed in the reflected shock region, and the Argon and Helium are at the same approximate pressure in the general area of the throat. Let it also be assumed that when the Helium feeds into the throat, as described above, it

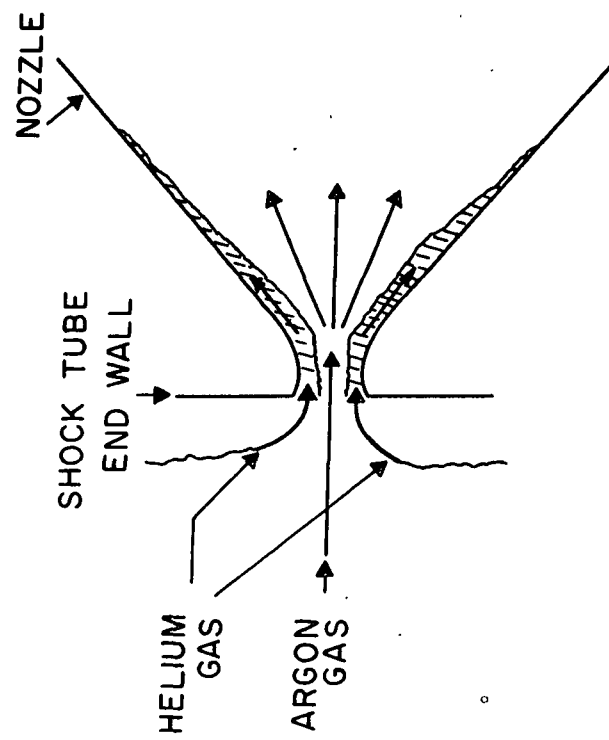


Figure 3.3

Change of effective nozzle ratio by Helium feeding into Argon flow

occupies a certain percentage of the total area. From the Argon real gas nozzle calculations, at an area ratio of 100 (that is, the area at the point in question in the nozzle is 100 times greater than the throat area occupied by the Argon), the gas pressure of the Argon would have dropped by a factor of about 800 of that in the throat. It would seem logical that the Helium would suffer approximately the same relative pressure drop. However, to obtain this the Helium would need only an area increase of about 20. This value was obtained using ideal gas relations. Therefore, the Helium would occupy a much smaller percentage of the total area.

This particular phenomenon of Pitot pressure drop could then be attributed to the fact that the Argon acts as a real ionizing gas in the nozzle flow, while the Helium acts as an ideal gas with no ionization.

### 3. Boundary Layers

#### Leading Edge Effects

It is not the aim of this project to carry out an investigation of the leading edge effects associated with rarefied hypersonic flow. Indeed, the object of using an inclined flat plate was to maintain a very high stagnation enthalpy while avoiding this problem area. However, it is important that a sufficient study be made to be sure of this point.

The generally accepted flow picture is that at, and very near to, the leading edge, the gas flow is described by kinetic theory. This area is followed downstream by a region of transition to what is known as the "merged region." Pan and Probstein (1966) characterize the merged region by continuum flow where the viscous boundary layer and oblique shock wave are merged. There may be wall slip. Further

downstream there are the regions of strong interaction and then weak interaction. These are depicted by the fact that the boundary layer and shock front separate and a region of inviscid flow forms between them. However, they are in close enough proximity for the boundary layer to affect the position of the shock front. The resultant curvature of the shock produces a pressure gradient.

Heat transfer measurements made in the merged region, as indicated by Vidal, Golian, and Bartz (1963), will fall below the predictions made using the equations derived in Part 2 of this paper. Measurements made in the strong interaction region must also be rejected because of the existance of a significant pressure gradient.

McCroskey, Bogdonoff, and McDougall (1966) have shown that the relevant merged region interaction parameter is given by

$$\bar{V} = M_2 (C/Re_2)^{1/2} , \quad (3-1)$$

where  $C$  is the constant in a linear viscosity law and  $M_2$  and  $Re_2$  are the post oblique shock Mach Number and local Reynold's Number, respectively. McCroskey, et al., experimentally demonstrated that when  $\bar{V}$  has a value between 0.15 to 0.20, merged region effects, such a lowering of the surface density and heat transfer, could be expected.

Dorrance (1962) has shown that the relevant strong interaction parameter is

$$\bar{X} = M_2^3 (C/Re_2)^{1/2} . \quad (3-2)$$

From the work of Hayes and Probstein (1959), it appears that strong interaction would be present for values of  $\bar{X}$  greater than 3 or 4, and weak interaction would be the criteria below these values.

Table 3.2 shows the calculated values of  $\bar{V}$  and  $\bar{X}$  at 1, 2, and 3 cm. up the plate from the leading edge for the small exit,  $9.5^\circ$  plate inclination, and for the large exit,  $19.5^\circ$  plate inclination data, with a pure Argon flow. The values of the Mach Number and the Reynold's Number at each point have been calculated with flow divergence considered in the manner described in Part 2. The only measurement that might suffer some merged region influence is at 1 cm. with the large exit nozzle, at a plate inclination of  $19.5^\circ$ . It would appear that the strong interaction region is very limited in extent<sup>1</sup> and consequently the assumption of a zero induced pressure gradient is valid to a good approximation.

It has been assumed that the flat plate induced pressure gradient can come about only through some form of leading edge effect and not by changes in the free stream conditions. In his discussion Dorrance (1962)<sup>2</sup> shows that if  $g_w$  is small and the pressure gradient parameter varies "slowly", the integrated boundary layer solutions seem insensitive to the variation of the pressure gradient. Further experimentally, the concept of "local similarity", i. e. the integration of the boundary layer equations at a specific location using the free stream conditions present there, has been proven to be acceptable. Accordingly, in this

<sup>1</sup> It should be noted that Rudman and Rubin (1968) in an experimental study determined that the merged region went directly into the weak interaction region when the free stream Mach Number was equal to or less than 8.

<sup>2</sup> See chapter 4.

work the two dimensional flat plate boundary layer equations have been solved at different locations up the plate using the free stream conditions calculated at the respective positions.

#### Heat Transfer

Figure 3.4a shows typical data to calculate the Argon heat transfer rate. The upper and lower traces were recorded by gauges 1.75 and 2.25 cm. up the plate from the leading edge, respectively. There is a dramatic change in the character at approximately the same time that the Pitot pressure drops. The initial noise is mainly attributed to the presence of electrons in the flow. After the Pitot pressure drops, the heat transfer also falls, and at the same time the noise for the most part disappeared. It is suggested that this last point is due to the quenching of the flow ionization by the injection of Helium into the test gas..

Figure 3.4b indicates typical heat transfer information obtained when Helium was used both as the driver and test gas. This data is shown for comparison purposes with Figure 3.4a. The upper and lower traces were made by gauges 1.1 and 2.66 cm. up the plate from the leading edge. Note that there is no change in slope, and that the curves are for all practical purposes noise free. The former point is important, and it correlates with the fact that no Pitot pressure drop was observed with a Helium driver Helium test gas arrangement.<sup>1</sup> The noise free traces are again attributed to the fact that there was no ionization of the Helium.

---

<sup>1</sup> Pitot pressure measurements with air as the test gas showed the same large scale fall as with Argon.

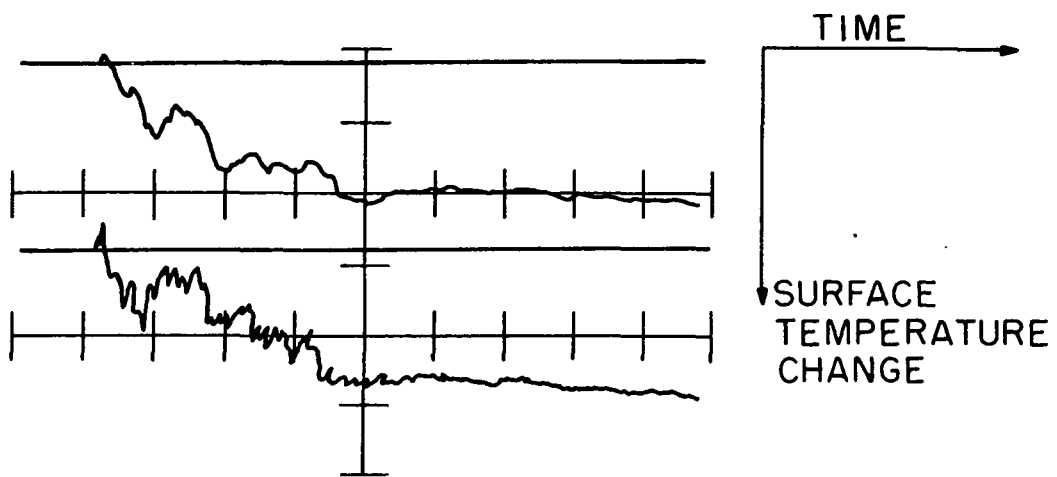


Figure 3.4 a

Drawing of typical surface temperature history in Argon flow. Time base is 20 micro-seconds/division

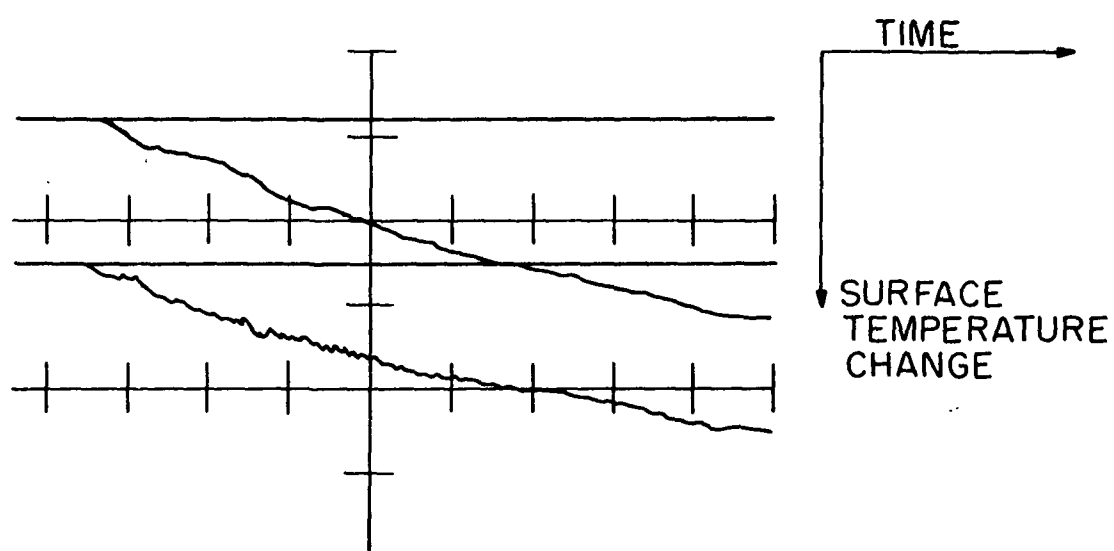


Figure 3.4b

Drawing of typical surface temperature history in Helium flow. Time base is 20 micro-seconds division

DATA	DISTANCE UP PLATE (cm)	$\bar{V}$	$\bar{X}$
Small exit,	1	0.09	1.3
$9.5^\circ$ plate	2	0.08	1.3
inclination	3	0.07	1.3
Large exit,	1	0.14	1.4
$19.5^\circ$ plate	2	0.11	1.2
inclination	3	0.10	1.2

TABLE 3.2

Calculated Merged Region and Strong Interaction Parameters

Figure 2.15, redrawn here for reference, shows the calculated and measured surface heat transfer rates for boundary layers in thermo-chemical equilibrium. Theoretical predictions are shown for both the cases of constant and variable transport parameters. The measured results are for a period approximately 85 micro-seconds after shock reflection. It is reiterated that in the figures the point is the mean value of many determinations, and the flags are the standard deviations of the data.

The measurement at 1.1 cm. distance up the plate has probably suffered merged region effects, as suggested in Table 3.2. The variable transport parameters markedly lowered the surface heat transfer rate. The large exit prediction and measurements are close to a factor of two from one another, the limit set as acceptable, but the correlation of the small exit measurements and theory is bad.

It was deemed wise at this point, based on the above results, to carry out a limited series of calculations and measurements for a pure Helium flow. The Helium would be divorced of real gas effects and thereby act as a check on the basic theory. The result, using an initial shock tube pressure of 10 inches Hg is shown in Figure 3.5, again for a time of about 85 micro-seconds after shock reflection. The large exit nozzle was used with a plate inclination of  $9.5^{\circ}$  and data is only shown for a gauge position 2.66 cm. up the plate from the leading edge. (The gauges closer to the leading edge could have possibly suffered merged region effects).

The experimental and calculated data showed reasonable agreement. If, with pure Helium, a fairly thick nozzle turbulent boundary layer did develop towards the exit, the flow divergence would be

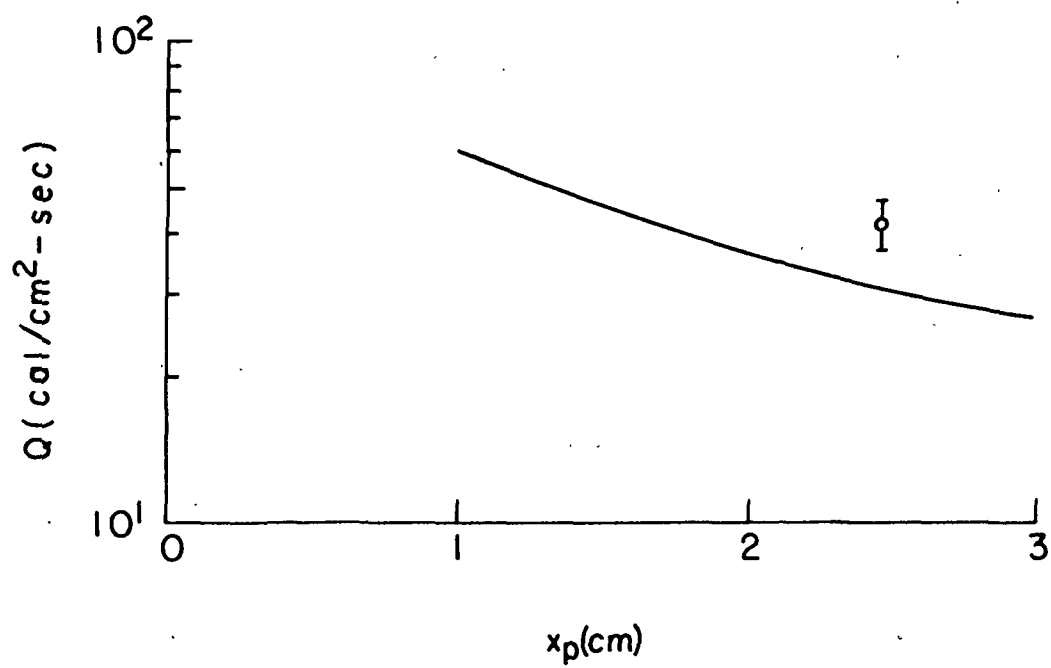


Figure 3.5

Helium heat transfer rate at approximately 85 micro-seconds after shock reflection, large exit nozzle, and  $9.5^\circ$  plate inclination. Constant transport parameters were assumed

lessened and the flow pressure would be increased. As a result, the measured heat transfer rate would be expected to be larger than the theoretical prediction.

#### Composite Boundary Layer Calculations

The chemically frozen boundary layer heat transfer predictions, with or without a catalytic surface, were higher than for a boundary layer in thermochemical equilibrium with variable transport properties. The results of Part 2 showed that Helium contamination would not lower the predicted heat transfer rates to correlate with the data, and some other mechanism must be found to account for the low heat transfer rates.

Wong and Bershad (1966) argued that after a shock the gas goes to a high temperature, given by the ideal gas equations. Atom-atom collisions occur which tend to produce a low level of ionization. Eventually, the electron numbers are sufficiently high to cause atom-electron reactions to predominate, with a subsequent rapid pick up of the ionization level. Finally, the gas reaches near equilibrium as the rate of recombination comes into balance with that of ionization. Any impurities will cause the above chain to proceed at a faster rate.

In the situation at hand, the same processes are at work. However, as outlined below, it is probable that the gas relaxation processes may be such as to promote a close approach to local equilibrium conditions near the wall.

Blottner (1964) has carried out a series of chemical non-equilibrium boundary layer calculations for air. He assumed the Prandtl number was either 1 or 0.7, and the Lewis number was either 1.0 or 1.4. His results showed that the temperature and composition profiles

of the non-equilibrium boundary layer could be considerably different from either equilibrium or frozen results. However, Blottner's constant transport property calculations did not suggest a major change in surface heat transfer rates.

Pallone, Moore, and Erdos (1964) carried out similar calculations in air. They, however, used variable transport properties. The maximum temperature in their boundary layers was about  $5000^{\circ}\text{K}$  and consequently the amount of ionization was small. This meant that the Prandtl number remained essentially constant in value at 0.75.

The inclusion of variable transport properties to the extent that occur in this work into a non-equilibrium calculation would be most difficult, and computer time consuming. This, coupled with the poor knowledge of the rate coefficients needed in the calculation, demanded that some easier approach to the problem of non-equilibrium be found. A simpler first approximation to the problem could be the defining of a level in a boundary layer, at which the gas would change from that of essentially frozen in character to that of essentially equilibrium in character. The question is how to establish the position of the point where the two solutions (i.e. chemically frozen and thermo-chemically equilibrium calculations) could be put together.

Continuing the practice adopted in the calculation of frozen boundary layers, let it be assumed that the free stream is in thermo-chemical equilibrium but that the upper portion of the boundary layer is in a chemically frozen state.

The equilibrium constant for chemical reactions is given by the ratio of the ionizing reaction rate coefficients over the recombination coefficients. Wong and Bershad (1966) give expressions for the

reaction rate coefficient for Argon ionization and for the recombination constant. They are, respectively

$$K_I = 10^{-6} \left\{ \frac{(2kT)^3}{\pi m_e} \right\} \left\{ 4.4 \left[ (\beta_E/T) + 2 \right] \exp(4\beta_E/T) + 9.5 \left[ (\Theta_I/T) + 2 \right] \exp(-\Theta_I/T) + 4.4 (\beta_E/T) \left[ 1 + (\Theta_I/T) \right] \left[ (\Theta_I/\beta_E) - 1 \right] \exp(-\Theta_I/T) \right\} \left[ \frac{\text{cm}^3}{\text{sec}} \right], \quad (3-3)$$

and

$$K_E = \frac{12 (2\pi m_e)^{3/2}}{h^3} (kT)^{3/2} \exp(-\Theta_I/T), \quad (3-4)$$

where

$\Theta_I$  = ionization temperature,  $^{\circ}\text{K}$  ( $1.828 \times 10^5$ ),

$\beta_E$  = excitation temperature,  $^{\circ}\text{K}$  ( $1.335 \times 10^5$ ).

Wong and Bershadec gave the rate coefficient for ionization,  $K_I$ , as a function of electron temperature, but the assumption will be made here of thermal equilibrium.

The first term in the second bracket of equation (3-3) is approximately 1000 times greater than the other terms, and to a good first approximation the latter terms may be ignored. Taking the recombination rate coefficient,  $K_R$ , as the ratio  $K_I/K_E$  and calculating the numerical constants, it is found

$$K_R = 1.3035 \times 10^{-32} \left[ \frac{13.35 \times 10^4}{T} + 2 \right] \exp \left[ \frac{4.93 \times 10^4}{T} \right] \left\{ \frac{\text{cm}^6}{\text{sec}} \right\}. \quad (3-5)$$

Figure 3.6 shows the value of the recombination rate coefficient given by equation (3-5). The recombination rate increases as the temperature falls, in agreement with a similar equation given by Knöös (1968). Notice how the value increases very rapidly below temperatures of about  $7000^{\circ}\text{K}$ , and therefore approach to the surface must promote an approach to equilibrium. Consequently, the recombination rate, that is the number of recombinations occurring per unit time, appears to be a reasonable criterion for determining the position of the matching layer in the composite boundary layer.

Wong and Bershadar assumed only a three body recombination process, i.e.



and therefore the rate of change of the electron numbers is given by

$$\frac{dN_e}{dt} = N_e N_A K_I - N_e^3 K_R , \quad (3-7)$$

where the term  $N_e^3 K_R$  is the recombination rate.

The integration of the boundary layer equations essentially defined 50 stream tubes within the boundary layer. The characteristic time in each stream tube for particles to remain in the region of interest was taken to be the period required for the gas particles to travel three cm. from the leading edge up the plate.

The criterion where the solution was switched from a frozen integration to an equilibrium integration was then taken to be given by

$$I_c < \frac{N_e}{N_e^3 K_R t_c} , \quad (3-8)$$

where  $t_c$  is the characteristic time and  $I_c$  is some arbitrary constant to be determined.

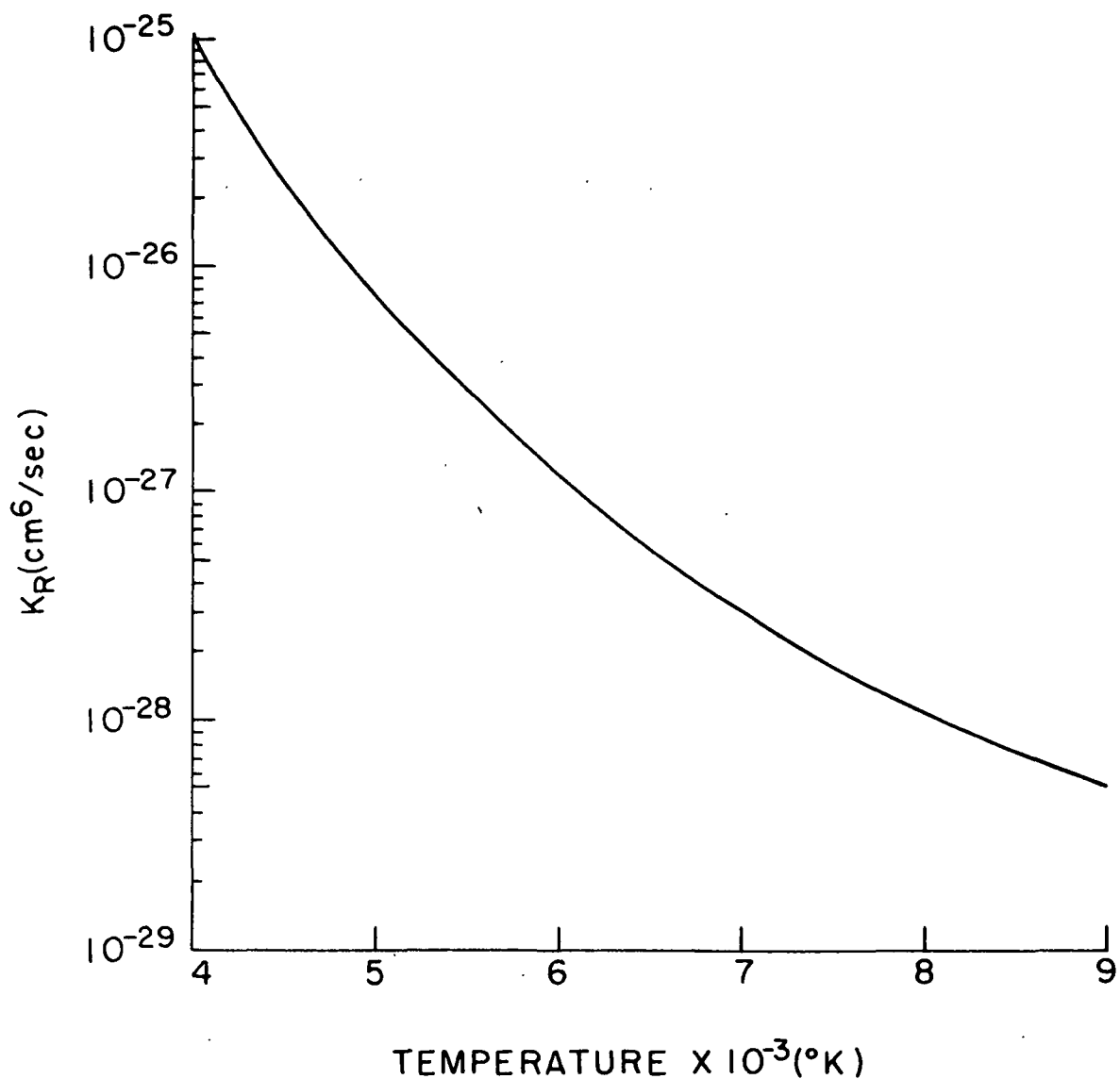


Figure 3.6

Recombination rate coefficient for Argon

Equation (3-8) can be interpreted as meaning that if the number of electrons is greater than some factor times, the possible number that could be recombined within the characteristic time, the gas is defined as frozen.

Figure 3.7 shows how rapidly the value of this criterion changes with temperature. Referring back to Figure 2.17, the temperature profile of the frozen boundary layer shown here again for convenience, it can be appreciated how suddenly the changeover of the two conditions might indeed be.

Changeover stream tubes were defined based on choices of  $I_c$  nearest the values of 10 and 100. Table 3.3 shows the choices of stream tube<sup>1</sup>, the corresponding values of temperature, the constant  $I_c$ , and the height above the surface.

The problem of matching the lower equilibrium and upper frozen calculations in a composite boundary layer bears some comment. To be correct, not only should the actual values of enthalpy and velocity be matched, but also their derivatives. The enthalpy gradient,  $g'$ , and velocity gradient,  $f''$ , respectively, are measures of any heat flux or shear stress passed across the changeover layer from the frozen portion to the equilibrium portion of the composite boundary layer.

The boundary layer equations, however, were not designed to accommodate non-zero values of  $g'$  and  $f''$  as  $\eta \rightarrow \infty$ . That is, it was assumed that once the values of  $g$  and  $f'$  went to unity, they would remain at this value and therefore the gradients of these quantities would go to

---

<sup>1</sup>These values are based on integrations at two cm. up the plate.

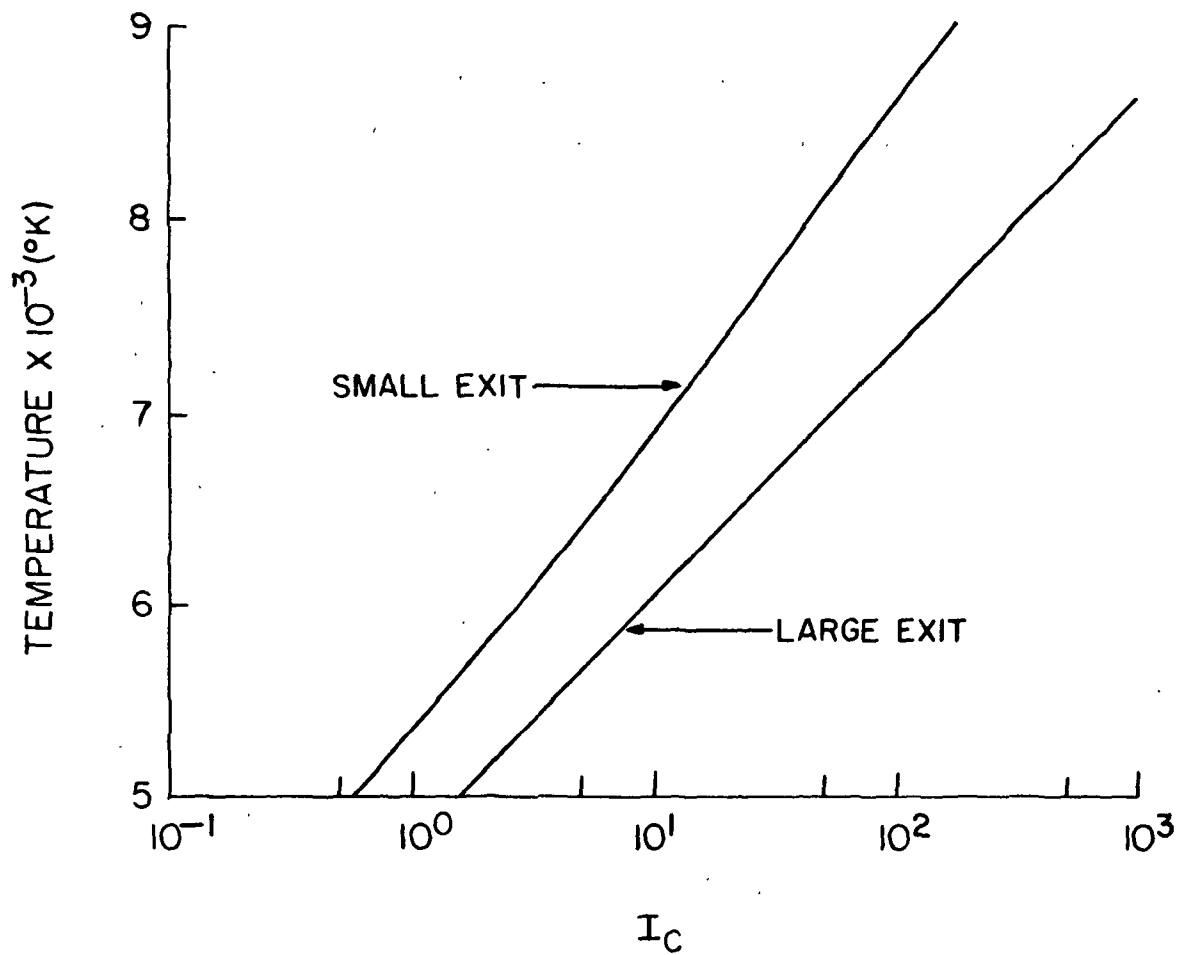


Figure 3.7

Matching criterion for composite boundary layer calculation. Small and large exit nozzles

zero. In the composite boundary layer, it is taken that  $g$  and  $f'$  may only be unity at a single level and consequently gradients may be present.

In addition to the intrinsic difficulty with the boundary layer equations, there is also a problem area with the integration of the relations when gradients are present at the upper boundary of the solution. Osborne (1969) assumed that the differential equations to be integrated were subject to the general boundary conditions given by

$$B_1 x(a) + B_2 x(b) = c , \quad (3-9)$$

where  $B_1$  and  $B_2$  are  $n \times n$  matrices,  $x(a)$  and  $x(b)$  are the values of  $x$  at the lower and upper boundary, respectively, and  $c$  is a vector of the values of the boundary conditions.  $B_1$  and  $B_2$  must remain uncoupled and consequently the maximum number of boundary conditions that can be stated is 5 in the case of an equilibrium boundary layer ( $f_w = f'_w = 0$ ,  $g_w = \text{constant}$ ,  $f'_e = 1$ , and  $g_e = 1$ ) and 7 in the case of the frozen boundary layer ( $f_w = f'_w = 0$ ,  $\Theta_w = \text{constant}$ ,  $S_{iw} = 0$  or a constant,  $f'_e = 1$ ,  $\Theta_e = 1$ , and  $S_{ie} = 1$ ). To include the additional boundary conditions of  $f''_e$  and  $g''_e$  would require the defining of two dummy variables to make  $B_1$  and  $B_2$  in the equilibrium solution  $7 \times 7$  matrices. Numerical experimentation showed this procedure to yield unsatisfactory results. Therefore, if a direct integration from the surface to the matching layer is done, the effects of heat flux and shear stress at the matching level must be neglected with the present method.

Figure 3.8 shows a partial profile of the heat flux for both a complete equilibrium and frozen boundary layer solution based on the same free stream conditions. As can be seen, in the frozen solution, the heat flux in the region of the changeover is about a factor of 4 less than at the wall, while in the equilibrium case it is a factor of 2 less

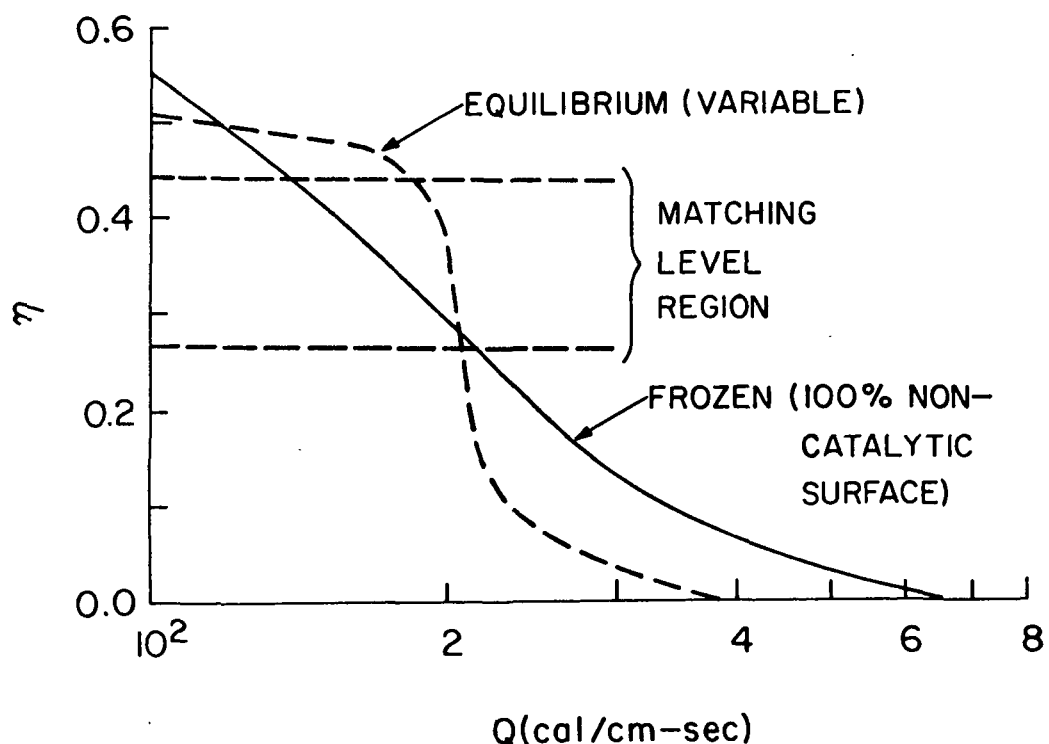


Figure 3.8

Heat flux for small exit nozzle, plate  
inclination of  $9.5^\circ$ ,  $x_p = 2.0$  cm

$\eta$	$T(^{\circ}\text{K})$	$I_c$	$y(\text{cm})$	MODEL
0.330	7269	17.8	0.018	small exit
0.440	8823	132	0.029	9.5 $^{\circ}$ plate inclination
0.275	5850	7.3	0.022	large exit
0.385	7415	115	0.039	19.5 $^{\circ}$ plate inclination

TABLE 3.3

Matching Levels in Composite Boundary Layers

than at the wall. This suggests that the heat flux from the frozen portion of the composite boundary layer may not play a dominant role in determining the surface heat transfer rate.

Figure 3.9 shows a partial profile for the shear stress of both a complete equilibrium and frozen calculation for the same free stream conditions. This graph would indicate that the shear stress in the region of the changeover is large. If the gradient of velocity  $f''$  feeds through the integration and affected the value of the enthalpy gradient at the wall, the surface heat transfer rate would be altered considerably.

From the above results, it would seem that as a first approximation, the solutions could be mated in the composite boundary layer by matching the values of velocity, the shear stress, and the specific enthalpy, as well as possible, and by ignoring matching of the heat flux.

As an alternative to the direct integration of the problem, lower portions of the previous equilibrium calculations were matched to the upper portions of frozen calculations, where both the solutions were based on the same free stream conditions. The concept of similarity has been exploited. It has been assumed that when the velocity, shear stress, and specific enthalpy are matched, the character of the gas in the lower portion of the boundary layer may better be described by the conditions of an equilibrium solution at some other position on the plate, but which are still similar mathematically.

In terms of the transformed variables, the shear stress is proportional by  $\mu f''$ .

Now,

$$\frac{\partial}{\partial y} = \frac{d\eta}{dy} \frac{\partial}{\partial \eta} \quad , \quad (3-10)$$

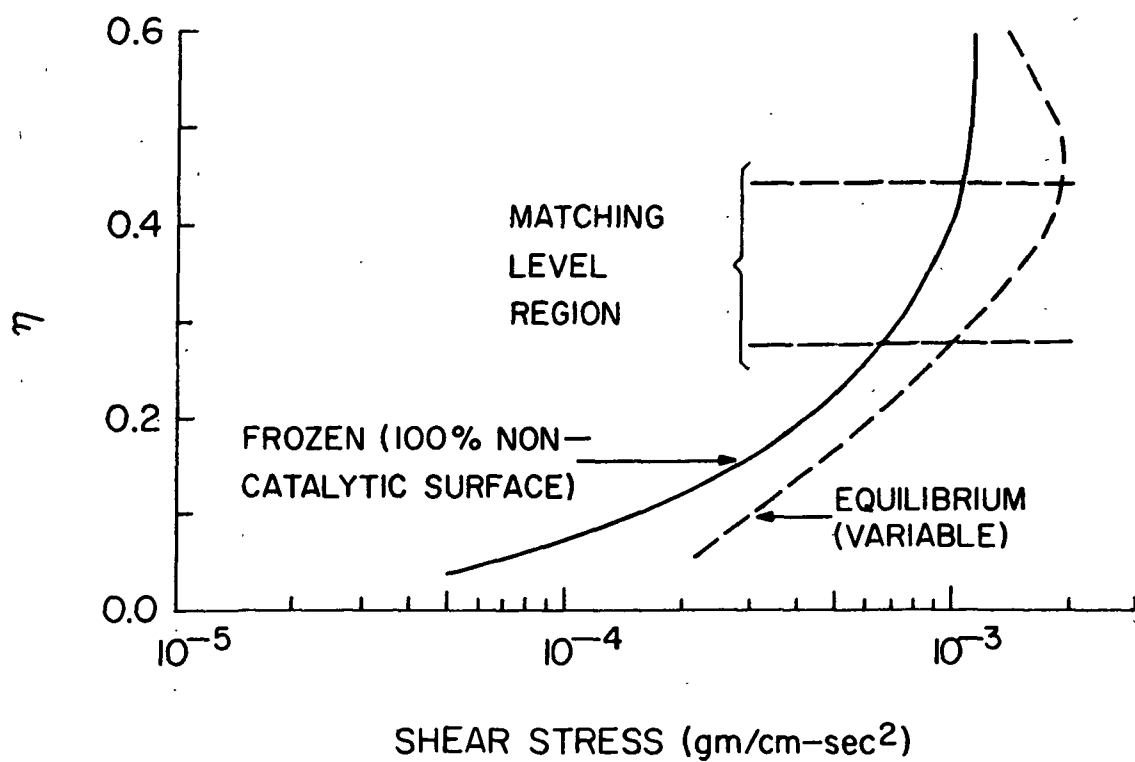


Figure 3.9

Shear stress for small exit nozzle,  $9.5^\circ$   
plate inclination,  $x_p = 2.0$  cm

so that from equations (2-5) and (2-7a) the shear stress  $x, y$  plane will be given by

$$\mu \frac{\partial u}{\partial y} = u_e^{3/2} (\rho_w k_w Pr_w / c_{pw})^{-1/2} \rho x^{-1/2} \mu f'' , \quad (3-11)$$

At the matching level, the ratio between the frozen and equilibrium shear stress will be given by

$$\frac{(\text{shear stress})_{Fr}}{(\text{shear stress})_{Eq}} = \frac{(\mu f'')_{Fr}}{(\mu f'')_{Eq}} \frac{x_{Eq}^{1/2}}{x_{Fr}^{1/2}} \frac{\rho_{Fr}}{\rho_{Eq}} . \quad (3-12)$$

Using equation (3-8), the choice of the matching level in the frozen boundary layer solution can be made. The stream tube in the equilibrium calculation having the same velocity as that of the matching level is located, and the corresponding shear stresses in terms of the transformed variables and densities are put into equation (3-12). The ratio of the  $x^{1/2}$  distances is adjusted so that the ratio of the shear stress in the  $x, y$  co-ordinates will be unity. Table 3.4 shows the results of these calculations for distances at 2 cm. up the plate for the large and small exit problems.

Any resultant increase in  $x_{Eq}^{1/2}$ , assuming  $x_{Fr}^{1/2}$  to remain fixed, will decrease the surface heat transfer rate by the same amount, since through similarity these quantities are coupled (i.e.  $Q \sqrt{x}$ ).

Figures 3.10 and 3.11 show the predicted surface heat transfer rates based on these choices of  $I_c$  for the small exit and large exit problems. If the choice of  $I_c$  is made at approximately 10, it can be seen that in no instance is the difference between the predicted and measured heat transfer rates greater than a factor of two. Indeed the accuracy is much better than this generally, with the normalized

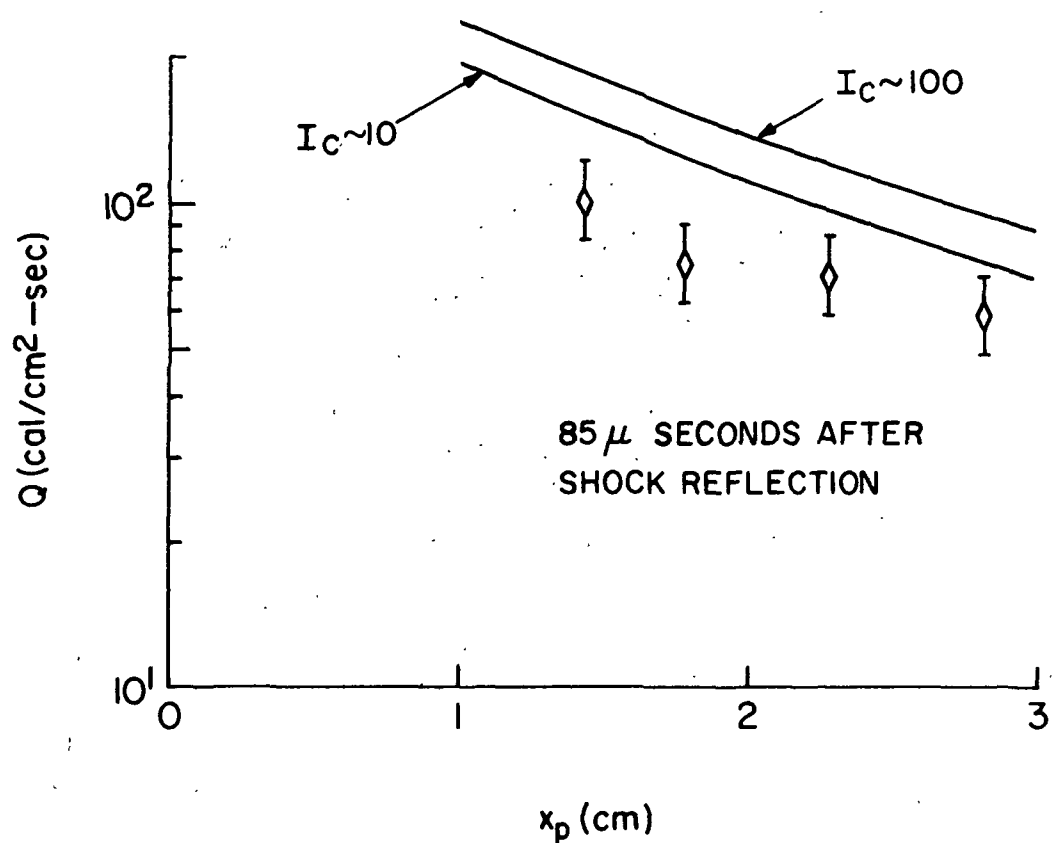


Figure 3.10

Composite boundary layer calculation of surface heat transfer rates. Small exit nozzle,  $9.5^\circ$  plate inclination

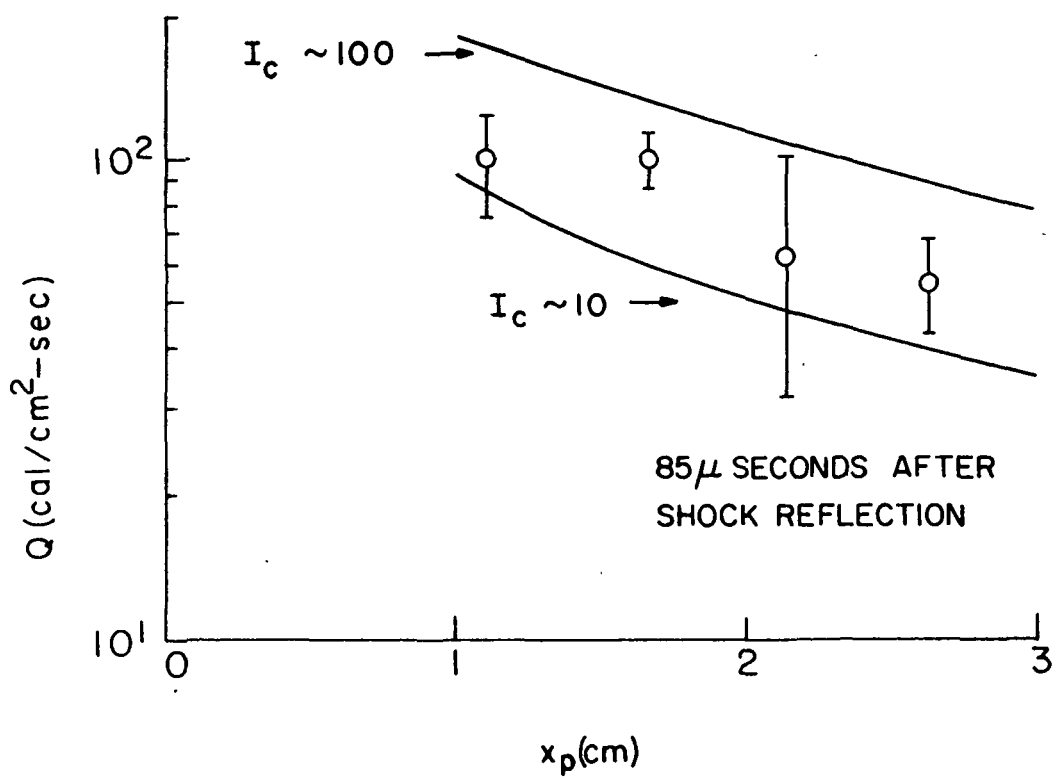


Figure 3.11

Composite boundary layer calculations of surface heat transfer rates, large exit nozzle, 19.5 plate inclination

standard deviation of all measurements from the theory being less than 40%.

The lower values of  $I_c$ , the greater is the tendency of the gas to depart from the frozen condition. It is clear that the best correlation between theory and data is obtained when a matching layer is chosen where there is a strong tendency to depart from the frozen state.

The large exit data, with a  $19.5^\circ$  plate inclination gave the best correlation with theory when  $I_c$  was set equal to 10. It is interesting to note that this case also provided the best overall match of shear stress, velocity, and specific enthalpy at the matching level. This would suggest that further efforts should be made in developing a method of integration of the boundary layer equations that will allow the inclusion of the velocity and enthalpy gradient as boundary conditions. The composite boundary layer would seem to offer a reasonable alternative to the much more difficult non-equilibrium calculations in very high enthalpy flows, and may be particularly useful for engineering calculations.

The work of Knöös (1968) predicted that much of the lower portion of an ionizing boundary layer may not be in either chemical or thermal equilibrium. It is to be emphasized that the concept of a composite boundary layer does not need to contradict the work of Knöös. The basic assumption in the composite calculation is that at a certain point in the boundary layer the gas conditions are better approximated by the extreme case of thermochemical equilibrium, rather than the extreme case of a chemically frozen boundary layer. It is considered that this condition will be true when there is significant recombination, regardless of whether the gas is in a state of equilibrium or not.

Case	Calculation	$\eta$	$I_c$	$f'$	$\mu f''$	$h$ (cal/gm)	$\rho$ (gm/cc)	$(X_{Eq}/X_{Fr})^{-1/2}$
small exit	frozen	0.330	17.8	0.284	0.798 E-3	1198	0.924 E-5	--
9.5° plate inclination		0.440	132	0.376	0.106 E-2	1397	0.761 E-5	--
equilibrium		0.422	--	0.284	0.193 E-2	926	0.951 E-5	0.402
		0.468	--	0.376	0.194 E-2	1098	0.838 E-5	0.496
large exit	frozen	0.275	7.3	0.262	0.432 E-3	1162	0.368 E-5	--
9.5° plate inclination		0.385	115	0.365	0.639 E-3	1365	0.290 E-5	--
equilibrium		0.553	--	0.365	0.112 E-2	1623	0.231 E-5	0.716

TABLE 3.4

Matching Level Data

#### 4. Summary of Part 3

In this part, the experimental data and its correlation with theory have been examined. There was good agreement between the measurement of test section Pitot pressure and an isentropic, real gas nozzle expansion theory until a time of flow of approximately 100 microseconds after shock reflection. After this period, the measured Pitot pressure dropped by approximately a factor of two. It has been suggested that this drop may be attributed to the injection of Helium driver gas into the periphery of the Argon flow in the area of the throat. The Argon expands down the nozzle as a real, ionizing gas, while the Helium expands as an ideal gas. This difference in flow character causes an increase in the effective area ratio in relation to the Argon with the observed fall in Pitot pressure.

The surface heat transfer rates showed a change of slope and general character at approximately 100 micro-seconds after shock reflection, correlating with the Pitot pressure data. The surface heat transfer rate is not adequately predicted with either an equilibrium or a frozen boundary layer assumption. However, improved prediction can be obtained by treating the boundary layer in two regions (a composite B/L), allowing the gas to pass from a chemically frozen region to one that is approximated by local thermochemical equilibrium. The position of the matching layer between the two regions is chosen by use of a simple criterion based on the recombination rate, and the parameters of velocity and shear stress are matched across it.

## REFERENCES

1. Back, L. H. (1967), "Laminar Boundary Layer Heat Transfer from a Partially Ionized Monatomic Gas," *Physics of Fluids*, 10, 4, 807-819.
2. Blottner, F. G. (1964), "Chemical Non-Equilibrium Boundary Layer," *AIAA*, 2, 232-240.
3. Bull, D. and Edwards, D. (1968), "An Investigation of the Reflected Shock Interaction Process in a Shock Tube," *AIAA*, 6, 1549-1555.
4. Davies, L. (1965), "The Interaction of the Reflected Shock with the Boundary Layer in a Shock Tube and Its Influence on the Duration of Hot Flow in the Reflected Shock Tunnel," *ARC 27 110-Hyp 505*, Aeronautical Research Council.
5. Davies, L. and Wilson, J. L. (1969), "Influence of Reflected Shock and Boundary-Layer Interaction on Shock Tube Flow," *Physics of Fluids*, 12, Supplement 1, 1-37.
6. Dorrance, W. H. (1962), Viscous Hypersonic Flow, McGraw Hill.
7. Dunn, M. G. (1969a), "Experimental Study of High Enthalpy Shock-Tunnel Flow. Part I: Shock Tunnel and Nozzle Starting Time," *AIAA*, 7, 8, 1553-1560.
8. Dunn, M. G. (1969b), "Experimental Study of High Enthalpy Shock-Tunnel Flow. Part II: Nozzle Flow Characteristics," *AIAA*, 7, 9, 1717-1724.
9. Fay, J. A. and Riddell, F. R. (1958), "Theory of Stagnation Point Heat Transfer in Dissociated Air," *Jour. of Aeronautical Sci.*, 25, 2, 73-85.
10. Fay, J. A. and Kemp, N. H. (1963), "Theory of Stagnation Point Heat Transfer in a Partially Ionized Diatomic Gas," *AIAA*, 1, 12, 2741] 2751.
11. Finson, M. L. and Kemp, N. H. (1963), "Theory of Stagnation Point Heat Transfer in Ionized Monatomic Gas," *Physics of Fluids*, 8, 201-204.
12. Hall, J. G. (1963), "Effects of Ambient Nonuniformities in Flow Over Hypersonic Test Bodies," *CAL Report No. 128*, Cornell Aeronautical Laboratory, Inc., Buffalo, N. Y.
13. Hayes, W. D. and Probstein, R. F. (1969), Hypersonic Flow Theory, Academic Press.
14. Kaegi, E. M. and Muntz, E. P. (1964), "Driver-Driven Gas Mixing and Its Effect on Shock Tunnel Test Time," Paper, *Third Hypervelocity Techniques Symposium*, March 17-18, Denver, Colorado.

15. Knöös, S. (1968), "Boundary-Layer Structure in a Shock-Generated Plasma Flow, Part 1," *Jour. of Plasma Physics*, 2, 2, 207-242.
16. Lees, L. (1956), "Laminar Heat Transfer Over Blunt-Nosed Bodies at Hypersonic Flight Speeds," *Jet Propulsion*, 26, 4, 259-269.
17. Lighthill, M. J. (1957), "Dynamics of a Dissociating Gas, Part 1," *Journal Fluid Mech.*, 2, 1-32.
18. Logan, P. F. (1971), Ph. D. Thesis (To Be Published), Australian National University.
19. Mark, H. (1957), "The Interaction of a Reflected Shock Wave with the Boundary Layer in a Shock Tube," Ph. D. Thesis, Cornell University.
20. McCroskey, W. J., Bogdonoff, S. M., and McDougall, J. G. (1966), "An Experimental Model for the Sharp Flat Plate in Rarefied Hypersonic Flow," *AIAA*, 4, 9, 1580-1587.
21. Oettinger, P. E. and Bershader, D. (1967), "A Unified Treatment of the Relaxation Phenomenon in Radiating Argon Plasma Flows," *AIAA*, 5, 9, 1625-1632.
22. Osborne, M. R. (1969), "On Shooting Methods for Boundary Value Problems," *Jour. Math Analysis and Applications*, 27, 2, 417-433.
23. Pallone, A. J., Moore, J. A., and Erdos, J. I., (1964), "Non-Equilibrium, Non-Similar Solutions of the Laminar Boundary-Layer Equations," *AIAA*, 2, 10, 1706-1713.
24. Pan, Y. S. and Probstein, R. F. (1966), "Rarefied-Flow Transition at Leading Edge," Fundamental Phenomena in Hypersonic Flow, Cornell University Press.
25. Petschek, H. and Byron, S. (1957), "Approach to Equilibrium Ionization Behind Strong Shock Waves in Argon," *Annal of Physics*, 1, 270-315.
26. Reilly, J. P. (1964), "Stagnation-Point Heating in Ionized Monatomic Gases," *Physics of Fluids*, 7, 12, 1905-1912.
27. Rudman, S. and Rubin, S. G. (1968), "Hypersonic Viscous Flow Over Slender Bodies," *AIAA*, 6, 10, 1883-1889.
28. Rutowski, R. W. and Bershader, D. (1964), "Shock Tube Studies of Radiative Transport in an Argon Plasma," *Physics of Fluids*, 7, 4, 568-577.
29. Slade, J. C. (1970), "Mass Spectroscopy in Shock Tunnels," M. S. Thesis, Australian National University.

30. Stalker, R. J. (1967), "A Study of the Free-Piston Shock Tunnel," AIAA, 5, 12, 2160-2165.
31. Vidal, R. J., Golian, T. C., and Bartz, J. A. (1963), "An Experimental Study of Hypersonic Low-Density Viscous Effects on a Sharp Flat Plate," Paper No. 63-435, AIAA Conference on Physics of Entry Into Planetary Atmospheres, August 26-28, M.I.T.
32. Yanow, G. (1971), "High Enthalpy Hypersonic Boundary Layer Flow," Ph. D. Thesis, The Australian National University.

SYMBOLS AND NOMENCLATURE

A  $(Le - 1) h_i (d\alpha/dh)_p$ , see equation (1-9); Area

a Speed of Sound

$C_1 Y Pr/c_p$ , see equation (1-14)

$C_2 (1 + A)/c_p$ , see equation (1-14)

$C_3 (1 - Pr)/c_p$ , see equation (1-14)

$C_4 Y/c_p$ , see equation (1-14)

$C_i \rho_i/\rho$ , species mass fraction

$c_p \sum_i C_i c_{pi}$ , specific heat at constant pressure (frozen)

$c_{pi}$  Frozen specific heat of species i

$D_i$  Coefficient of diffusion of species i through mixture of species

E Symbol for power of ten in computer type print out, e.g.  $10^x = Ex$

F See equation (2-30)

$f' u/u_e$ , see equation (1-9):  $f = \int_0^\infty df/d\eta$

$g (u^2/2 + h)/H_s$ , see equation (1-9)

$H u^2/2 + h$ , total enthalpy

$h$  Specific enthalpy

$h_i \int c_{pi} dT + h_i^0$ , specific enthalpy of species i

$h_i^0$	Heat of formation of species i
I	Ionization energy of Argon, 9026 cal/gm
$I_c$	Special constant in composite boundary layer calculation, see equation (3-8)
k	Thermal conductivity: Boltzmann's constant
$K_1$	$(Pr_w / c_{pw}) / C_1$ , see equation (1-15)
$K_2$	$(Pr_w / c_{pw}) / (Y C_2)$ , see equation (1-15)
$K_3$	$(Pr_w / c_{pw}) / (H_S C_2)$ , see equation (1-15)
$K_4$	$(Pr_w / c_{pw}) / C_4$ , see equation (1-15a)
$K_E$	Equilibrium constant for Argon, see equation (3-4)
$K_I$	Argon reaction rate coefficient, see equation (3-5)
$K_L$	$(c_{pw} / c_p) Le \alpha_e$ , see equation (1-15a)
$K_R$	Argon recombination rate coefficient, see equation (3-5)
$K_T$	$(Pr u_e^2) / (T_e c_p)$ , see equation (1-15a)
$L_e$	$D_i \rho c_p / k$ , Lewis number
M	Mach number; molecular mass
m	Mass
$m_e$	Mass of electron

n	Number of moles
$N_e$	Number of electrons per cc
P	Pressure
Pr	$\mu c_p / k$ , Prandtl number
Q, -q	Heat flux
R	$R_o / M$ ; on axis length of nozzle measured from throat
$R_e$	$\rho u x / \mu$ , Reynold's number
$R_o$	Universal gas constant
$R_x$	Radius of curvature of the nozzle at x distance from the throat
S	Entropy
$S_i$	$\alpha / \alpha_e$ , see equation (1-13)
T	Temperature
t	Time
$t_c$	Characteristic time used in calculation of $I_c$
u	Velocity along x axis in shock co-ordinate system
V	Volume
$\bar{V}$	$M(c/R_e)^{\frac{1}{2}}$ , rarefaction parameter
v	Velocity along y axis in shock co-ordinate system
$\dot{w}_i$	Mass rate of change of species i per unit volume

### GREEK SYMBOLS

$\alpha$	Ionization fraction
$\beta$	Angle between plate surface and nozzle axis
$\beta_e$	Temperature of excitation of Argon (see equation 3-3)
$\gamma$	$c_p/c_v$ , ratio of specific heats
$\gamma_{\text{eff}}$	Effective value of $\gamma$ , see equation (2-10)
$\delta$	Divergence angle of nozzle flow
$\delta^*$	Displacement thickness
$\epsilon$	Energy of Argon ionization, $2.524 \times 10^{-11}$ ergs/mole
$\eta$	Transformed y-axis parameter, see equation (1-6)
$\Theta$	Angle of plate inclination of on axis flow
$\Theta_I$	Temperature of Argon Ionization, see equation (3-3)
$\mu$	Viscosity
$\xi$	See equation (1-7)
$\rho$	Density
$\bar{X}$	$M^3 (C/Re)^{\frac{1}{2}}$ , leading edge interaction parameter

### SUBSCRIPTS

A	Refers to Argon
AI	Refers to Argon ions
AN	Refers to neutral Argon atoms
e	Boundary layer free stream conditions
H	Refers to Helium
N	Conditions at nozzle exit
n	Conditions taken normal to shock front
o	Arbitrary reference condition
P	Constant pressure condition
1	Conditions before passage of shock front
2	Conditions after passage of shock front
3	Reflected shock conditions

### SPECIAL TERMS

equilibrium	A gas in which the temperature and ionization follow the Saha equation; also thermochemical equilibrium.
frozen	A gas in which no chemical reactions occur during the time of interest.
large exit	Refers to flow with nozzle having an exit area ratio of 1204 and with a $19.5^\circ$ plate inclination.

small exit      Refers to flow with nozzle having an exit area ratio of 147 and with a 9.5° plate inclination.

transport parameters      The special terms defined in equations (1-14) and (1-14a)

transport properties      Thermal conductivity, viscosity, and diffusion (ambipolar)

very high enthalpy      Flows with stagnation enthalpies in excess of 12 eV or approximately 7000 cal/gm.

#### ACKNOWLEDGEMENTS

The author would like to take this opportunity to sincerely thank Dr. R. J. Stalker of the A. N. U. Aerophysics Laboratory for his technical advice, criticisms, and general guidance in all aspects of the work; Mr. R. French for his excellent contributions and technical knowledge relating to the shock tube facilities; and to the Ionosphere Research Laboratory for giving me the time to prepare the work for publication and for the excellent final drawings and manuscript typing.